POLITECNICO
MILANO 1863

SCUOLA DI INGEGNERIA INDUSTRIALE
E DELL'INFORMAZIONE

EXECUTIVE SUMMARY OF THE THESIS

Accounting for friction in the characterization of synthetic sports surfaces

TESI MAGISTRALE IN MATERIALS ENGINEERING AND NANOTECHNOLOGY

AUTHOR: SAMUELE ZALAFFI

ADVISOR: LUCA ANDENA

ACADEMIC YEAR: 2020-2021

1. Introduction

1.1 Athletic tracks

Nowadays synthetic athletic tracks are the most widely used thanks to their low maintenance needs and durability. They usually consists in two layers: a base layer, which can have different geometrical patterns and a finishing layer. The Word Athletics (WA) recognizes that the shock absorption ability of a track is important to ensure safety and comfort to the athlete and the main parameter used to measure this ability is the Force Reduction (*FR*) [1]. This ability is influenced by the geometrical design of the track and by the coefficients characterizing the materials composing the track. For this reason a reliable determination of the true materials coefficients, independent on geometry and other parameters (e.g. friction), is a key step for the characterization and optimization of the sports surfaces.

1.2 Finite element models

Previous works [2,3] studied the influence of geometry and materials coefficients on shock absorption ability of tracks through different finite element models. The first model of shock absorption tests realized was a 2D axisymmetric one [2] which, however, neglected the real track structure, considering it as a single layer of material having homogenized properties. To consider the real geometrical pattern of the track an analogous 3D model was created in the following work [3]. The results drawn from these models confirmed the importance of an accurate design of the track geometry and materials for its optimization.

1.3 Visco-hyperelastic model

In the following work [4] four different track materials named: B, EI, CF and LG were characterized with a visco-hyperelastic model that was then implemented in the above-mentioned 3D model. The constitutive model used expresses the stress as the product of two distinct functions: a strain-dependent function, $\sigma_0(\varepsilon)$ having the

dimension of stress, that is described with an hyperelastic model and a dimensionless time-dependent function, *g(t)*, so that (equation 1):

$$\sigma(\varepsilon;\ t)\ =\ \sigma_0\ (\varepsilon)\ g(t)\ \text{Eq. 1}$$

Where *g(t)* is described by a Prony series like the one in equation 2.

$$g(t) = g_{inf} + \sum g_i e^{-\frac{t}{\tau_i}}\ \text{Eq. 2}$$

Where $g_i = \frac{G_i}{G_0}$ are the dimensionless moduli, parameters of the Prony series that have to be determined. The stress at a desired time can be calculated from the input strain history using an algorithm based on finite time increments. The resulting recursive formula is shown in equation 3.

$$\sigma(t_{n+1}) = \sigma_0(\mathrm{t_n})g_{inf}\ + \sum e^{-\frac{\Delta t}{\tau_i}} * h_i(t_n) +$$

$$g_i * \frac{1-e^{-\frac{\Delta t}{\tau_i}}}{\frac{\Delta t}{\tau_i}}[\sigma_0(t_{n+1}) - \sigma_0(t_n)]\ \text{Eq. 3}$$

Where $\int_0^t g_i e^{-\frac{t-s}{\tau_i}} \frac{d\sigma_0}{ds}\ (t-s)ds = h_i(t)$ and τ_i are the characteristic times of the series. The tests used to characterize the materials with this model were uniaxial compression and stress relaxation tests that were performed both without lubrication and with a PTFE film as lubricant. The resulting curves of the latter have been used for the fitting of the parameters with different hyperelastic models. Here the results for the Mooney-Rivilin visco-hyperelastic model are shown in table 1.

1.4 Friction problem

As suggested by Cotta Ramusino [4], the influence of friction during the experimental tests has not been eliminated and this affects the results of the fitting procedure. In particular, the presence of friction during the compression tests prevent the expansion of the specimen conferring a higher apparent stiffness to the material. This fact was observed comparing stress-stretch curves obtained with and without PTFE [4]. In the latter case higher compression stresses were reported for the same level of stretch thus indicating that there is a marked influence of friction

1.5 Aim of the work

The aim of this work was to improve the description of friction for the above-mentioned materials and repeat the fitting procedure to obtain more accurate materials coefficient to be used in the above-mentioned FEM models for the characterization of sports surfaces.

Mooney-Rivlin	C_{10}(MPa)	C_{01}(MPa)	g_1	g_2	g_3	g_4
B	0.96	0	0.10	0.17	0.18	0.040
EI	1.6	0	0.20	0.19	0.10	0.057
CF	0.60	0	0.10	0.33	0.050	0.06
LG	0.87	0	0.15	0.25	0.07	0.047

Table 1 Mooney-Rivilin and Prony coefficients obtained in [4]

2. Materials and methods

2.1 Materials

Four rubber mixes used for athletic tracks application and provided by the producer Mondo Spa have been tested in this work. The materials are the same described in [4] and their physical characteristics are summarized in table 2.

Material	Function	Density(g/cm³)	Thickness (mm)	Color
B	Finishing	(1.302 ± 0.010)	4.67 ± 0.07	BLUE
LG	Base	(1.402 ± 0.020)	4.67 ± 0.04	GREY
EI	Finishing	(1.373 ± 0.0030)	4.67 ± 0.03	LIGHT BLUE
CF	Base	(1.247 ± 0.010)	4.72 ± 0.06	BLACK

Table 2 Materials: physical properties

2.2 Experimental tests

2.2.1 Compression tests

Compression tests with well lubricated surfaces needed to be performed to characterize our materials. In order to do this PTFE and soap were used as lubricants. Two configurations shown in figure 2 were compared to see which resulted in the lowest friction. The experimental set up is sketched in figure 1. Tests were carried out at different strain rates down to a stretch of 0.6. All test parameters are summarized in table 3. Samples used were circular with thickness of about 4.7 mm and nominal radius of 9 mm.

Test	Velocity (s^{-1})	Final deformation (%)	Total Time (s)
Compression	0.006	40	66.67
Compression	0.06	40	6.667
Compression	0.6	40	0.6667

Table 3 Parameters for compression tests

2.2.2 Stress relaxation tests

For the stress relaxation tests the same set-up and lubrication described above were used. We did two kinds of test with different final stretch but with the same ramp slope. Parameters are summarized in table 4.

Test	Velocity (s^{-1})	Final deformation (%)	Total Time (s)
Stress relaxation	0.06 (ramp)	10	301.7
Stress relaxation	0.06 (ramp)	30	305.0

Table 4 Parameters for compression tests

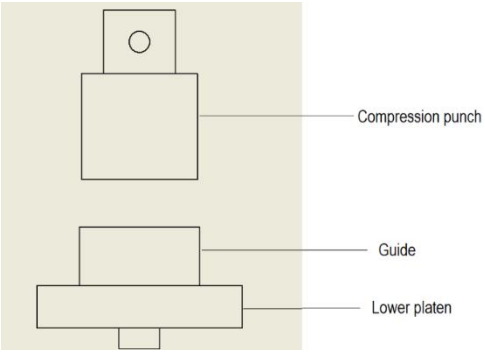

Figure 1 Experimental setup for compression tests and stress relaxation tests.

Figure 2 Lubrication types of interface used during tests. Soap-PTFE-soap method on the left and PTFE-soap-PTFE method on the right. The configuration was repeated identical for the lower surface

2.2.3 Friction sled

Measurement of friction coefficient (COF) were performed using different substrates aiming at representing the interfaces between sample and compression platens both in the tests held by [4] (PTFE and steel) and in the tests done in this work (figure 2) were tested. For the PTFE substrate the film was fixed to measure the friction between rubber and PTFE, this happened also for the soap-PTFE-soap configuration. In the PTFE-soap-PTFE configuration, instead the sliding between the two sheets was allowed. The setup is presented in figure 3. The velocities of the tests were chosen knowing the compression velocities acting during test and assuming volume conservation of the sample to estimate the radial expansion velocity. Parameters of the tests are in table 5, a lower run was chosen for the lowest velocity due to the higher time needed .The normal force was about 12 N for all samples.

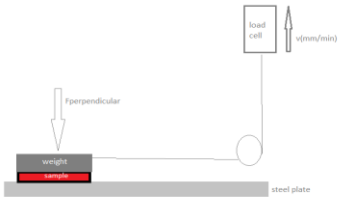

Figure 3 Experimental apparatus for COF measurement

Velocity(mm/min)	Run(mm)	Perpendicular Force (N)
162	100	12
16.2	100	12
1.62	40	12

Table 5 Parameters of friction sled experimental tests

2.3 Numerical simulations

Numerical simulations of the compression and stress relaxation tests were carried out. In particular, different models were created on the commercial software for FEA analysis Abaqus 2018. These simulations were than run changing the friction coefficient between the disks and the sample in order to investigate how the amount of friction influences the results of the test.

2.3.1 Models for compression and stress relaxation tests

The first model created was a 2D axial symmetric one. The sample was modeled as deformable shell and meshed with hybrid elements CAX4RH. Dimension of the sample were h=4.7 mm and r=9 mm. The bulk of the sample was considered as a homogeneous with material properties including time domain Prony viscoelasticity, general density and hyperelasticity defined with instantaneous coefficients. Compression disks were instead modeled as analytical rigid wire surfaces . Surfaces had a normal hard contact component and a penalty friction tangential behavior. Boundary

conditions are shown in figure 4. In the case of compression tests, the displacement was applied in a single dynamic implicit quasi-static step. For stress-relaxation tests instead two steps were needed; the first is equivalent to the one for compression tests except for the final value of deformation and time of the step. The second is still a dynamic implicit step of 300 s in which the displacement is maintained fixed at its last value while time elapses. An equivalent 3D model was also created by designing just a quarter of the sample and putting Y and X symmetry boundary conditions on the cut faces of the sample. In this case, C3D8RH hybrid elements were used.

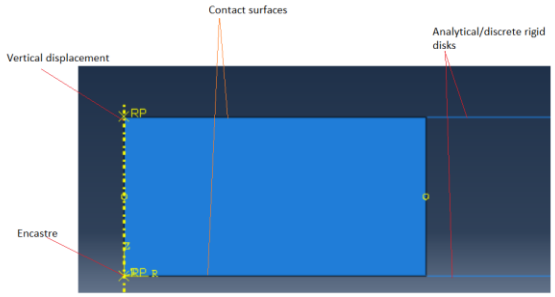

Figure 4 Boundary conditions of 2D model

In order to account for the very large displacement and deformation of the sample during a 40% strain input, different meshes have been tried to help convergence and to get the best and most accurate solution. Meshes are shown in figure 5 for the 2D model. For the 3D model, meshes tested were a sweep mesh and a structured one.

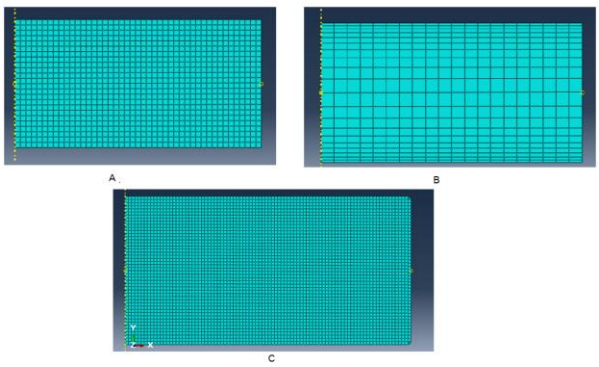

Figure 5 Meshes for 2D model. For mesh C a 0.1mm curvature radius was added to sample geometry

2.3.2 Sled simulations

2D and 3D model for sled tests were realized. Properties of materials and interactions are the same described above. Boundary conditions are shown in figure 6. Two steps were used, a static step for the application of the weight, which was represented by a body force acting on a rigid body tied to the sample, and a dynamic step to enforce the sliding of the sample over the substrate with an horizontal displacement of the weight reference point. The meshes adopted were a simple all quad CPS4R for the 2D and a structured C3D8RH for the 3D.

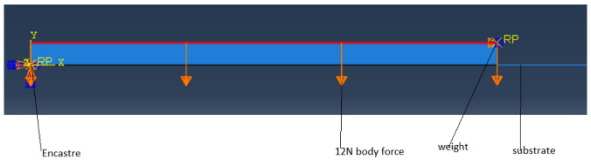

Figure 6 BCs for 2D sled model.

3. Results and discussion

3.1 Experimental tests

3.1.1 Compression and stress relaxation tests

The results of compression and stress relaxation tests are shown in comparison with the results obtained by [4] in figure 7 .The addition of soap surely decreases the amount of friction and the two configurations tested for soap gave equivalent results.

3.1.2 Friction sled results

Results of friction coefficients are represented in COF versus logarithm of velocity plot for steel, PTFE and soap-PTFE-soap configurations (figure 8). For the PTFE-soap-PTFE configuration the results are, as expected, material-independent because the sliding is occurring always between the two PTFE films. The measured COF is around 0.1 for all velocities.

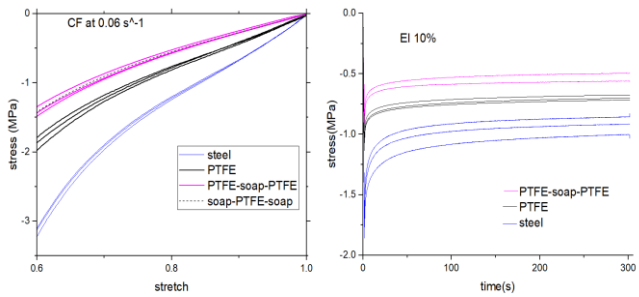

Figure 7 Representative examples of results for compression and stress relaxation tests

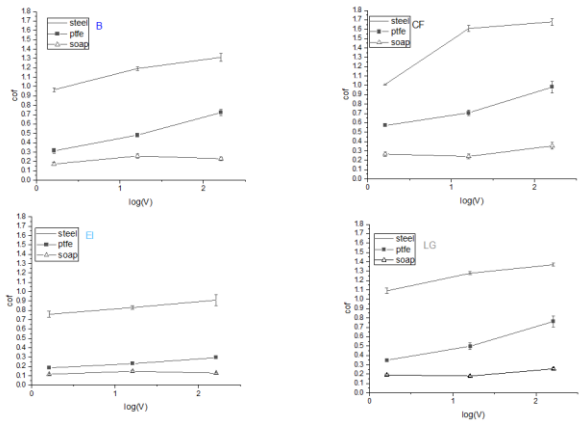

Figure 8 Results of COF for steel, PTFE and soap-PTFE-soap configurations.

3.2 Simulations results

3.2.1 Compression tests simulations

The meshes tested for the 2D model gave identical results at low level of friction. However mesh B and C seemed to give smoother results and less convergence problem for higher COF (>0.3).Also the mesh size needed to be decreased for higher levels of friction. The 3D model for both the meshes tested gave almost the same results found for the 2D model and for this reason, given the higher computational cost of the 3D model, only the 2D model is considered from now on. Compression stress-stretch curves obtained for different COFs were put in comparison with the same curve found in frictionless condition. In particular, the mean ratio of the latter with these curves (after interpolation at desired values of stretch) were studied. The results are shown in figure 9 and are compared with the results of an analytical model by Gent et al [5], which computes how the apparent stiffness changes for different level of friction during the compression of rubber blocks. The trend shown in figure 9 turned out to be the same for all materials and velocities used in simulations. However numerical results disagree with experimental ones. In order to show this finding curves were normalized to the PTFE curve, whose value of friction depended on material and velocity according to the friction sled results shown above. In figure 10 we see that experiments suggest there is still a strong dependency on friction at high values of COF (>0.6) where numerical results instead present an asymptote. We should underline that the model shows some critical issues, in fact an important edge effect is observed at the corners of the specimen where the contact pressure is suddenly increased at the very last node. This effect is encountered also in the numerical model realized by [5]. This might prevent the sample expansion by putting the corners in a bounded condition when they should actually slip. It is also important to notice that a very high distortion of the corner elements was always observed when the COF was high enough to provoke a lateral surface roll over (>0.3). This problem was less important when mesh C was adopted, however even in this case a strong stress gradient in the corners elements was recorded (figure 11).

3.2.2 Friction sled simulations

The aim of the friction sled model was to study the behavior of the contact type chosen and how it could affect the results. The same edge effect described above was found in this model; however, the results seemed to be coherent with the expected ones. In particular, the integral tangential force needed for the sliding of the sample was equal to the normal force multiplied by the COF and both the shear stresses and strains were well described and quite constant in the sample. Problems are encountered when the normal force is increased, in fact in this case the sample tend to rotate and penetrate within substrate (figure 12).

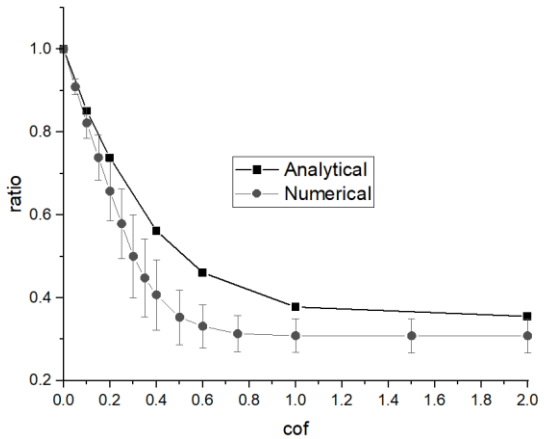

Figure 9 Mean ratio between frictionless curve and curves at different COFs. Analytical[5] and numerical results

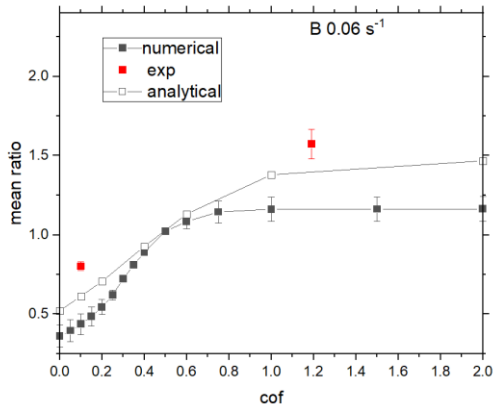

Figure 10 Experimental, analytical and numerical mean ratios with the PTFE curve for B at 0.06 s^{-1}.

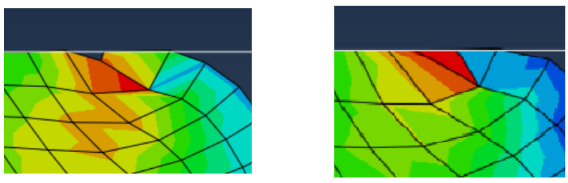

Figure 11 Deformation of corners for Mesh A(left) and C(right) during roll over at COF=0.6. Mises stress plot

Figure 12 S12 output plot for Fp=500N shell thickness=1

3.3 Fitting of new parameters

In the end, a new fitting was realized on the experimental curves obtained with soap (Table 6). Following the same procedure developed in [4] characteristic times of 0.3,3,30 and 300 s were used. Results were than validated with the 2D model and showed a good agreement. Results are compared with the ones obtained by [4] in graph 13.

To extrapolate the frictionless behavior of the materials it was assumed that the mean ratio between the frictionless virtual curve and the experimental curve was the same found with the numerical model, considering as the value of friction for the experimental curve the one measured with the sled for the corresponding PTFE-soap-PTFE configuration (about 0.1 for all velocities). From this value of friction, we extrapolated the mean ratio between the frictionless curve and the friction curve (0.1), as described in 3.2. This value is equal to 0.82 and it was then multiplied by the stress values of the soap experimental curves, obtaining in this way curves which should describe the frictionless behavior of the material. These curves were finally used for a new fitting. The final results are shown in table 7. To validate the results obtained, we run simulations of the experimental tests setting the friction at 0.1, value assigned to the experimental curves. The results were then compared with the experimental soap curves. Similarly we tried to run simulations at the friction level measured for PTFE and steel interfaces and then compare them with the corresponding experimental curves. In addition we plotted the same simulations results found with the previous coefficients obtained in [4]. Of course, the latter better describe the PTFE curve since it represents the data on which coefficients were fitted. However if we consider the steel curve, we see that having taken into account the effect of friction in the extrapolation of the material coefficients have significantly improved the prevision of this curve once the friction is added to the model. However the numerical model used with new coefficients still predicts much higher stresses with respect to the experimental ones (figure 14)

Material	C_{10} (MPa)	C_{01}(MPa)	g_1	g_2	g_3	g_4
B	0.81	0	0.19	0.059	0.14	0.060
EI	1.3	0	0.091	0.14	0.19	0.066
CF	0.44	0	0.24	0	0.24	0.050
LG	0.56	0	0.089	0.11	0.096	0.24

Table 6 Fitting of parameters on experimental curves obtained with soap lubricated PTFE interfaces

Material	C_{10} (MPa)	C_{01}(MPa)	g_1	g_2	g_3	g_4
B	0.66	0	0.19	0.059	0.14	0.060
EI	1.1	0	0.13	0.084	0.21	0.073
CF	0.36	0	0.24	0	0.22	0.050
LG	0.48	0	0.14	0.082	0.10	0.23

Table 7 Fitting of parameters on experimental curves obtained with soap lubricated PTFE interfaces rescaled by a factor of 0.82 computed from FEA simulations for COF 0.1.

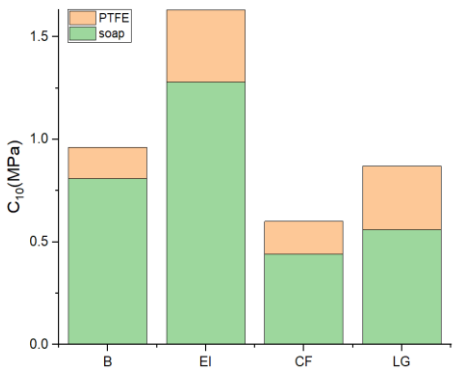

Figure 13 Comparison between coefficients obtained with PTFE and the one obtained with soap (table 6)

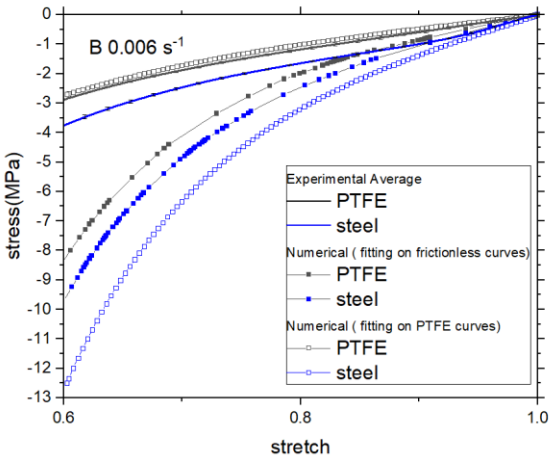

Figure 14 Numerical simulations of compression obtained with coefficients of table 7 for COF assigned to PTFE and steel according to sled results and compared with experimental curves

4. Conclusion

For what concerns the results of the first fitting we can say that the use of new lubrication techniques have for sure decreased the influence of friction and has allowed us to find more reliable materials coefficients that can be used for the characterization of the athletic tracks. Therefore, the tested lubrication system with soap and PTFE proved to be a step in the right direction of minimizing the influence of friction during the compression tests. However, these results are still influenced by friction, as a negligible friction configuration is impossible to achieve from the experimental point of view.

For this reason, the second approach described above was considered. These new results are still not fully satisfying; even if the new approach provides a marked improvement with respect to the previous one, some issues still need to be solved. In fact, it was observed that the numerical model used to eliminate the friction influence was not able to completely predict experimental results previously obtained in [4]. In particular, these results still showed a high dependence on friction at high level of COF where the numerical model showed the presence of a plateau. A possible cause is that the pressure under which friction coefficients were measured is much lower than the one acting during the real compression of the rubber samples, and this fact may affect the measured COF values. Due to the reasons listed above instead, the results obtained with the second fitting are not completely reliable and need further study. However the realization of a model able to extrapolate the frictionless behavior of the materials seems feasible but, it still needs a considerable amount of future work.

For example, a way to improve the model could also be the collection of experimental compression curves for specimens of different aspect ratio and the comparison with corresponding numerical simulations. In addition, further investigation on the dependence of friction on the applied contact pressure should be considered for the here presented materials, in order to better understand which is the value of friction that is acting during the compression test.

We can conclude saying that further studies about the realization of an accurate model able to extrapolate the frictionless behavior of the material could be really helpful to speed up the procedures for the characterization of rubbery materials at high level of compression strain, giving the possibility to obtain more reliable data to be used for the study about the optimization of the sports surfaces design..

5. Bibliography

[1] World Athletics, Track and Field Facilities Manual. World Athletics, 2019.

[2] L. Andena, F. Briatico-Vangosa, E. Cazzoni, A. Ciancio, S. Mariani, and A. Pavan,*"Modeling of shock absorption in athletics track surfaces,"* Sports engineering, vol. 18, no. 1, pp. 1–10, 2015.

[3] L. Andena, S. Aleo, F. Caimmi, F. Briatico-Vangosa, S. Mariani, S. Tagliabue, and A. Pavan, *"Modelling the cushioning properties of athletic tracks"*, Sports Engineering, vol. 21, no. 4, pp. 453–463, 2018.

[4] F. Cotta Ramusino *"A visco-hyperelastic model for elastomeric materials"*, Master Thesis in Materials engineering and nanotechnology at Politecnico di Milano, 2020

[5] A. N. Gent, F. M. Discenzo, J. B. Suh:*" Compression of Rubber Disks Between Frictional Surfaces"*

POLITECNICO
MILANO 1863

SCUOLA DI INGEGNERIA INDUSTRIALE
E DELL'INFORMAZIONE

Accounting for friction in the characterization of synthetic sports surfaces

TESI DI LAUREA MAGISTRALE IN
Materials engineering and nanotechnology

Author: **Samuele Zalaffi**

Student ID:	10567003
Advisor:	Luca Andena
Co-advisor:	Stefano Tagliabue
Academic Year:	2020-21

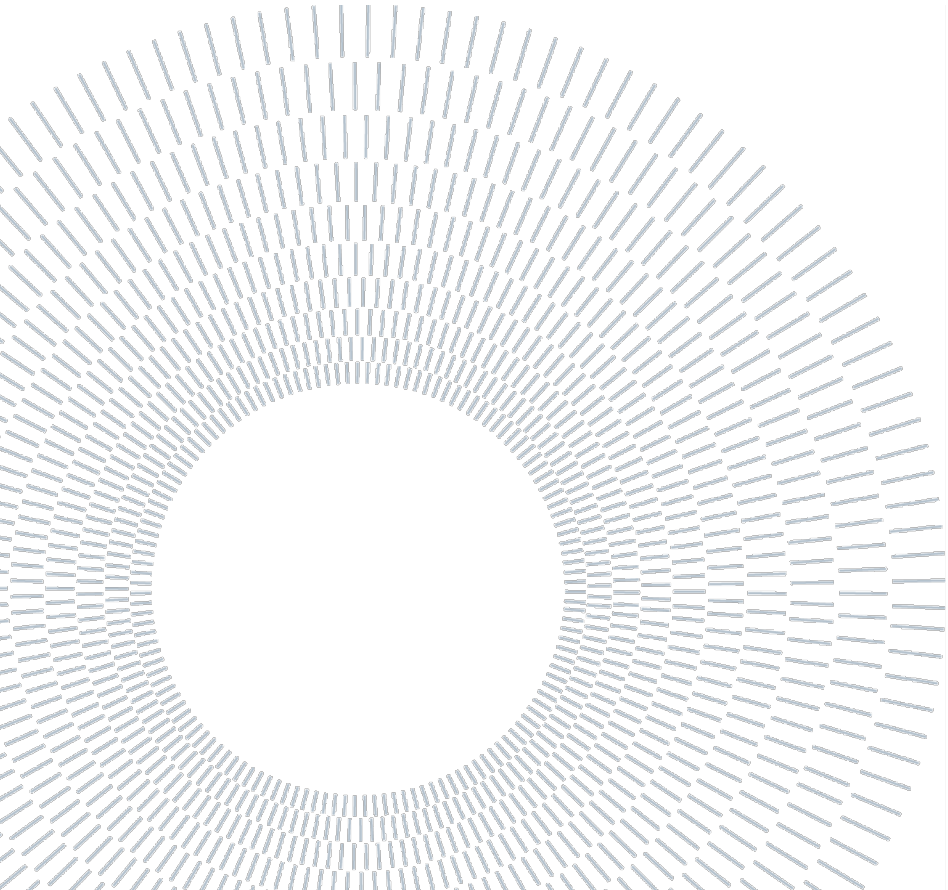

Abstract

This work is focused on the characterization of four rubbery materials, used for the production of athletic tracks with a visco-hyperelastic model accounting for the influence of friction acting during compression tests. The above mentioned model had been previously used to determine the shock absorption properties of these materials through the use of the finite element model of the Artificial Athlete already employed in previous works. However the material coefficients used for this purpose had been determined in condition that didn't completely eliminate the effect of friction. For this reason, in this work, experimental tests (compression and stress relaxation) in nearly frictionless condition were done along with measurement of the rubber friction coefficients for different substrates and lubrication techniques. These experimental data were then used to extrapolate virtual frictionless curves thanks to the help of a finite element model which simulated the experimental tests at different level of friction otherwise not achievable. In the end new materials coefficient for the visco-hyperelastic model are extrapolated and are ready to be used for the characterization of shock absorption properties of the sports flooring. It must be noticed that the FEM model present different issues and, in particular at high levels of friction, does not give an accurate prediction of experimental data. Further development is surely needed to improve the model which could result in a very useful tool to predict the behavior of sports surfaces materials.

Key-words: Rubber, Friction, Finite element, Viscoelastic, Hyperplastic, Artificial Athlete, Force Reduction

Abstract in lingua italiana

Il lavoro qui presentato si concentra sulla caratterizzazione di quattro materiali utilizzati per la produzione di piste di atletica con un modello visco-iperelastico, tenendo conto dell'influenza dell'attrito che agisce durante i test in compressione. Il modello sopra menzionato è stato precedentemente usato per determinare le proprietà di assorbimento dell'urto dei suddetti materiali attraverso un modello ad elementi finiti dell'atleta artificiale già utilizzato in altri lavori presenti in letteratura. In questa tesi, sono quindi stati realizzati test sperimentali (compressione e rilassamento degli sforzi) nelle minime condizioni di attrito possibili, insieme a misurazioni dei coefficienti di attrito delle gomme su diversi substrati e con diverse tecniche di lubrificazione. I dati ottenuti sono stati poi utilizzati per l'estrapolazione di curve virtuali a zero attrito grazie all' utilizzo di un modello a elementi finiti che può simulare i test sperimentali a diversi livelli di attrito. In questo modo nuovi coefficienti visco-iperelastici sono stati ricavati e possono essere utilizzati per una nuova determinazione delle proprietà di assorbimento dell'urto per le piste di atletica. Va notato che il modello FEM realizzato presenta alcune criticità, in particolare ad alti livelli di attrito non sembra dare una predizione accurata di ciò ritrovato sperimentalmente. Un ulteriore miglioramento del modello sarà utile per la realizzazione di uno strumento fondamentale nella caratterizzazione dei materiali per le pavimentazioni sportive.

Parole chiave: Gomma, Attrito, Elementi Finiti, Viscoelastico, Iperelastico, Atleta Artificiale, Force Reduction

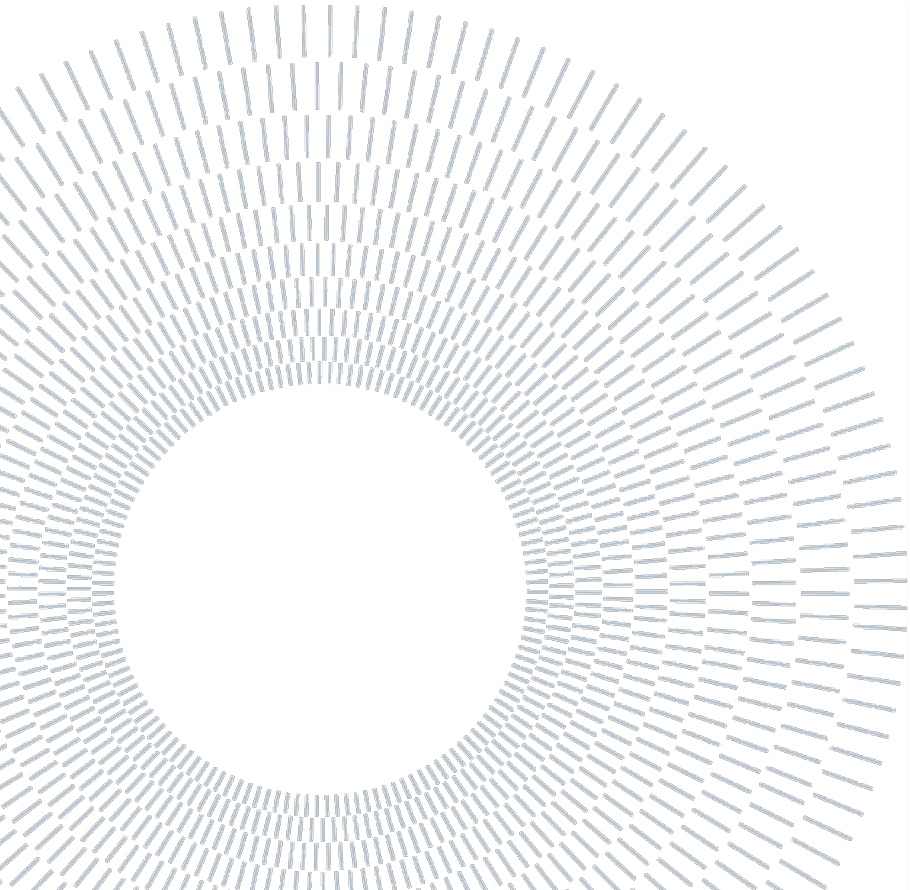

Contents

1. INTRODUCTION

1.1 Athletic tracks

1.1.1 Synthetic Athletic Tracks history

Synthetic athletic tracks first appeared in the mid-1960s [1] and were developed with the name of Tartan tracks manufactured by the American factory 3M [2]. The product was based on polyurethane and it was the first track of this kind to be used in Olympic Games, in particular it was installed for the 1968 Mexico City summer Olympics. Since then synthetic athletic tracks have become the most widely used type due to their great advantages including:

1-Durabilty

2-Low sensitivity to weather condition

3-Low need for maintenance

Fig. 1.1-1 Image of synthetic running track floor [3]

There are two main kinds of athletic tracks: prefabricated sheets and in-situ paved tracks. The former is manufactured in a dedicated plant and then transported and bounded to the substrate, the latter is instead produced directly in place [1].

1.1.2 Prefabricated tracks

Prefabricated tracks are produced under controlled conditions in a dedicated plant. The process starts from a mixture of natural and synthetic rubbers typically: natural

rubber (NR), styrene butadiene rubber (SBR) and ethylene propylene diene monomer rubber (EPDM). These materials are mixed together with fillers and other additives and the mixture is then calendered to create constant thickness sheets which are vulcanized in a continuous process. This kind of tracks, as shown in figure 1.1.2, is usually composed of two layers that are vulcanized together to form a continuous sheet with no junction. The installation of prefabricated sheets requires a high degree of skill and an accurate preparation of the substrate. [1]

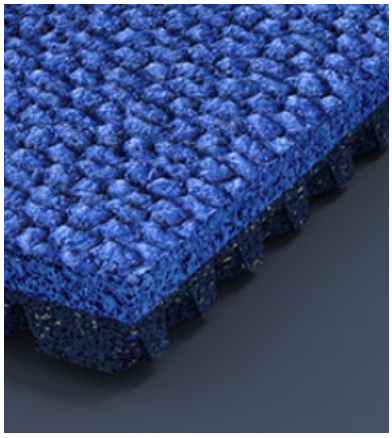

Fig. 1.1-2 Example of prefabricated sheet by Mondo Spa [4]

1.1.3 In situ paved

Tracks can be also fabricated by mixing raw materials directly in situ and casting them on the surface through the use of a paving machine as the one shown in figure 1.1.6. There are many ways to produce them.

Cast elastomer

The first technology consists in casting a polyurethane resin, prepared by mixing a liquid polyol and an isocynate in situ, mixed with rubber crumbs on the substrate; then EPDM rubber granules are put on the top of the resin and finally the system is cured.

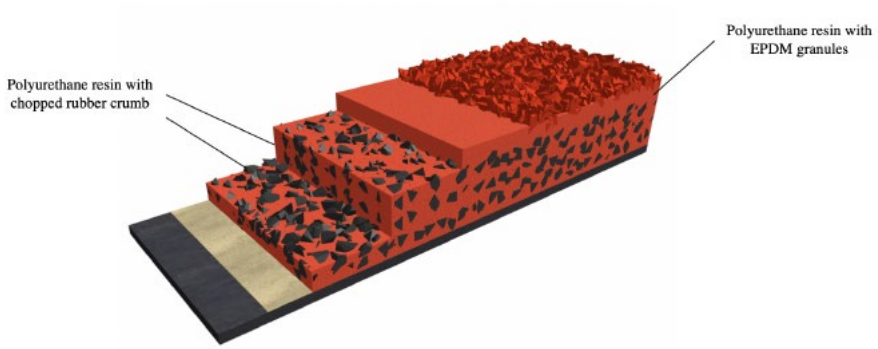

Fig. 1.1-3 Example of Cast elastomer system [5]

An alternative is the application of a mixed polyurethane layer and then of a second layer of polyurethane and chopped rubber on the top of the first. Finally a third layer with EPDM granules can be applied as finishing. Both methods belong to the cast elastomer athletic tracks family (figure 1.1.3). Such surfaces are strong and durable, provided they are correctly formulated using compatible raw material ingredients in right proportion.

Resin Bounded

Another way to produce this kind of tracks is to use resin-bounded rubber crumb (figure 1.1.4). The crumb is mixed with a PU resin, which is usually moisture curing in this case, and cast on the base by the use of a paving machine. After curing a finishing layer is applied by spraying resin with rubber aggregates. This system is less expensive than the one described above as it uses less polyurethane resin.

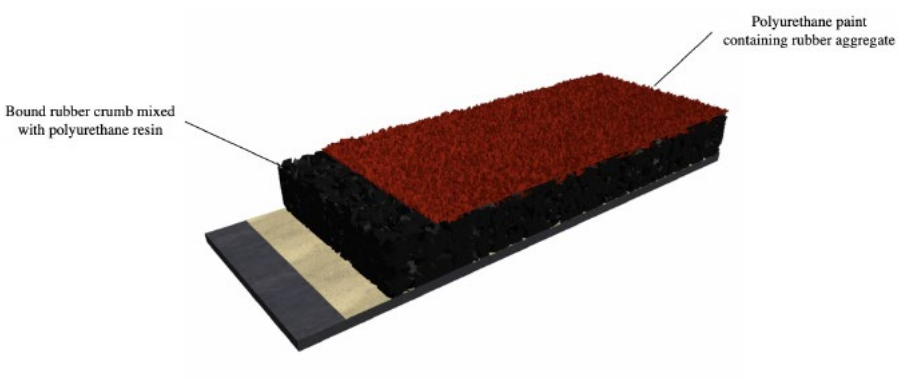

Fig. 1.1-4 Example of Resin bounded system [5]

Composite System

A composite system combining cast elastomer and resin-bound tracks can also be used and it is usually called sandwich system (figure 1.1.5). The composite track is made of a resin-bound layer of about 9 mm on the top of which a cast elastomer layer is applied. This system mixes the high durability of the cast elastomer track with the economic advantage of the resin-bound method.

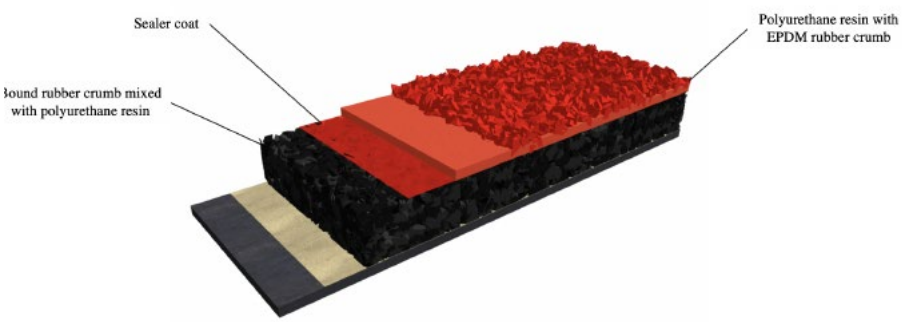

Fig. 1.1-5 Example of Composite system [5]

Fig. 1.1-6 Paving machine [6]

1.2 Tracks requirements and approval

The main regulating authority for athletic tracks requirements is the Word Athletics (WA), formerly called International Association of Athletic Federations (IAAF). In its manual [1] World Athletics provides all the requirements an athletic track must satisfy as well as specifications about testing procedures.

1.2.1 Dimensions

Tracks, as shown in figure 1.2.1, have an oval shape with a total length of 400 m and an optimal radius of 36.5 m. As a consequence the straights have a length of 84.39 m. All lanes have a width of 1.22m ± 0.01m. The 400m Standard Track has 8, 6 or occasionally 4 lanes but the last variant is not used for international running competitions. The 400m measure represents the theoretical line of running which is 0.3 m offset from the inner edge of the track thus measuring $L = 2 * (36.8\pi + 84.39) = 400.001\ m$.

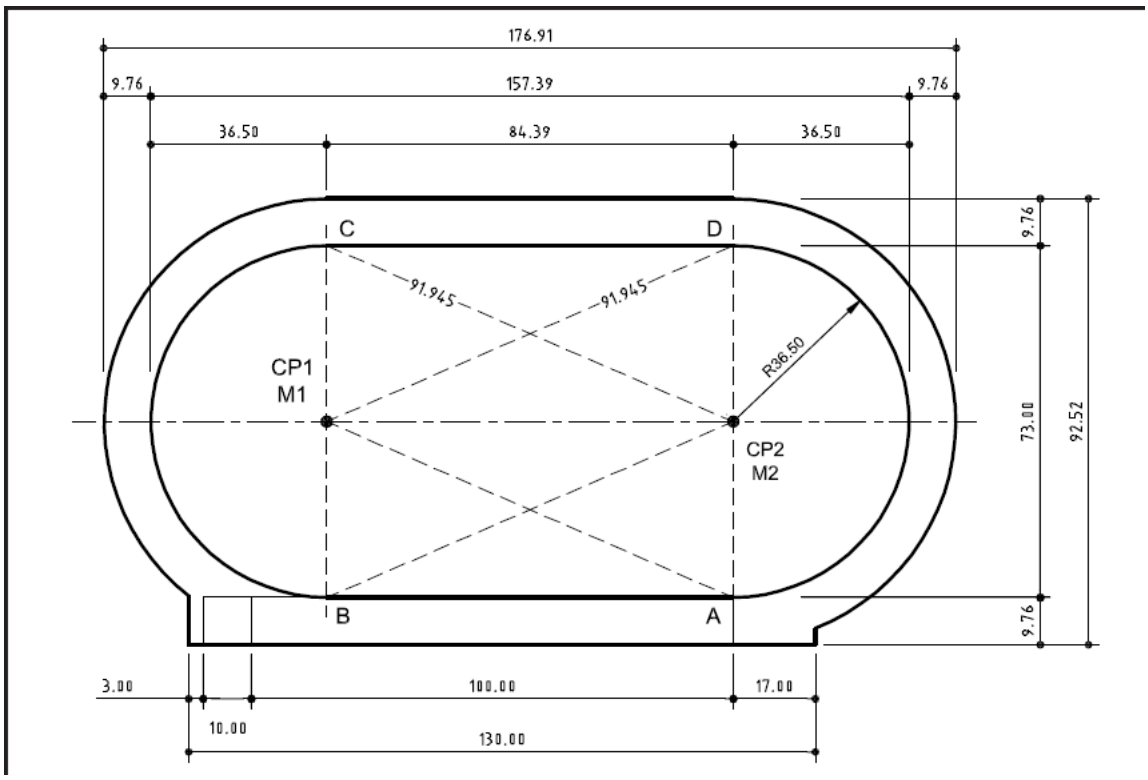

Fig. 1.2-1 Scheme representing dimensions of a track from the WA manual [1]

1.2.2 Durability

The first requirement of synthetic tracks is durability; in fact tracks should retain their mechanical and physical properties as long as possible. Wear, freeze and thaw cycles, UV exposure and water are the main causes of degradation and obviously outdoor tracks are the most hit by these agents. The most frequent consequences of degradation are: delamination of the surface from the base or itself, discoloration, loss of integrity and water bubbling.

1.2.3 Other requirements

There are many other requirements listed in the WA manual. For example a control on imperfections evenness and thickness should be done. The track must not have slopes exceeding 4 mm over 6 m or 3 mm over 1m. Also a minimum thickness is set by the WA because too low thicknesses may not allow to run with spiked shoes. No upper limit is proposed even if excessively high thicknesses may result in too soft surfaces; it was in fact proved in the previous work by L. Andena et al [7] that the thickness limit is strictly related to the force reduction value. This relation is described in detail in the following chapter.

1.3 Mechanical Testing

There is a set of different tests that a track should undergo before being put in service.

1.3.1 Force reduction

The force reduction test is described in the UNI EN 14808 standard and it is a way to determine the shock absorption of sport surfaces which is defined as the *"ability of a sports surface to reduce the impact force of a body falling onto the surface"* [8]. Energy absorbed by a material during an impact can be described as [9]:

$$E_{stored} = \frac{1}{2} * Kx^2 \qquad 1.1$$

Where K is the stiffness of the material and x the deflection. The standard separates the force reduction test for point elastic and area elastic surfaces. The former is a surface which deforms only around the point of application of the force while the latter deflects over a larger area. Area elastic are typically wooden sport floorings

used for sports like: ball games, dancing and roller hockey. Point elastic surfaces can instead be used for gymnastics and fighting sports. Finally two other types of floorings exist: combined-elastic, which consist of an area elastic base combined with a point elastic layer, and mixed elastic which is made of a point elastic sub-layer covered by a hard coating [10].

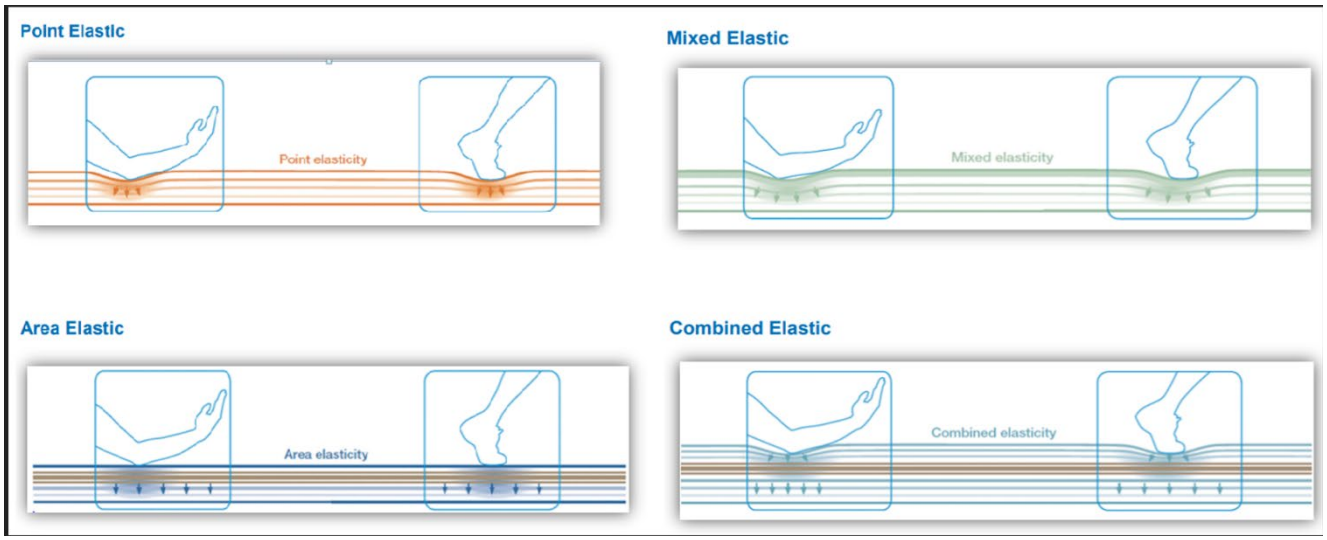

Fig. 1.3-1 Different types of sport floorings [10]

Samples used to test area-elastic surfaces are bigger (3.5X3.5 m) than point elastic samples (1X1 m). In this work we are going to focus only on point elastic surfaces. During the test a weight of 20 kg falls from a height of 120 mm over a spring of stiffness 2000 N/mm and diameter 69 mm. The test piece is positioned under the spring and over a substrate made of rigid and smooth concrete. The test is first performed without the test piece to measure the response of the bare substrate and then repeated with the test piece to finally measure the force reduction as [8]:

$$R = \left(1 - \frac{F_t}{F_r}\right) * 100 \quad 1.2$$

Where F_t is the peak force measured during the test with the specimen and F_r is the peak force given by the impact with concrete. The value of F_r shall lie in the range $6.35<F_r<6.85$ kN. As specified by WA the R value should be between 35% and 50%.

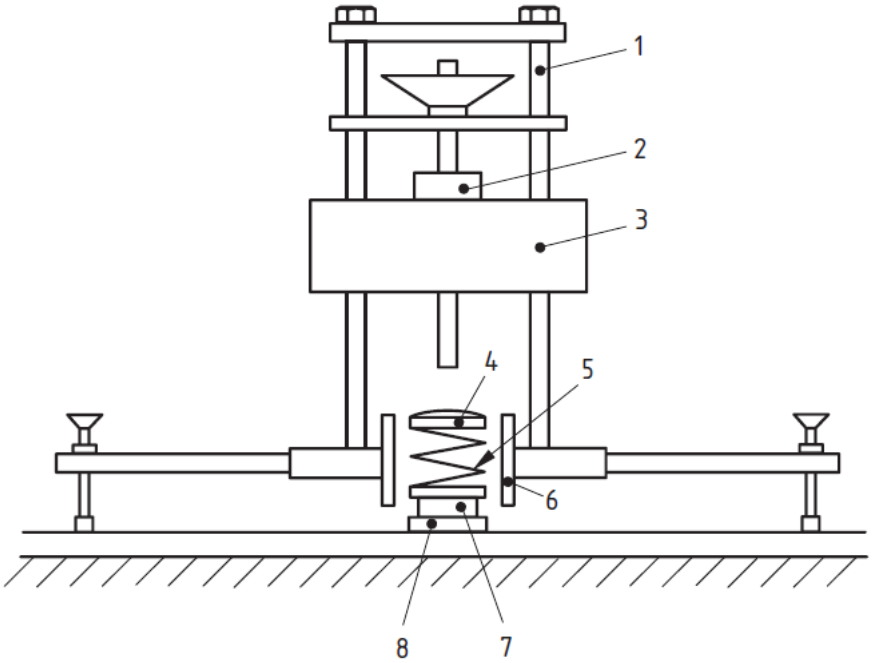

Key

1	guide for the falling weight	5	spring
2	electromagnet	6	guiding tube
3	falling weight	7	force sensing device
4	upper plate	8	base plate

Fig. 1.3-2 Apparatus for Force reduction test [8]

1.3.2 Vertical Displacement

The apparatus is similar to the one described in paragraph 1.3.1 for force reduction test except for the use of a spring with length 69 mm and stiffness of 40+-1.5 N/mm, furthermore a smaller steel base plate is used. Two horizontal projections, visible in figure 1.3.3, are added on testing foot for the displacement sensors which are symmetrically positioned with respect to the axis of the apparatus and have a maximum uncertainty of 0.05 mm over a range of +-10mm. The magnitude measured is the maximum displacement of the test piece described by equation 1.3 [11]:

$$D = \frac{1500N}{F_{max}} * f_{max} \qquad 1.3$$

Where f_{max} is the maximum deformation of the sports floor in the falling weight axis in mm and F_{max} is the maximum force measured. In this case the WA set the

acceptable range of D as 0.6<D<2.5 mm. Higher values can produce instability of the foot while lower values can result in a too rigid surface.

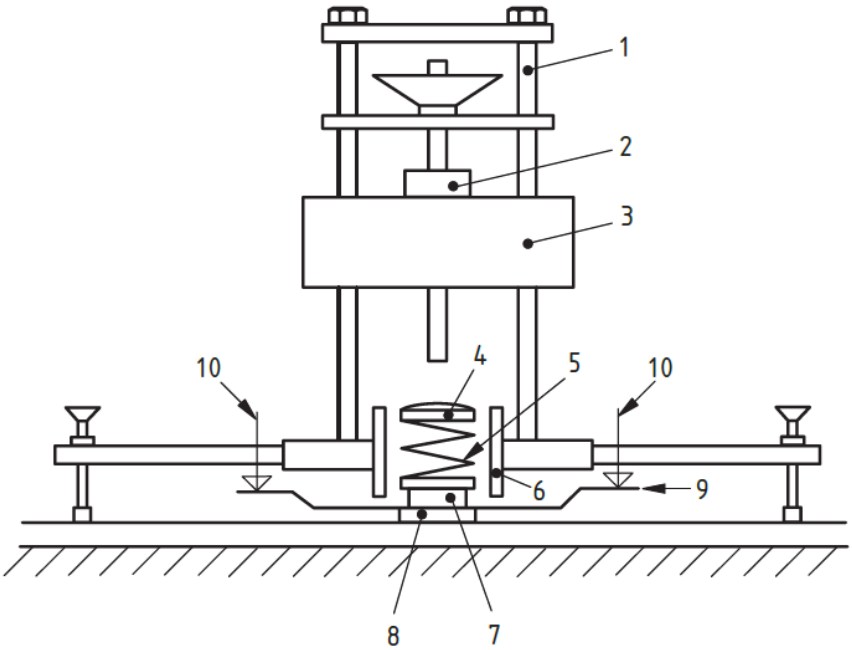

Key

1	guide for the falling weight	6	guiding tube
2	electromagnet	7	force sensing device
3	falling weight	8	base plate
4	upper plate	9	horizontal projections
5	spring	10	sensors (pick up)

Fig. 1.3-3 Apparatus for vertical displacement test. Notice that horizontal projections are added for the displacement sensors. [11]

1.3.3 Friction

Tracks friction can be measured in two ways. The first is the portable skid resistance tester: the apparatus is shown below in figure 1.3.4 and it is made of a pendulous which oscillates while just scraping the track surface [1].

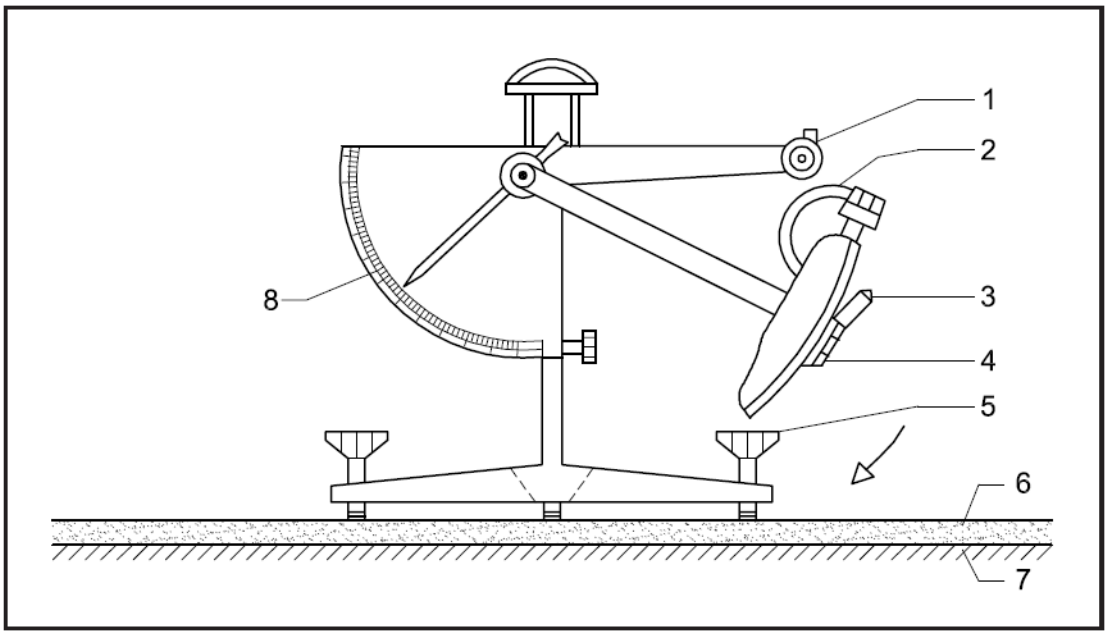

Figure 3.1.3.6a - Portable skid resistance tester (Friction Method A)

1 Release catch	5 Foot of support
2 Lifting handle	6 Synthetic surface
3 Pin F	7 Base
4 Rubber slider	8 Scale

Fig. 1.3-4 Portable skid resistance tester from the WA manual [1]

In the second method (figure 1.3.5) instead a torque is applied to a rotating shaft which has a foot in contact with the surface track. The frictional resistance to rotation of the shaft is measured and knowing the normal force pressing the foot against the surface it is possible to compute the final friction coefficient.

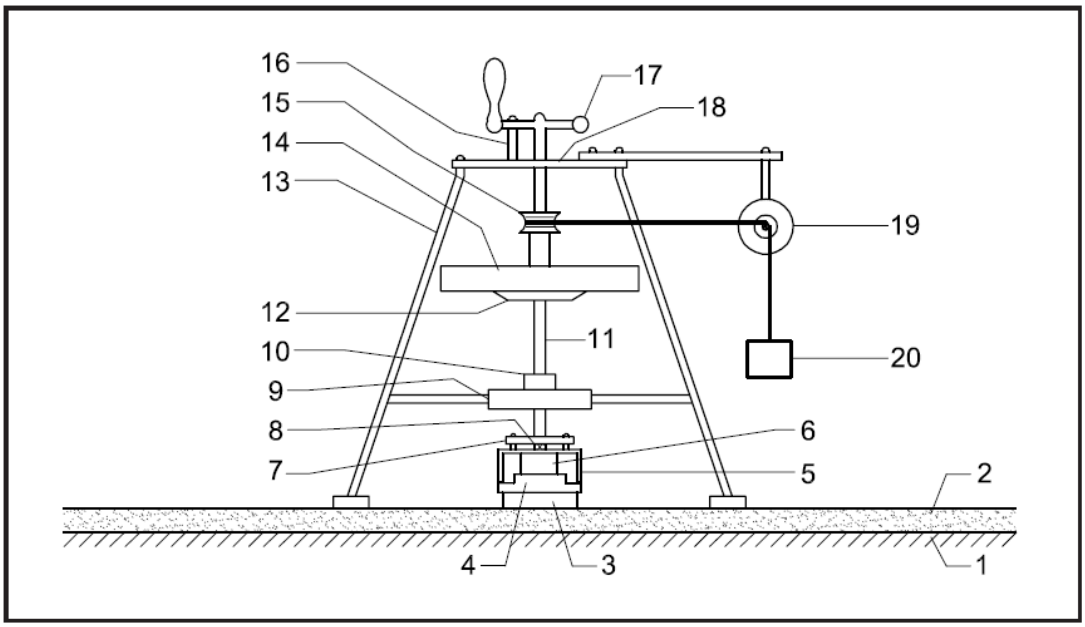

Figure 3.1.3.6b - Sliding resistance tester (Friction Method B)

1 Base	11 Threaded spindle
2 Synthetic surface	12 Support flange
3 Bottom plate	13 Frame
4 Lower part of test foot	14 Weights
5 Upper part of test foot	15 Winding drum
6 Electrical detector	16 Catch lever
7 Soft rubber disc	17 Handwheel
8 Ball joint	18 Plain bearing
9 Ball bearing holder	19 Potentiometer for measuring the speed of rotation
10 Ball bearing	20 Freely suspended weight

Fig. 1.3-5 Sliding resistance tester. [1]

The friction coefficient of tracks should be higher than 0.5 even in wet conditions.

1.3.4 Tensile properties

The WA provides also minimum tensile properties for the track material. The tensile strength should be 0.5MPa for non-porous surfaces and 0.4MPa for porous surfaces. For all surfaces, the elongation at break shall be a minimum of 40% [1]. The specimens for the tensile test are shown below in figure 1.3.6 and can be either provided by the manufacturer or cut from the tack itself.

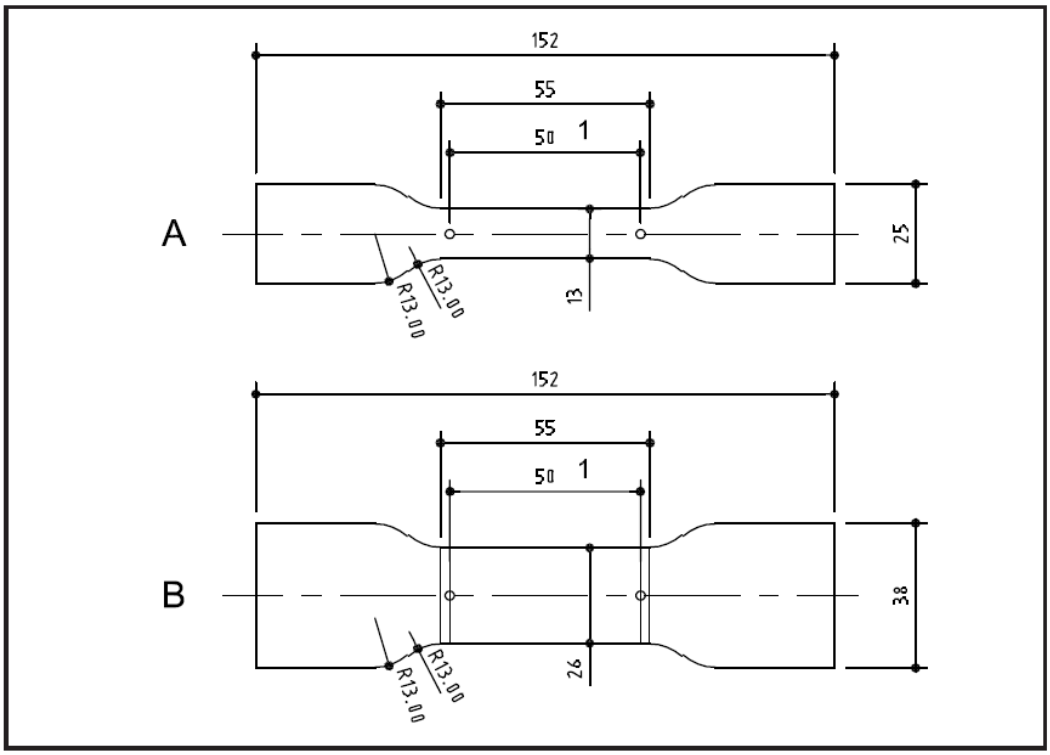

Figure 3.1.3.7 - Tensile specimens (Dimensions in mm)

Sample A
Sample B

Fig. 1.3-6 Specimens for tensile test on track. [1]

WA specifies two kind of samples that are shown in figure 1.3.6. Even if sample B is accepted the document strongly suggest the utilization of Sample A. The thickness of both samples corresponds to the one of the track [1].

1.3.5 Tests on physical properties

Other tests on physical and mechanical properties are described in detail in the document by the WA. Here we only list them: imperfections, evenness, thickness, drainage and color.

1.4 Track design for athlete performance and health

During running energy is transferred from the athlete to the track and is then returned by the track to the athlete. Every time the athlete kinetic or potential energy is transformed into elastic energy stored in the track material we have some energy losses due to vibrations, heat generation and, mainly, because of viscoelastic behavior of rubber. Energy stored in the material can be estimated through equation 1.1 if properly returned to the athlete it can greatly improve its performance like a trampoline effect. Energy dissipated instead is found by a simple balance of the total energy given to the system like in the equation 1.4 below [9]:

$$E_{returned} = E_{input} - E_{dissipated} \qquad 1.4$$

Although the stored energy is important to improve athlete performance the ability of the floor to dissipate energy and reduce vibrations can decrease the risk of running injuries. For this purpose also the shock absorption ability of the surface, as defined above (1.3.1), is fundamental to reduce the maximum force acting on the athlete's body during impact.

1.4.1 Optimization

In order to optimize the performance of the athlete we can act on two elements: material properties of the track and its geometrical design. For what concerns material properties some studies [9] suggest that a good stiffness for athletic tracks lies between 160-320 kN/m. The material not only should be able to store energy but it should also return it in the right location and time. The timing of energy release is directly proportional to the surface stiffness, if this timing is matched with the one of the activity the athlete is likely to have an energy return when it is more needed [9]. The use of a structured track can deeply influence the performance of the athlete. In fact the addition of a geometrical pattern changes the overall stiffness of the track usually decreasing it; thus, allowing for more deformation, it is possible to store more energy. Furthermore thanks to the directionality of the pattern the stiffness may vary according to the direction, in this way, as showed in figure 1.4.1, the geometry of the track becomes fundamental to determine the direction in which forces are applied by the surface to release the stored energy [9]. Therefore geometry and material of the track can be engineered to have a surface which returns energy to

the athlete at the right time and with forces in the right direction [9]. To finally optimize these parameters finite element analysis can become a fundamental tool to predict the elastic behavior of the track system. An example is the investigation of the rectangular or honeycomb pattern used by Mondo Spa as done by L.Andena et al which will be described in detail in the next chapter [12]. The pattern can vary according to geometrical drawing, depth and size of the cells. All these characteristics have been proven to greatly affect the elastic behavior of the floor.

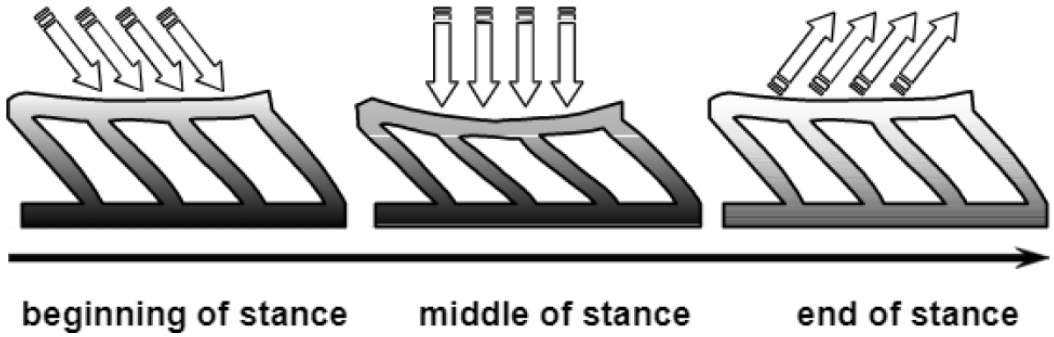

Fig. 1.4-1 Behavior of 2D structured track during running

1.4.2 Running injuries

Running induces a relative high risk of injuries, in particular overuse injuries are the most common ones. They are caused by shockwaves propagating in the lower extremities due to the foot impact on the floor. Many factors are used to study the influence of the floor type or the running technique to the risk of injuries related to running. For example the foot strike pattern (FSP) can change the probability and the type of injury; as suggested by [13] a rear-FS, where the heel touches the ground first, is responsible for injuries at the knee and the hip while on the contrary a non-rear-FSP can be more dangerous for the ankle and the Achille's tendon [13]. The floor material compliance can be responsible for health issues, in this case parameters that are usually studied are the vertical loading rate VLR and the vertical ground reaction force VGRF. These parameters are strongly related to one another and they can be computed from the Force-time graph of the foot impact on the ground as it is possible to observe from image 1.4.2. This graph typically shows two peaks the first is called impact peak and the second propulsion peak. The VLR is the rate at which the VGRF reaches the impact peak, so it is the slope of the first part of the graph [14]. The two parameters are related to running injuries and can depend on both floor and, of course, shoes stiffness. This last observation has been well proved by the work of L. Andena et al [15] in which the dependence of the loading rate was studied, also through the use of finite element analysis, as a function of stiffness and

thickness of the floor material. In this case the magnitudes studied were three: the well-known force reduction value, the initial loading rate (ILR) defined as the slope of the force versus time curve at time of impact *t=0*s and finally the average loading rate (ALR) taken as the average slope of the same curve between *t*=0.2s and *t*=0.8s as shown below (Figure 1.4.3). The study showed that the ILR is proportional to the stiffness of the material and decreases as the thickness increases, however it is independent on the FR value. Figure 1.4.4 shows the behavior of ILR for two real tracks A and B and for a natural rubber which is stiffer; furthermore the ILR of 2 fictitious stiffer materials is plotted thanks to the use of a 2D numerical simulation of the FR tests which showed very good agreement with experimental results obtained for the other materials. The model used for the study is described in detail in the following chapter [16].The ALR instead is plotted against the FR value and seems to be strictly related to it.[15]

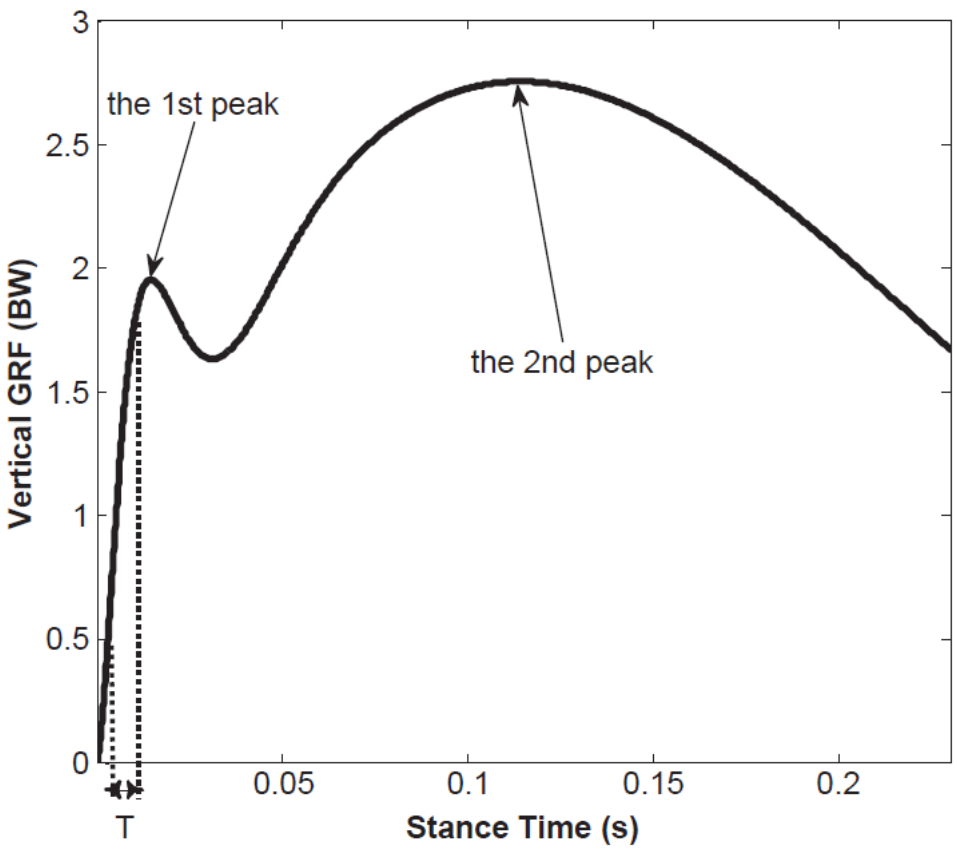

Fig. 1.4-2 VGRF versus stance time graph [14]

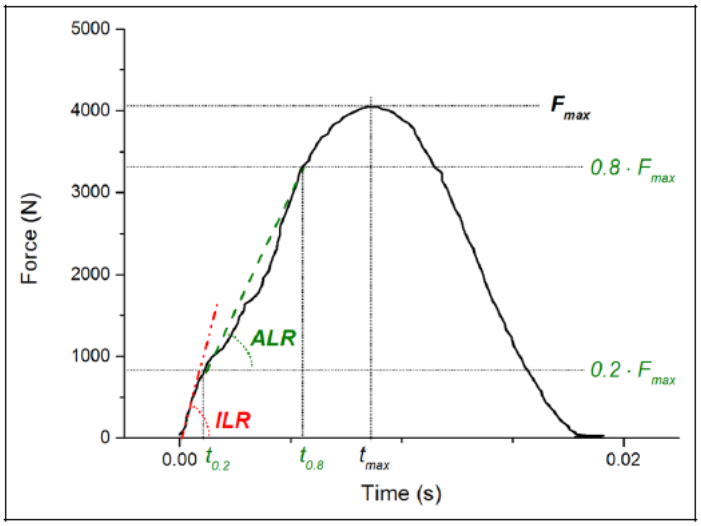

Fig. 1.4-3 Graphical meaning of the ILR and ALR magnitudes [15]

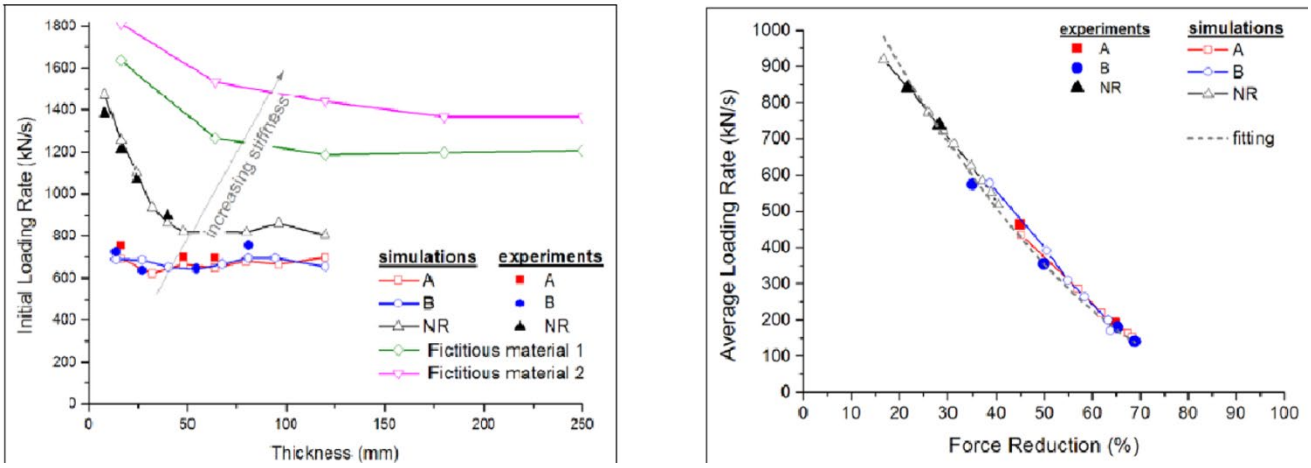

Fig. 1.4-4 On the left ILR versus thickness graph at different stiffness levels. On the right the correlation between FR and ALR values for different materials. Notice the good agreement between numerical and experimental results. [15]

2. PREVIOUS WORK

In this chapter a collection of literature works aimed at studying the value of Force Reduction for different track systems is presented. The focus is on how this value changes according to thickness of the track, coefficients of track material and geometrical design of the track. Common ground for all the articles analyzed here is the use of finite element analysis which is exploited to extrapolate the right material coefficients for the track and what is most important to study the FR test result itself.

2.1 Force reduction

Previous literature works studied the dependency of the force reduction value on the thickness of the sample and on its dynamic modulus measured through DMA tests. Different track materials (A, B, C, D, E, F and G) where tested, considering them as homogeneous samples regardless of their real geometrical pattern, along with other polymeric materials here listed: Polyurethane (PU), Polyethylene (PE), Polybutadiene (PB) and natural rubber NR [7]. What has been found is that FR increases with the thickness of the sample and it usually reaches an asymptotic value. The dependency on thickness can be described by an exponential function as in equation 2.1:

$$FR(s) = FR_{inf} * (1 - e^{-\frac{s}{s_0}}) \quad 2.1$$

Where FR_{inf} is the asymptotic value of force reduction which occurs for thicknesses s much higher than s_0. Both FR_{inf} and s_0 parameters are material dependent and in particular FR_{inf} seems to decrease with the dynamic modulus of the material. It is to be noticed that the usual thickness of tracks is lower than the value at which FR is equal to FR_{inf}, therefore a strong dependency on thickness is expected.

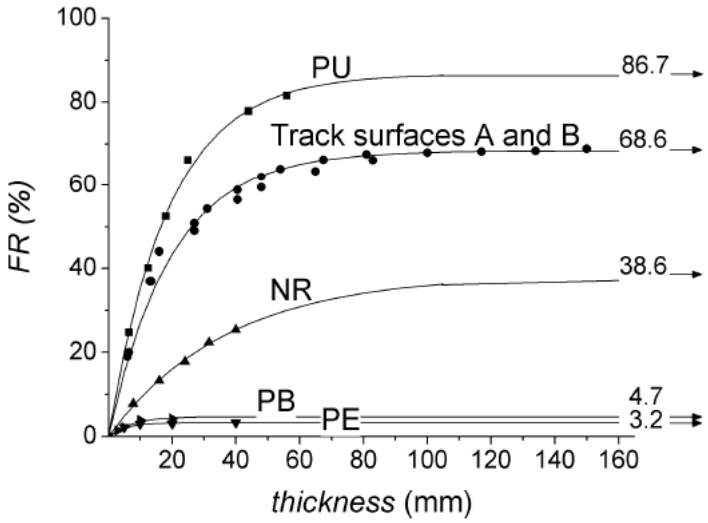

Fig. 2.1-1 FR versus thickness for some of the tracks (A and B) and for some polymeric materials [7]

Finally the dependency of the asymptotic value FR_{inf} on the dynamic mechanical analysis (DMA) coefficients of the materials was studied. As already mentioned this parameter is proportional to the inverse of the dynamic moduli $|E^*|$ (complex modulus), E' (storage modulus) and E'' (loss modulus) as shown in figure 2.1.2. No relevant correlation was instead found with the loss factor (tan(δ)) of the material. Even s_0 didn't seem to have any correlation with the dynamic moduli or with the loss factor and it was described as a *"sensitivity of the material under test to the thickness"* [7].

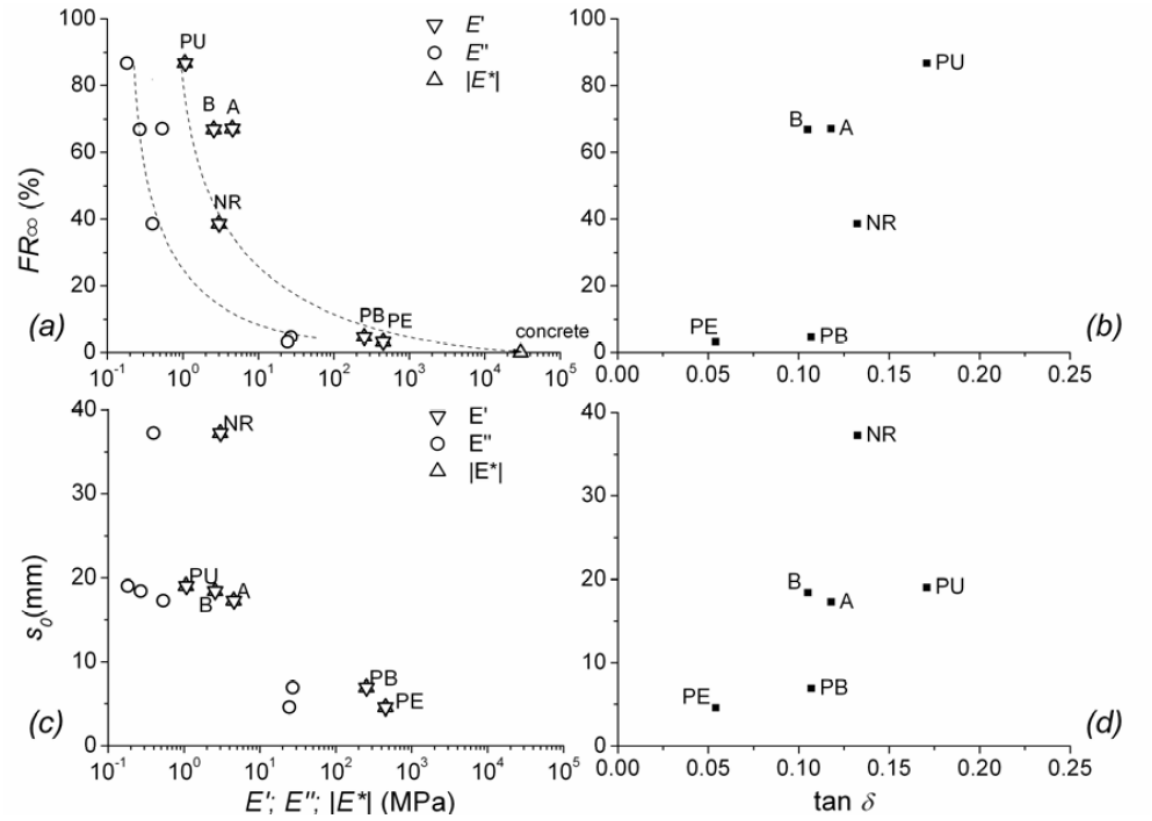

Fig. 2.1-2 Correlations of the two fitting parameters FR_{inf} and s_0 with: (a)-(c) the moduli (E′, E″, |E|) and (b)-(d) the loss factor of the materials. The lines drawn in (a) are just guidelines and not actual fits of the data [7].*

2.2 2D axisymmetric model

In the following studies [16], [17] instead a 2D model of the artificial athlete apparatus described in paragraph 1.3.1 was created to investigate the ability of finite element method to predict the *FR* value. In the model, shown in figure 2.2.1, all steel parts were considered as rigid bodies the spring and load cell of the *artificial athlete* were instead modeled as elastic springs, with masses of 1.460 kg and 0.518 kg and stiffness of 2 kN/mm and 1 MN/mm. The sample was described as hyperplastic deformable body while the substrate (two substrates were investigated: PE or concrete) as a linear elastic deformable body. The element type used was CAX4RH. The hyperelastic coefficients of the material were computed from uniaxial compression tests data sets. Different materials were tested: a track material A and a natural rubber for comparison, both of them showed a weak rate dependency

underlined by compression tests at different rates(from 0.005 s^{-1} to 0.6 s^{-1}). To simulate the *FR* test parameters at a rate of 60 s^{-1} are needed, at this purpose coefficients at this rate were extrapolated from the coefficients obtained through non-linear fit of experimental curves by using a simple linear fit of said parameters as a function of the logarithmic stretch rate (where the stretch is defined as current length of the specimen over initial length $\lambda = \frac{L}{L_0}$), the procedure is summarized by figure 2.2.2. The finite element model was then validated through the comparison of numerical simulations of drop weight test and experimental results that had been generated at this purpose, the results showed quite good agreement as the error peak force was less than 3%.

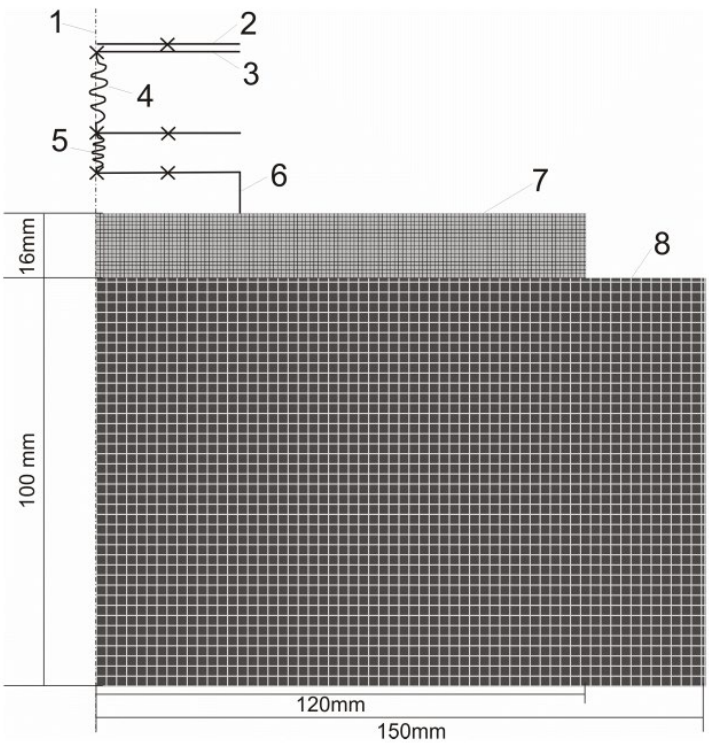

Fig. 2.2-1 Sketch of the FE model of the FR test 1 axis of symmetry, 2 falling body, 3 upper plate, 4 spring, 5 load cell, 6 base plate, 7 test specimen, 8 substrate [16]

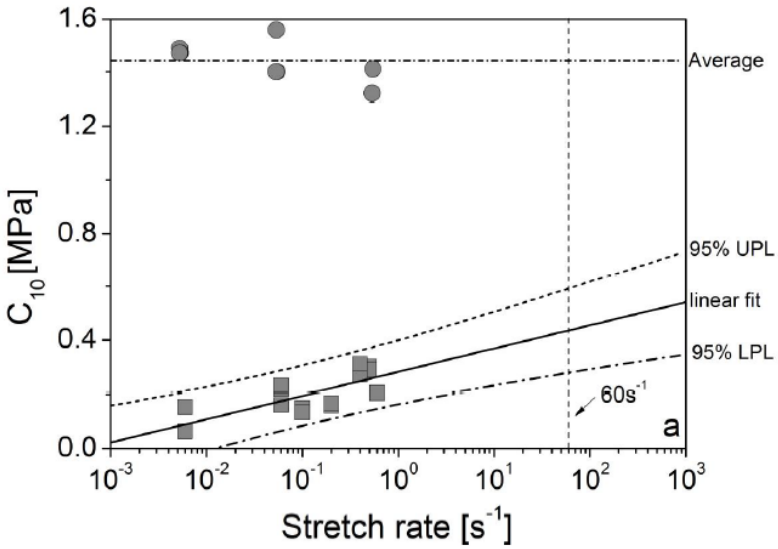

Fig. 2.2-2 Example of extrapolation of C_{10} coefficient at 60 s^{-1} [16]

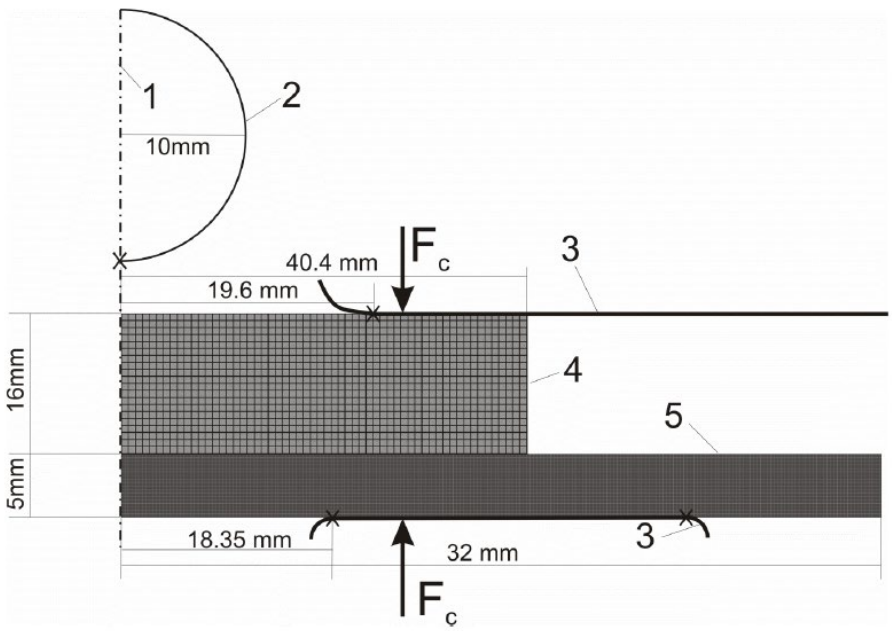

Fig. 2.2-3 Sketch of the FE model of the drop weight tower test 1 axis of symmetry, 2 striker, 3 clamping plates, 4 material A specimen, 5 HDPE substrate [16]

Finally the model was used to simulate *FR* tests and in particular the prediction of the force reduction with a varying thickness of the sample was studied. The FE model seemed to well predict the fact that *FR* reaches an asymptotic value after a certain thickness and gave also good estimation of FR_{inf}. The dependency on the material modulus in this case evaluated from the Mooney-Rivlin constants ($E=6*(C_{10}+C_{01})$ see chapter 3) was also well predicted for the materials tested, in addition virtual materials with different stiffnesses were tested in [17] to understand the behavior of FR_{inf} in a wider range of stiffness values (fig.2.2.5). Finally the numerical results matched very well the experimental data both in terms of the full force–time history (and hence in terms of evolution of the elastic energy stored in the track material) and in terms of maximum force value [16].

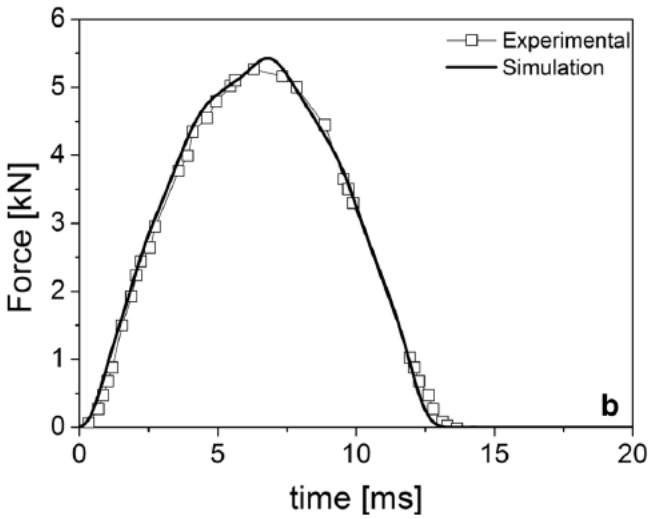

Fig. 2.2-4 Comparison between FR experiments and simulations, performed on 16-mm-thick samples of NR. [16]

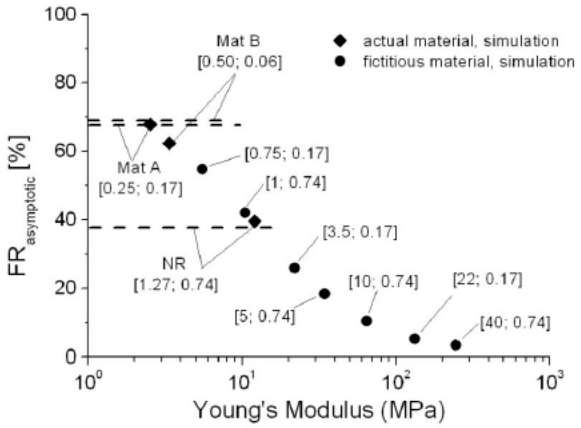

Fig. 2.2-5 Asymptotic FR vs. Young Modulus of the three investigated materials and other fictitious ones: numbers in parentheses are relevant values of C_{10} and C_{01} while dashed lines represent FR limiting values, determined experimentally for material A, B and NR [17]

2.3 3D Model

The simplified 2D model above described neglected the real track structure, considering it as a single layer of material having homogenized properties. In the following studies [12], [18], a new 3D model was developed to accurately describe the structure of multi-layered tracks, with properties and geometrical construction (e.g. solid or honeycomb) differing from one layer to another. The 3D model required definition of the intrinsic properties of each constituent material, including that of the honeycomb structure; for the latter, it was very difficult to extract samples suitable for the evaluation of material properties. Hence, a detailed FE model was developed for the compression tests, using the general-purpose commercial code Abaqus. The 3D model gave results in agreement with the experimental *FR* curves [12], [18] and the improvement consisted in taking into account, and correctly describing, the actual geometrical structure of the honeycomb base layers, which proved to have a considerable effect on the shock absorption ability of the overall track, thus making it a useful tool for the optimization of the running pavement performances. In particular in [18] the effect of geometrical design of structured tracks in terms of depth and size of the cells was studied. In this study 3 complete track material were tested (A, D and H) with different finishing and bottom layers and with different geometries as shown in figure 2.3.1. Hyperelastic constants of the finishing material were found with simple uniaxial compression tests while for the bottom layer a 3D simulation of the complete track was used as mentioned above. FR 3D simulations were than run with different cell geometries for tracks A and H as shown for the

latter in figure 2.3.2. For both track a dependency of the *FR* value and the geometry was found demonstrating that there is the possibility to optimize the track design and that the 3D FEM model is a fundamental tool for this purpose. [18]

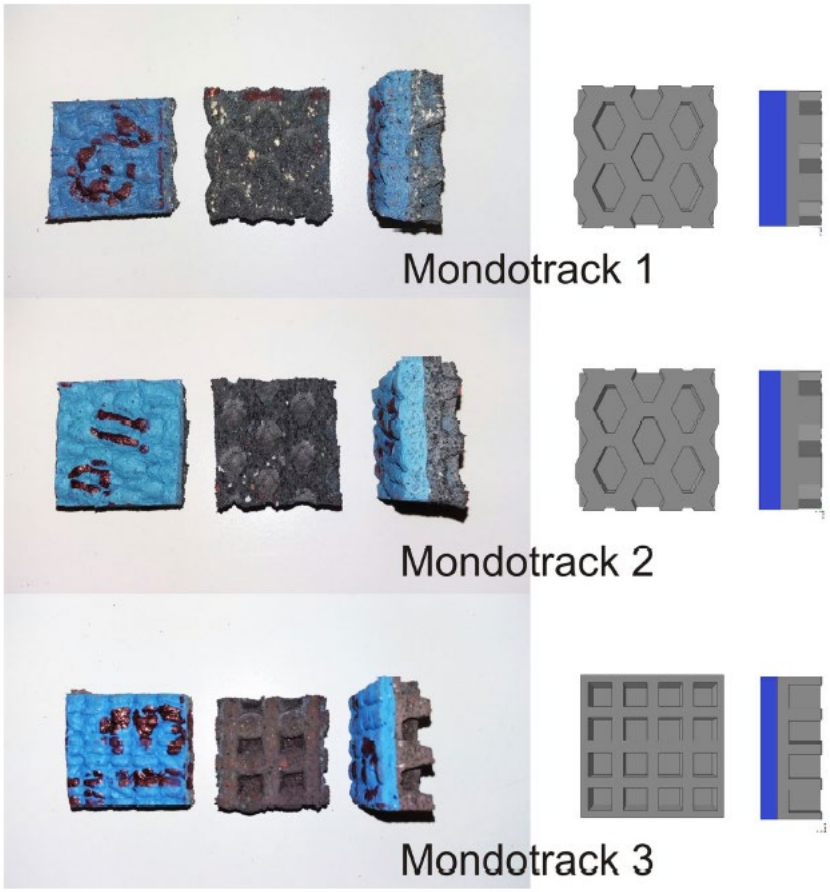

Fig. 2.3-1 Materials tested in [18]

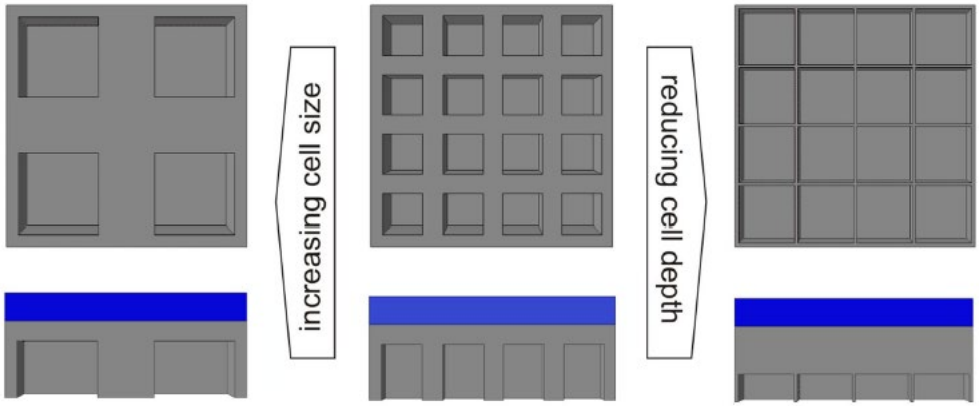

Fig. 2.3-2 Example of variation in geometrical design for track H [18]

2.4 Visco-hyperelastic model

Finally in the thesis *"A visco-hyperelastic numerical model for elastomeric materials"* by F. Ramusino [19] viscoelastic properties of 4 different materials (named CF, LG, B and EI) were studied to understand their influence on the force reduction value. The rubber mixtures studied correspond to the finishing and bottom layers of the tracks described in [18] as shown in table 2.1.

Track	Finishing	Base	Base pattern
A	B	CF	Honeycomb
D	EI	CF	Honeycomb
H	EI	LG	Rectangular

Table 2.1 Composition of tracks [18], [19]

First the materials were characterized through uniaxial compression tests and stress relaxation tests. The former were realized at different strain rates, as done in the

previous works, in particular 3 strain rates were studied: 0.6,0.06 and 0.006 s^{-1} which corresponded to 180,18 and 1.8 mm/min crosshead displacement. To reduce the influence of friction a PTFE film was put between the sample and the disks (figure2.4.1). The tests were conducted down to a stretch of 0.6. Two kinds of stress relaxation tests were performed to find viscoelastic properties of the material: one with a fixed stretch of 0.7 and the other with a stretch of 0.9. Both tests had an initial stretch ramp with constant slope (0.06 s^{-1}) and the deformation was held for 300 s. Preliminary cyclic load-unload compression tests showed that no Mullins effect occurred in the samples studied

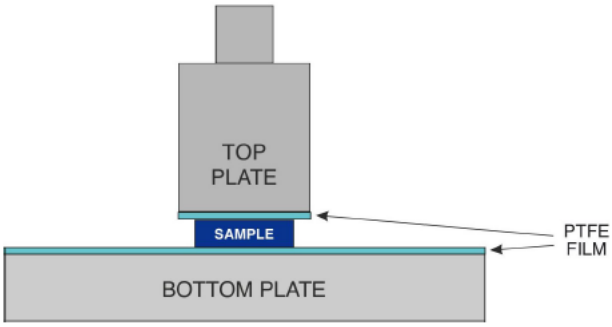

Fig. 2.4-1 Configuration of compression tests [19]

2.4.1 Constitutive model

In this paragraph the Visco-hyperelastic model used in the previous work by F.Ramusino [19] and inspired by the work of Goh et al [20] is briefly presented. The constitutive model expresses the stress as the product of two distinct functions: a strain-dependent function, $\sigma(\varepsilon)$ having the dimension of stress and a dimensionless time-dependent function, $g(t)$, so that:

$$\sigma(\varepsilon;\ t) = \sigma_0(\varepsilon)\ g(t) \qquad 2.2$$

Where σ is the stress at strain ε and time t. The strain-dependent function can either be linearly elastic, or non-linearly elastic through various forms of hyperelastic potential. The time-dependent function can be represented by a Prony series:

$$g(t) = g_{inf} + \sum g_i e^{-\frac{t}{\tau_i}} \qquad 2.3$$

Where g_{inf} and g_i are dimensionless constants defined as:

$$g_i = \frac{G_i}{G_0} \qquad 2.4$$

g_i is related to g_{inf} through the following condition:

$$1 = g_{inf} + \sum g_i \qquad 2.5$$

Given a certain strain history the stress can be computed through the following convolution integral:

$$\sigma(t) = \int_0^t g\,(t-s)\frac{d\sigma_0}{ds}\,(t-s)ds \qquad 2.6$$

Which, in turn, can be split into a long-term elastic and viscoelastic contribution:

$$\sigma(t) = \sigma_0(t)g_{inf} + \sum \int_0^t g_i e^{-\frac{t-s}{\tau_i}} * g\,(t-s)\frac{d\sigma_0}{ds}\,(t-s)ds \qquad 2.7$$

Where we can define the integral in the following way:

$$\int_0^t g_i e^{-\frac{t-s}{\tau_i}}\frac{d\sigma_0}{ds}\,(t-s)ds = h_i(t) \qquad 2.8$$

The problem can be solved efficiently using the Taylor algorithm, based on finite time increments. For a generic time interval (t_n; $t_{(n+1)}$), the time step Δt is given as:

$$\Delta t = t_{n+1} - t_n \qquad 2.9$$

Therefore, the exponential term in the integrand can be written as:

$$e^{-\frac{t-s}{\tau_i}} = e^{-\frac{t_n}{\tau_i}} e^{-\frac{\Delta t}{\tau_i}} \qquad 2.10$$

And the term h_i:

$$h_i(t_{n+1}) = e^{-\frac{\Delta t}{\tau_i}} * h_i(t_n) + \int_0^t g_i e^{-\frac{t_{n+1}-s}{\tau_i}} \frac{d\sigma_0}{ds}\,(t-s)ds \qquad 2.11$$

The differential term $\frac{d\sigma_0}{ds}$ can be expressed in terms of discrete time steps:

$$\frac{d\sigma_0}{ds} = \lim_{inf}((\sigma_0^{n+1} - \sigma_0^n)/(\Delta t)) \qquad 2.12$$

Substituting Eq. 2.11 into Eq. 2.12 and solving the integral analytically leads to a recursive formula for updating the stress $\sigma(t_{n+1})$ in Eq. 2.7:

$$\sigma(t_{n+1}) = \sigma_0(t_n) g_{inf} + \sum e^{-\frac{\Delta t}{\tau_i}} * h_i(t_n) + g_i * \frac{1-e^{-\frac{\Delta t}{\tau_i}}}{\frac{\Delta t}{\tau_i}} [\sigma_0(t_{n+1}) - \sigma_0(t_n)] \qquad 2.13$$

2.4.2 Fitting procedure

Experimental results were fitted to extrapolate coefficients of the visco-hyperelastic model. For this purpose an excel file like the one showed in figure 2.4.2 was created:

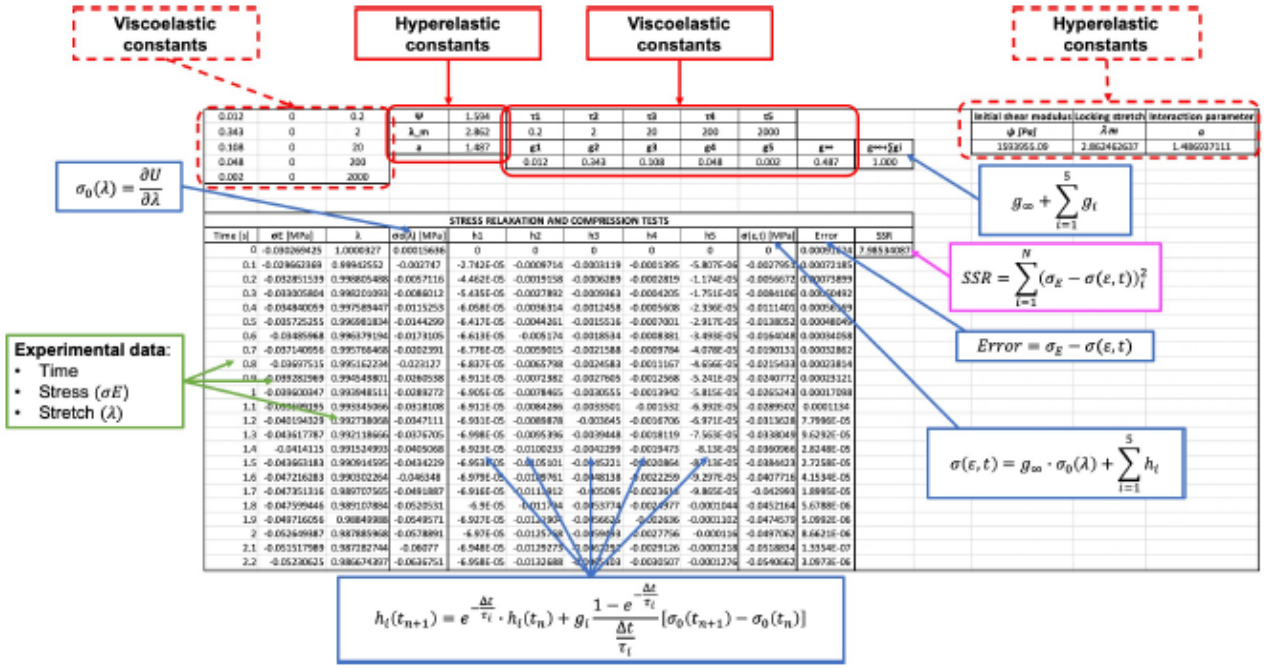

Fig. 2.4-2 Excel file used for fitting [19]

Firstly experimental curves were sampled in a specific way in order to have a reasonable number of points representing both stress relaxation and compression tests. In particular a time sampling was chosen over a stress one. Details of this sampling are summarized in table 2.2. Then data were introduced in file and the Excel solver was run to minimize the sum of the square difference between the

stresses calculated by the model and the ones measured experimentally; the variable cells were, of course, the ones representing the hyperelastic coefficients and the Prony series dimensionless moduli g_i while the τ_i values were fixed at 0.3,3,30 and 300 seconds; values selected to well describe the range of times of these tests. Finally some constraint had to be added, in particular the sum of g_i values must be equal to one and all g_i coefficients must be positive.

Test	$\dot{\varepsilon}$ [s^{-1}]	λ_{final}	Number of tests	Δt [s]
Compression	0.006	0.60	3	0.1
Compression	0.06	0.60	3	0.01
Compression	0.6	0.60	3	0.001
stress relaxation	0.06	0.90	3	0.1
stress relaxation	0.06	0.70	3	0.1

Table 2.2 Sampling of experimental curves [19]

The procedure was repeated for all four materials and for four different hyper elastic model: Mooney-Rivlin, Ogden (*N=1* and *N=2*), Van-der-Waals and Arruda-Boyce to find the best fitting one, these models are better described in the following chapter. The results are shown below (table 2.3):

Ogden	μ_1 [MPa]	α_1	μ_2 [MPa]	α_2	g_1	g_2	g_3	g_4
Material B	14.59	2.75	-11.58	0.74	0.03	0.21	0.16	0.07
Material EI	3.33	2.62	-	-	0.20	0.19	0.10	0.06
Material LG	3.99	7.42	-1.22	-4.37	0.08	0.30	0.07	0.05
Van der Waals	ψ [MPa]	λ_m	a		g_1	g_2	g_3	g_4
Material CF	1.60	2.86	1.49		0.03	0.38	0.05	0.07

Table 2.3Results of fitting procedure for all materials [19]

The best fitting was given by Ogden model in all cases except for material CF which was better represented by Van der Waals model.

2.4.3 Implementation in the artificial athlete

Finally this new model was used for the simulation of the artificial athlete test. To do so compression curves at 60 s^{-1} were extrapolated from the experimental one and were then used for a new fitting of materials parameters. This time the Prony coefficients τ_i were changed to consider lower values of time which are more suitable for an impact test. Final results showed a better agreement with experimental Force-time curves than the hyperelastic model tested previously, proving that the introduction of the viscoelastic behavior of the material improved the accuracy of the model.

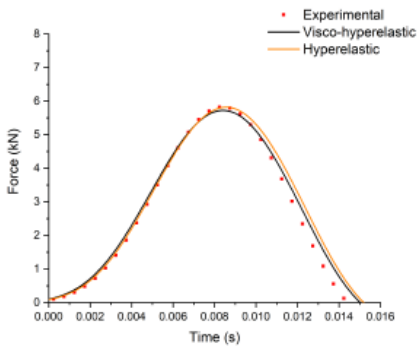

Fig. 2.4-3 Comparison between Visco-hyperelastic and hyperelastic model predictions with experimental data for LG material.

2.4.4 Friction problem

In the previous work by F.Ramusino [19] the compression and stress relaxation tests appeared to be greatly influenced by friction in terms of the resulting stress-stretch behavior. For this purpose different configurations were tested; in fact circular samples had been preferred over rectangular ones which show a greater sensitivity to the presence of friction and in addition a polytetrafluoroethylene (PTFE) film was put between the sample and the dynamometer plates. However it was observed that this procedures were not enough to eliminate the influence of friction, therefore the obtained curves on which materials constant had been calibrated were not representing a pure uniaxial compression of the specimen affecting in this way the extrapolation of the right material coefficients. As shown in figure 2.4.4 the presence of friction shifts curves toward higher compression stresses increasing the apparent stiffness of the material.

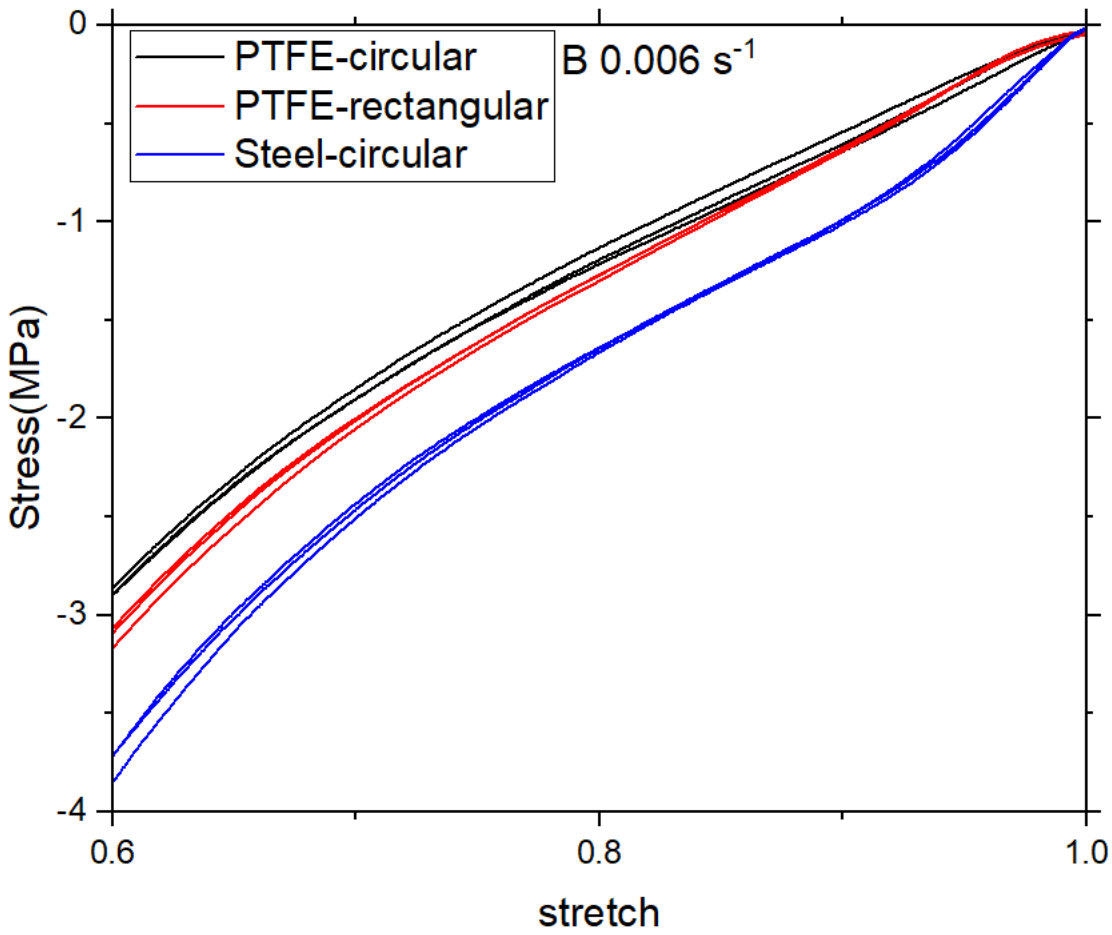

Fig. 2.4-4 Compression stress-stretch curves for material B at 0.006 s^{-1} for different frictional surfaces (steel or PTFE), geometry and shape factor of samples (rectangular 30X30X5 mm or circular Φ18X4.7 mm). Difference in the curves suggests that there is an influence of friction.

2.5 Aim of the work

The aim of the present work is to extrapolate the real material coefficients eliminating the influence of friction. To reach our purpose we used both experimental and numerical means. In particular real friction coefficients of these materials were experimentally measured and used in numerical simulations to understand how the stiffness is affected by friction and the state of stress to which the sample is actually subjected.

3. THEORETICAL BACKGROUND

3.1 Characteristics of elastomeric materials

Rubbers are polymeric materials which can undergo large amounts of elastic strain under the action of low stresses. Typical values of elastic moduli for rubbers are in the order of a few MPa. Furthermore almost all elastomers are amorphous, high molecular weight and slightly cross-linked polymers which usually have flexible chains due to their low glass transition temperatures (much lower than room temperature). Crosslinking in elastomers is usually achieved by vulcanization where the double C-C bonds of the unsaturated chain of the polymer are exploited to form covalent bonds between chains. The process is irreversible and is usually carried out in the mold through the use of vulcanization agents like sulfur or peroxides. Crosslinking can be also physical as it happens in thermoplastic elastomers like styrene-butadiene copolymers SBC where the links between Butadiene chains is achieved through polystyrene glassy domains. Industrial elastomers are never homogeneous materials because they are strongly reinforced mechanically by the use of inert fillers. Most common fillers are carbon black and silica. The reinforcing effect of the filler is depending on different factors like: size of the filler particles, the formation of aggregates and surfaces interaction (chemical and physical). The introduction of fillers greatly affects the mechanical behavior. It is noticed that a good reinforcement can provoke an increase in both stiffness and elongation at break. Also, a softening behavior during load-unload cycles is frequently observed and it is known as Mullins effect.

3.1.1 Rubber elasticity

Rubbery materials show an entropic elasticity; in fact deformation of this materials decreases Entropy as the molecular chains of the rubber go from a disordered random coil state to a more ordered stretched chain configuration. So the materials, once the load is released, restore entropy by elastically recovering the deformation. As shown in figure 3.1.1, crosslinking of the polymer prevent the recovery of entropy

by viscous flow and thermal motions allowing, in this way, a complete elastic recovery once the deforming stress is removed.

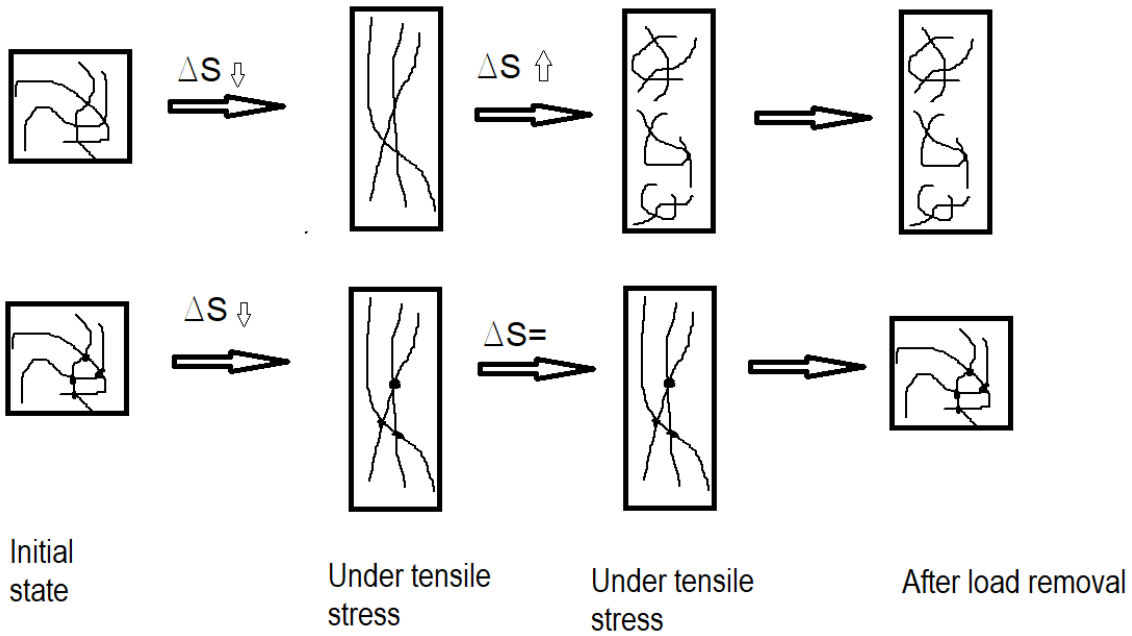

Fig. 3.1-1 Role of crosslinking and entropy in rubber elasticity. In the upper part chains without crosslinking are subjected to a tensile stress. In the lower part the role of crosslinking (black dots) is shown.

3.1.2 Molecular theory

Through the use of thermodynamics it is possible to derive a constitutive model for rubber elasticity. When a specimen is subjected to an external force it reacts with a retraction force which is ideally due to an entropic contribution [21]:

$$f = -T\left(\frac{dS}{dL}\right)_{V,T} \qquad 3.1$$

Assuming now to model the material as a network made of cross-linked sub chains, where sub chains length agree with a Gaussian distribution probability and assuming constant volume deformation we can calculate the change in entropy for every sub chain due to deformation thanks to the Boltzmann equation (3.2):

$$S = K_B \ln(\Omega) \qquad 3.2$$

Where K_B is the Boltzmann's constant and W the number of different conformations of the system. We can then sum up all contributions to obtain the total change in entropy and, consequently, the reaction of a rubber specimen in terms of stress for a uniaxial extension [21].

$$\sigma = G(\lambda - \frac{1}{\lambda^2}) \qquad 3.3$$

Where l is the stretch ratio defined in equation 3.4:

$$\lambda = \frac{L}{L_0} \qquad 3.4$$

With L and L_0 respectively the current and initial length of the specimen.

G is instead the modulus defined as:

$$G = \frac{\upsilon K_B T}{V} = N K_B T \qquad 3.5$$

where υ represents the overall number of chains, V is the volume of the specimen and N is the number of chains per unit volume. This is known as the Khun molecular model and it is able to predict mechanical behavior from molecular considerations. Some important assumptions are made in this model though, in fact the model doesn't take into account entanglements and dangling bonds, moreover more accurate models can be found by considering non Gaussian distributions.

3.2 Rubber Hyperelasticity

Hyperelastic material constitutive equation are based on the assumption of elastic energy conservation. Hyperelastic models can be either phenomenological or based on molecular theories and usually include different numbers of material parameters that can have various physical meaning. In few words they are elastic materials for which the work is independent on the load path. The elastic energy can be then

defined by a potential Ψ(C) which is function of the invariants (I_1, I_2 and I_3) of the right Cauchy deformation tensor $\boldsymbol{C} = F^T * F$ (where F is the deformation gradient) and ,as a consequences, of the strain tensor $\boldsymbol{E}$ [22].

$$w(\mathbf{E}) = \Psi(2\mathbf{E} + \mathbf{I}) \qquad 3.6$$

Potentials are usually divided in two parts: the deviatoric one and the volumetric one

$$\Psi(I_1, I_2, I_3) = \Psi_{dev}(I_1, I_2) + \Psi_{vol}(J) \qquad 3.7$$

Where J is the determinant of F. For nearly incompressible material the volumetric part is usually negligible. The stress tensor is found by derivation of the potential with $\boldsymbol{C}$; it becomes than:

$$\mathbf{S} = 2\frac{\mathrm{d}\Psi(\mathbf{C})}{\mathrm{d}\mathbf{C}} \qquad 3.8$$

And for the Cauchy stress tensor:

$$\boldsymbol{\tau} = 2\left(\frac{\mathrm{d}\Psi}{\mathrm{d}\mathbf{I_1}} + I_1\frac{\mathrm{d}\Psi}{\mathrm{d}\mathbf{I_2}}\right)\mathbf{B} - 2\frac{\mathrm{d}\Psi}{\mathrm{d}\mathbf{I_2}}\mathbf{B^2} + 2I_3\frac{\mathrm{d}\Psi}{\mathrm{d}\mathbf{I_3}}\mathbf{I} \qquad 3.9$$

Where $\boldsymbol{B}$ is the left Cauchy deformation tensor $\boldsymbol{B} = F * F^T$. Here some of the most common hyperelastic potentials will be presented. The focus will be on incompressible materials since the volumetric part is typically neglected in rubber materials.

3.2.1 Polynomial

The simplest form of strain energy potential is the polynomial one and it is usually defined as [23], [24]:

$$\Psi = \sum_i \sum_j C_{ij} * (I_1 - 3)^i (I_2 - 3)^j \qquad 3.10$$

The potential is depending on the invariants of the right Cauchy tensor C and it is the general form of simpler potentials presented below.

3.2.2 Mooney-Rivlin

In the Mooney-Rivlin constitutive model for incompressible materials the potential is defined as [23], [24]:

$$\Psi = C_{10}(I_1 - 3) + C_{01}(I_2 - 3) \quad 3.11$$

It is a bilinear form in terms of first and second invariants.

Uniaxial problem

For the uniaxial problem the deformation gradient is necessarily given by equation 3.12:

F =

$$\begin{pmatrix} \lambda & 0 & 0 \\ 0 & \frac{1}{\sqrt{\lambda}} & 0 \\ 0 & 0 & \frac{1}{\sqrt{\lambda}} \end{pmatrix} \quad 3.12$$

That is because conservation of volume imposes that $\lambda_1\lambda_2\lambda_3 = 1$ and because of the symmetry of the problem $\lambda_2 = \lambda_3$.As a consequence being $\sigma_2 = \sigma_3 = 0$ we can find the uniaxial true stress:

Cauchy =

$$\begin{pmatrix} \frac{2\,(\lambda^3 - 1)\,(c_{01} + c_{10}\,\lambda)}{\lambda^2} & 0 & 0 \\ 0 & 0 & 0 \\ 0 & 0 & 0 \end{pmatrix} \quad 3.13$$

By using $P = F^T J F^{-1} \tau F^{-T}$ we can find the Piola stress tensor which gives us the nominal stress of the problem.

P =

$$\begin{pmatrix} \frac{2\,(\lambda^3-1)\,(c_{01}+c_{10}\,\lambda)}{\lambda^3} & 0 & 0 \\ 0 & 0 & 0 \\ 0 & 0 & 0 \end{pmatrix} \qquad 3.14$$

Simple shear

In the case of a simple shear problem the deformation gradient F can be represented by equation 3.15:

F =

$$\begin{pmatrix} 1 & \gamma & 0 \\ 0 & 1 & 0 \\ 0 & 0 & 1 \end{pmatrix} \qquad 3.15$$

We can than compute the true stress tensor using the condition that $\sigma_3 = 0$:

Cauchy =

$$\begin{pmatrix} 2\,c_{10}\,\gamma^2 & 2\,\gamma\,(c_{01}+c_{10}) & 0 \\ 2\,\gamma\,(c_{01}+c_{10}) & -2\,c_{01}\,\gamma^2 & 0 \\ 0 & 0 & 0 \end{pmatrix} \qquad 3.16$$

As we can observe shear deformation linearly increases with shear stress and the shear modulus is than represented by the sum:

$$G = 2 * (C_{01} + C_{10}) \qquad 3.17$$

Using then the isotropic approximation and the volume conservation ($\nu = 0.5$, where υ is the Poisson ratio) we can estimate the Young's modulus that should describe the behavior of the element for small deformations.

$$E = 6 * (C_{01} + C_{10}) \qquad 3.18$$

Note that for shear problems the nominal stress should equal the true stress as we have no change in the stressed area.

3.2.3 Neo-Hookean

The Neo-Hookean model is a single parameter model:

$$\Psi = C_{10}(I_1 - 3) \quad 3.19$$

Using the same consideration made above we notice that Neo-Hookean model is a particular case of Mooney-Rivlin model where C_{01}=0. And so for the nominal uniaxial stress state we get equation 3.20:

$$P = \begin{pmatrix} \frac{2\,c_{10}\,(\lambda^3 - 1)}{\lambda^2} & 0 & 0 \\ 0 & 0 & 0 \\ 0 & 0 & 0 \end{pmatrix} \quad 3.20$$

For the simple shear problem the results are equal to the Mooney-Rivlin model where C_{01}=0.

$$\text{Cauchy} = \begin{pmatrix} 2\,c_{10}\,\gamma^2 & 2\,c_{10}\,\gamma & 0 \\ 2\,c_{10}\,\gamma & 0 & 0 \\ 0 & 0 & 0 \end{pmatrix} \quad 3.21$$

As a consequence:

$$E = 6 * (C_{01}) \quad 3.22$$

The Neo-hookean model can be derived from the molecular theory of rubber elasticity using Khun model assumptions [23].

3.2.4 Ogden

The Ogden potential is instead defined in terms of the principal stretches rather than $\boldsymbol{C}$ invariants. Principal stretches are defined as the eigen values of the stretch tensor V, which is defined as $V = (F * F^T)^{0.5}$ and represents the pure deformation component of the F matrix. The potential is defined in this way [24], [25]:

$$\Psi = \sum_j 2 * \frac{\mu_j}{\alpha_j^2} * (\lambda_1^{\alpha_i} + \lambda_2^{\alpha_i} + \lambda_3^{\alpha_i} - 3) \quad 3.23$$

The principal stresses can then be computed with this relation [25]:

$$\sigma_i = \sum_j 2 * \frac{\mu_j}{\alpha_j} * \lambda_i^{\alpha_i} \quad 3.24$$

In the case of a uniaxial stress problem and considering volume conservation the principal stretches are exactly the components of the F matrix shown in equation 3.12.Therefore using equation 3.24 to find the principal stresses σ_1, σ_2 and σ_3; putting then the condition of uniaxial stress $\sigma_2 = \sigma_3 = 0$ we can find the solution to the uniaxial problem for Cauchy stress by eliminating the contribution of hydrostatic pressure $\sigma_1 - \sigma_2 = \sigma_1 - \sigma_3 = \sigma_1$ to finally get the solution:

$$\sigma = \sum_j 2 * \frac{\mu_j}{\alpha_j} * (\lambda^{\alpha_j} - \lambda^{-\frac{1}{2}\alpha_i}) \quad 3.25$$

The resulting nominal stress is instead:

$$\sigma = \sum_j 2 * \frac{\mu_j}{\alpha_j} * (\lambda^{\alpha_j - 1} - \lambda^{-\frac{1}{2}\alpha_i - 1}) \quad 3.26$$

For the simple shear problem instead we have to first find the principal stretches by finding the eigen values of matrix V. To do this the reference system is rotated by an angle equal to:

$$\tan(2\theta) = 2\gamma^{-1} \quad 3.27$$

Then the principal stresses are found with equation 3.24 and finally the shear stress can be found with equation 3.28:

$$\sigma_{xy} = \frac{1}{2}(\sigma_1 - \sigma_2)\sin(2\theta) \qquad 3.28$$

We notice that for low values of g the angle is 45° and thus correspond exactly to a state of maximum pure shear without any normal stress. It can be finally shown that the equivalent initial shear modulus is about:

$$G = \sum_i \mu_i. \qquad 3.29$$

3.2.5 Arruda-Boyce

The eight-chain model, also known as the Arruda-Boyce model , idealizes the rubber network as eight representative chains connecting the centroid of a cube to the corners [23].

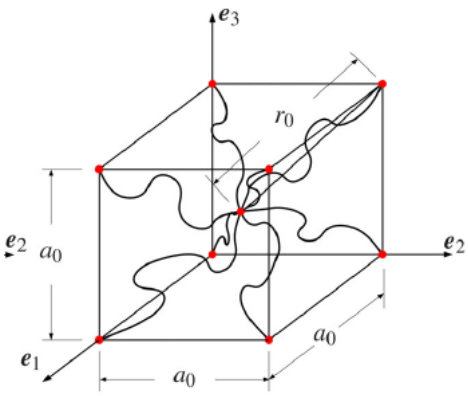

Fig. 3.2-1 Representation of eight chain model [23]

The resulting strain energy function can be expressed as [23], [24]:

$$\Psi = \mu \sum_i \left(\frac{C_i}{\lambda_m^{2i-2}}\left(I_1^i - 3^i\right)\right) \qquad 3.30$$

Where $C_1 = \frac{1}{2}$, $C_2 = \frac{1}{20}$, $C_3 = \frac{11}{1050}$, $C_4 = \frac{19}{7000}$ and $C_5 = \frac{519}{673750}$; l_m and m are material parameters. In particular, the locking stretch, λ_m, and μ can be correlated to the initial shear modulus G_0 as follows:

$$G_0 = \mu(1 + \frac{3}{5*\lambda_m^2} + \frac{99}{175*\lambda_m^4} + \frac{513}{875*\lambda_m^6} + \frac{42039}{67375*\lambda_m^8}) \qquad 3.31$$

3.2.6 Van-der-Waals

The potential used by Kilian in the so called Van der Waals model is this [23], [24]:

$$\Psi = \mu(-(\lambda_m^2 - 3)[\ln(1-\eta) + \eta - \frac{2}{3}a\left(\frac{I'-3}{2}\right)^{\frac{3}{2}}] \qquad 3.32$$

Where:

$$I' = (1-\beta)I_1 + \beta I_2 \quad 3.33$$

$$\eta = \left(\frac{I'-3}{\lambda_m - 3}\right)^{\frac{1}{2}} \quad 3.34$$

The name Van der Waals draws on the analogy in the thermodynamic interpretation of the equations of state for rubber and gas. While the Neo-Hookean model can be compared with an ideal gas in that it starts out from a Gaussian network with no mutual interaction between the quasi-particles, the Van der Waals strain energy potential is analogous to the equations of state of a real gas. The parameter a represents in fact the Van der Waals interaction term and it decreases as the crosslink density increases; λ_m governs the limiting chain extensibility and μ is a modulus term which correspond to the initial shear modulus [23].

3.3 Viscoelasticity

All polymeric materials exhibit a viscoelastic behavior. This means that the response to a mechanical loading on the material is time and history dependent. This dependence is given by the viscous dissipations in the material during loading, in fact the material is not only behaving like a purely elastic solid but also as a sort of viscous liquid. In order to describe time-dependency the modulus of the material (or its compliance) is defined as a function of time *E=E(t)* (or *D=D(t)*) as shown in figure 3.3.1. This function is often described by either a power law or an exponential that assumes these forms respectively:

$$E(t) = E_0 , t < t_0 ; E(t) = E * t^{-n} , t_0 < t < t_{inf} ; E(t) = E_\infty , t > t_\infty \quad 3.35$$

$$E(t) = E_0 - E * e^{-\frac{t}{\tau}} \quad 3.36$$

These functions feature an instantaneous modulus *(E(0))* an asymptotic modulus *(E(∞))* and a characteristic time.

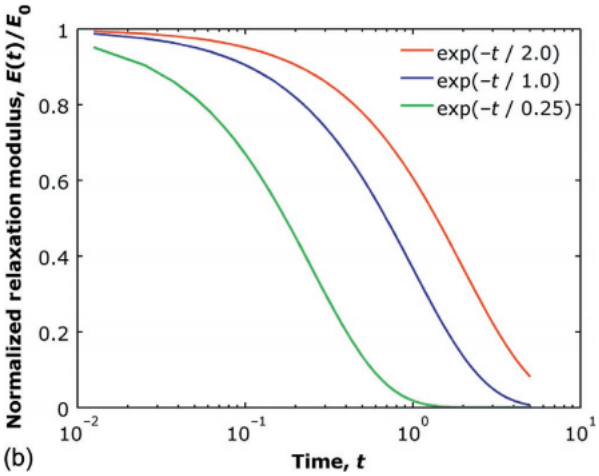

Fig. 3.3-1 Example of plot of Modulus versus time for a viscoelastic material. [22]

In the *log(E)* versus *log(t)* plot the asymptotic values at short and long times represent respectively E_0 and E_∞ while the characteristic time is the abscissa value at which we see the change in the second derivative sign. History dependence also plays a fundamental role in the description of the mechanical output. To describe complex

load history we usually take advantage of the Boltzmann superposition principle whose final form is:

$$\sigma(t) = \int_0^t E(t-s) * \frac{d\varepsilon}{ds}\, ds \qquad 3.37$$

The principle decomposes the complex loading history in simple steps whose contribution is finally summed up to the desired time *t*. Typical tests used to describe viscoelastic characteristics of the polymer are stress-relaxation and creep. In the first one the strain is fixed and the decreasing of stress is measured; on the contrary in creep test the stress is fixed and the strain increases in time. One thing that must be noticed is that the compliance of a creep tests is not the inverse of the relaxation modulus. To describe the viscoelastic behavior simple mechanical models are used. These models, also known as analogue models, consist of a combination, in series or in parallel, of springs, which accounts for the elastic behavior, and dampers, which instead account for the viscous behavior. The simplest examples are the Kelvin and Maxwell (figure 3.3.3) models which uses just one spring and one dashpot, respectively in parallel and in series. More complex models, like Zener's one, are made of a greater number of elements [22].

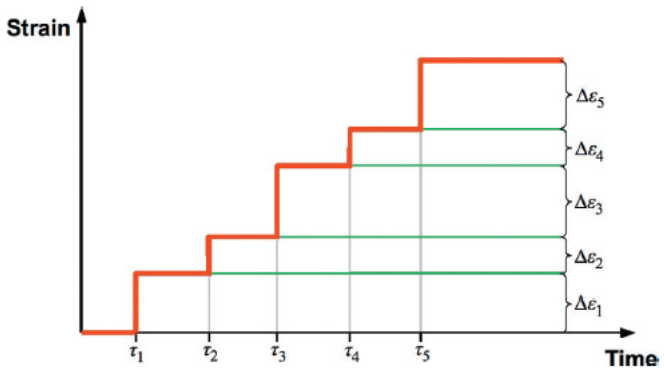

Fig. 3.3-2 Decomposition of the strain history in simple steps. [22]

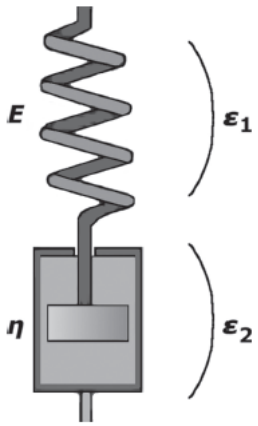

Fig. 3.3-3 Maxwell model [22]

3.4 Finite element method

The finite element method (FEM) is a numerical technique for solving problems which are described by partial differential equations or can be formulated as functional minimization. One of the greatest advantage of FEM is the capability to provide approximated solutions in problems defined in a complex or variable domain this method can be used to solve problems of many types: mechanics, fluid dynamics, thermo-mechanics, electromagnetics and geotechnics [26][27]. The basic principle of the FEM is the domain discretization. It consists in setting a finite number of characteristic points (nodes) in order to obtain a separation of the solid body into a finite number of elements, with proper connectivity and without gap or overlapping. The elements all together form a mesh, whose density strongly affects the accuracy of the analysis. The FEM finds the solution to the problem following six key steps:

1. Idealization: the physical system is represented with a mathematical model. It can be done reducing the dimensions, idealizing the support conditions and suppressing details that complicate the problem but are inessential for solving it.
2. Discretization: the continuous domain of the problem is discretized into a collection of simple parts (elements).
3. Choice of the type of element.
4. Assembly: The element equations for each element in the FEM mesh are assembled into a set of global equations that model the properties of the entire system.

5. Application of boundary conditions: they are forces, or other kind of stimuli, and restraints; imposing boundary conditions modifies the global equations.
6. Solving for primary unknowns: the modified global equations are solved for the primary unknowns at the nodes.
7. Calculation of the Derived Variables: by using the nodal values of the primary variables [26] [27].

In the finite element method the displacement field is discretized in this way:

$$u = N_N u^N \qquad 3.38$$

Where N is the shape function and u^N is the nodal displacement. The virtual velocity δv and the virtual rate of deformation δD can be than be discretized as:

$$\delta \mathrm{v} = \mathrm{N_N} \delta \mathrm{v^N} \quad and \quad \delta \mathrm{D} = \mathrm{B_N} \delta \mathrm{v^N} \qquad 3.39$$

The equilibrium problem is finally discretized as:

$$\delta \mathrm{v^N} \int B_N^T : \sigma \mathrm{dV_0} = \delta \mathrm{v^N} [\int N_N^T * \mathrm{b\ dV} + \int N_N^T * f\ \mathrm{dS}] \qquad 3.40$$

This non-linear problem can be solved iteratively, for instance using the Newton-Raphson method; in fact ABAQUS solves the problem considering the incremental form [26].

3.4.1 Time integration

The above equation 3.40 can be rewritten as [19]:

$$M\ddot{u} + C\dot{u} + Ku = f_{ext} - f_{int} \qquad 3.41$$

M is the mass matrix and it is responsible for inertial effect, C is the damping matrix and it is multiplied by the first time derivative of displacement, K is the stiffness matrix dependent on geometry and constitutive equations of the model, f_{ext} and f_{int} are the forces, external and internal to the structure, acting on the node. When neither damping nor inertial effect are relevant for the problem (as it happens in static-general steps) this equation can be simplified as:

$$f = Ku \qquad 3.42$$

The overall analysis time is subdivided in a sequence of smaller steps Δt, corresponding to increments in the applied force Δf or displacement Δu. At any time increment the stiffness matrix K must be updated. Such incremental approach can be carried out with two different algorithms: implicit (traditional) or explicit, respectively implemented in Abaqus/Standard and Abaqus/Explicit [28] [24].

Explicit integration

Abaqus/Explicit is based on the implementation of an explicit integration rule along with the use of diagonal element mass matrices [24]

$$u^{i+1} = u^{i} + \Delta t \dot{u}$$
$$u^{i+\frac{1}{2}} = u^{i-\frac{1}{2}} + \frac{1}{2}(\Delta t^{i+1} + \Delta t^{i})\ddot{u}$$
$$\ddot{u}^{i} = M_l^{-1}(f_{ext}^{i} - f_{int}^{i}) \qquad 3.43$$

Where $\dot{u}$ is the velocity, $\ddot{u}$ the acceleration, $i, i-\frac{1}{2}$ and $i+\frac{1}{2}$ refer to the increment number and mid-increment numbers respectively and M_l is the so-called mass lumped matrix which is a diagonal mass matrix calculated by ignoring the deformation of the related finite element. This approach do not enforce the equilibrium between the internal and the external forces acting on each node of the model so that the analysis of each time increment is considerably less expensive than in the implicit method. On the other hand, the drawback of the explicit method is the conditional stability. The stability limit for an explicit operator is that the maximum time increment must be less than a critical value of the smallest transition times for a dilatational wave to cross any element in the mesh and this should, in principle, increase the analysis duration. In conclusion, explicit method is well-suited to deal with dynamic systems as well as contact or material complexities that typically require an excessive number of iterations to achieve convergence in Abaqus/Standard.

Implicit integration

Abaqus/Standard uses the Newton-Raphson method to obtain solutions for nonlinear problems. Actually, Abaqus/Standard breaks the simulation into a number of load increments and finds the approximate equilibrium configuration at the end of each load increment. Abaqus/Standard uses the structure's initial stiffness, K_0, which is based on its initial configuration, u_0, and a small load increment Δf_{ext} to calculate a displacement variation, Δu_1, for the structure. Then, the structure configuration is assessed at the current configuration $u_1 = u_0 + \Delta u_1$. In this configuration the software generates a new stiffness matrix K_1 and evaluates the residual force R_1 [24]:

$$R_1 = f_{ext} - f_{int,1} \qquad 3.44$$

If R_1 is less than a user specified tolerance at every point than the solution is accepted otherwise it performs another iteration. For each iteration in a nonlinear analysis Abaqus/Standard forms the model's stiffness matrix and solves a system of equations. This means that each iteration is equivalent, in computational cost, to conducting a complete linear analysis. Due its computational cost and risk of instabilities that makes it hard to find a force equilibrium implicit integration is usually employed to solve only smooth nonlinear problems. Finally, once the analysis of an increment is completed, on the basis of the success rate of Newton-Raphson iterations, Abaqus/Standard automatically adjusts the size of the subsequent Increments [24].

3.4.2 Viscoelasticity in Abaqus

In the present work all the numerical model are realized with the commercial finite element software ABAQUS and use as constitutive model the visco-hyperelastic one described above. For this reason in this paragraph it is briefly introduced how viscoelasticity is implemented in ABAQUS. The program assumes that the viscoelastic function is a Prony series like the one in equation 3.45:

$$g(t) = 1 - \sum g_i (1 - e^{-\frac{t}{\tau_i}}) \qquad 3.45$$

The corresponding stress can be calculated using equation 3.37 and integration by parts:

$$\tau(t) = \tau_0 + \int_0^t \dot{g}\,(s)\tau_0(t-s)ds \qquad 3.46$$

The viscoelastic behavior can be used in ABAQUS for both linear and non-linear elasticity [24]. To describe the viscoelasticity it is necessary to input one of these set of data: stress relaxation test or creep test data, frequency dependent cyclic test data or Prony series coefficients. In our case the coefficients for the viscoelastic function had been already calculated by [19] through the fitting procedure described above.

3.5 Contact in Abaqus

Another fundamental aspect for all the models realized in this work is contact. In this subsection the main types of contact present in ABAQUS are described for a better understanding of the models mentioned later. Contact definition is related to how instances interact with each other. To define contact it is always necessary to choose a master surface and a slave surface. The former should belong to the stiffer body and should have a coarser mesh than the other one. Contact is than defined by its normal and tangential behavior [24].

3.5.1 Normal contact behavior

Hard contact is a type of normal contact and it allows the pressure between two parts to assume any value as soon as they come in contact with each other (according to the mechanics of these bodies), while the interaction vanishes if the bodies are not in contact.

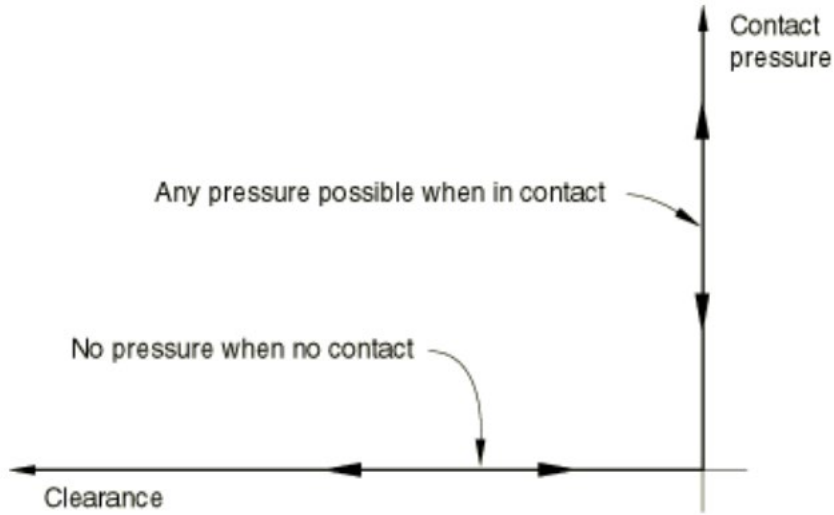

Fig. 3.5-1 Schematic representation of hard contact behavior [24]

Sometimes hard contact creates convergence problems and in these cases, other, more sophisticated, contact definitions implemented in ABAQUS may be useful such the penalty interaction which is probably the most common one. It can be considered as a sort of loosening of the hard contact conditions, in fact no interaction is simulated as long as the distance between two components is larger than zero, whereas, as the parts get in contact, the pressure rises linearly with their interpenetrating length, up to a predefined maximum tolerance value. Such linear relation depends on the stiffness matrix value *K*, which is automatically defined by the software, and it is enforced by means of Lagrangian multipliers. The exponential normal contact in a similar way allows the pressure to increase exponentially when the bodies get closer, to define it the clearance at which pressure is zero and the pressure at zero clearance must be input.

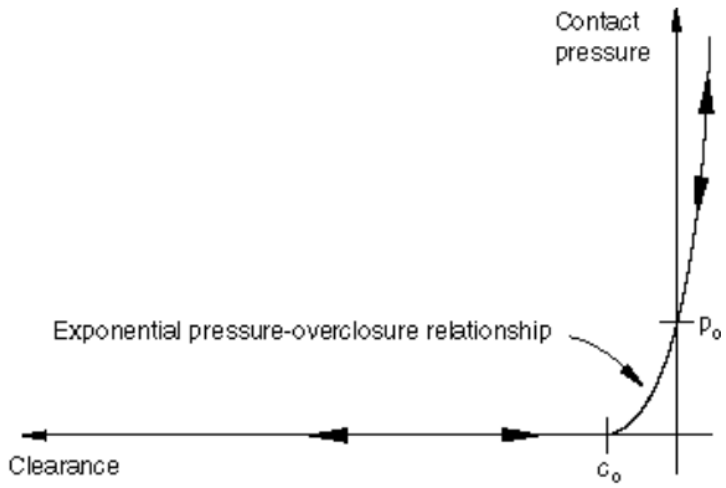

Fig. 3.5-2 Schematic representation of exponential contact behavior [24]

3.5.2 Tangential contact behavior

The simplest tangential contact behavior in ABAQUS is the frictionless one where no force is applied when the two bodies are sliding against one another. There are many ways to introduce friction in the analysis: penalty, exponential, rough and La Grangian. By default ABAQUS uses the basic Coulomb friction model according to which the surfaces can carry a shear stress up to a limit given by the Coulomb friction law

$$C_{shear} \leq \mu * C_{pressure} \qquad 3.47$$

Where $C_{pressure}$ is the contact normal pressure, μ the friction coefficient and C_{shear} is the contact shear that in the case of a 3D model is computed using an average of the two orthogonal component:

$$\tau_{eq} = \sqrt{(\tau 1^2 + \tau 2^2)} \qquad 3.48$$

The μ value can be input as a series of data dependent on slip velocity and $C_{pressure}$. When C_{shear} reaches the maximum value set by equation 3.47 slipping between the two surfaces occurs. When instead this value is lower a sticking slip tolerance can be set using a linear relation with a defined stiffness as shown in figure 3.5.3 [24]. The lagrangian multiplier friction similarly prevent relative motion between the surfaces until a critical contact shear value is reached, anyway this formulation increases the computational cost of the analysis and can even prevent convergence [24].

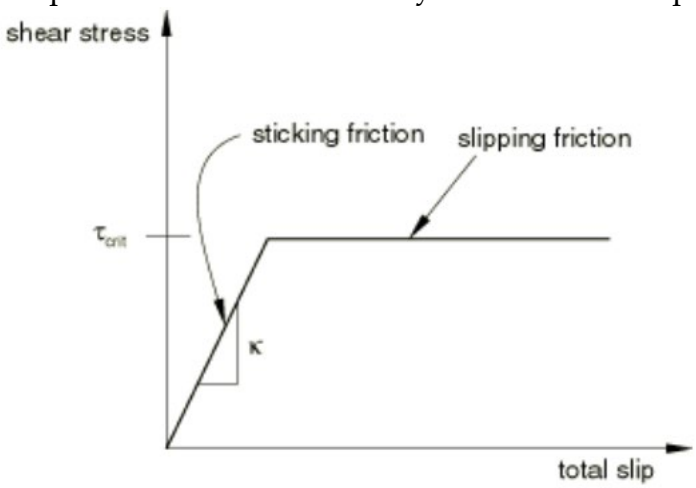

Fig. 3.5-3 Contact shear versus slip graph. K is the elastic slip stiffness [24]

In the exponential friction instead also a static friction coefficient is considered. When slipping starts the μ value is exponentially decreased to its dynamic (Kinetic) value.

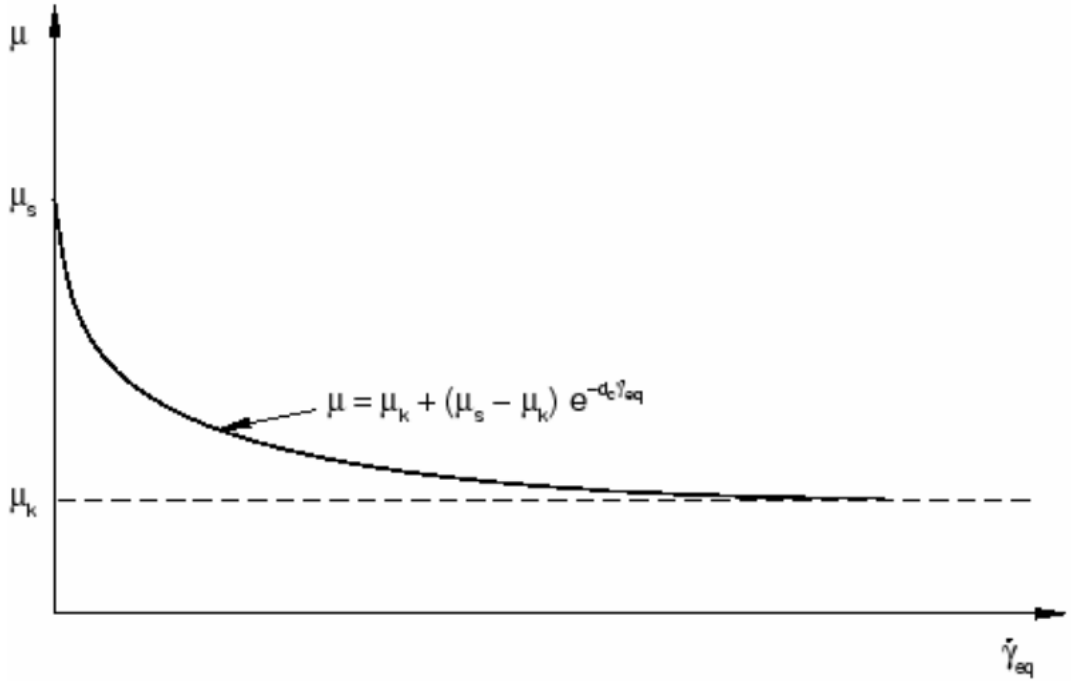

Fig. 3.5-4 Exponential friction behavior [24]

Here an equivalent slip rate $\dot{\gamma}_{eq}$ is calculated in a way analogous to equation 3.79 used for shear stress. Finally a rough frictional behavior is present as an option. In this case no slip will ever occur after the two surfaces has come in contact therefore allowing the shear contact stress to reach any value.

4. COMPRESSION OF RUBBER BLOCKS

In this section a theory regarding the compression of rubber blocks in bounded or frictional condition is briefly presented. In particular the focus will be on the quantitative estimation of how much the stiffness of the rubber is increased due to frictional behavior and on the stress state expected in the rubber specimen.

4.1 Theory

When a rubber block is compressed between two rigid surfaces it is usually prevented from expanding laterally by frictional or even bonded constraint; in this way during compression the rubber block appear to have a greater stiffness than its intrinsic one and this stiffness is related to the apparent modulus E_a. Furthermore interfacial stresses created during compression may affect slippage and durability of the block. Compression of bounded blocks has been widely studied as it may be useful to design bridge piers cushioning systems and rail tie-bars or it may affect stiffness, braking and wear of a tire. Many relations have been found to relate the apparent modulus of bounded axisymmetric samples to the real modulus of the material, some are listed below [29] [30] [31] [32].

$$E_a = E(1 + \frac{1}{2}\left(\frac{a}{h}\right)^2) \qquad 4.1$$

$$E_a = E(1.2 + 2s^2) \qquad 4.2$$

All these relations depend on the radius-to-thickness ratio a/h (sometimes defined as one loaded area over the total free area of the sample $S = \frac{a^2}{2ah} = \frac{a}{(2h)}$ for circular shape) of the sample and on its geometrical shape. In fact the equations slightly changes when a rectangular block in plane strain is considered [32].

$$E_a^{rect} = \frac{4}{3}E(1+s^2) \qquad 4.3$$

These relations are found assuming linear elastic incompressible materials and are valid for aspect ratios *a/h* higher than one. For example in the work by Gent et al [29] a parabolic lateral deformation of the sample, which keeps volume constant, is assumed to find equation 4.1, as shown in figure 4.1.1.

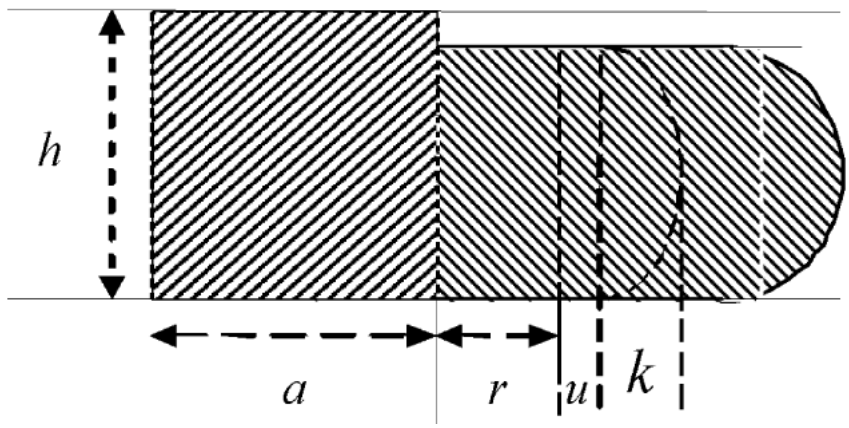

Fig. 4.1-1 Deformation of axisymmetric block. k(r) is the maximum outward displacement, r the radial coordinate and u slip displacement. [29]

k, defined as the maximum outward displacement, is found by volume conservation and, for a circular specimen, it is equal to:

$$k(r) = \frac{3er}{4} \qquad 4.4$$

Where *e* is the input vertical deformation and *r* the radial coordinate. An example of how to find *k* for the simpler case of infinitely long rectangular blocks is given by [30] and is shown in figure 4.1.2.

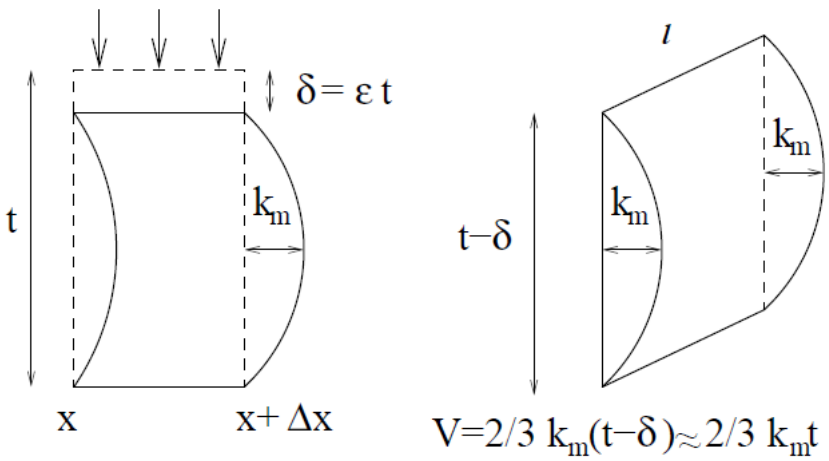

Fig. 4.1-2 Calculation of the volume of the parabolic bulge for infinitely long rectangular blocks [30]

Having *k* it is possible to compute the interfacial shear stresses:

$$\frac{t}{Ee} = \frac{r}{h} \qquad 4.5$$

And from equilibrium considerations we can extrapolate the variation of pressure *dP/dr* as shown in figure 4.1.3

$$\frac{P}{Ee} = \frac{a^2 - r^2}{h^2} \qquad 4.6$$

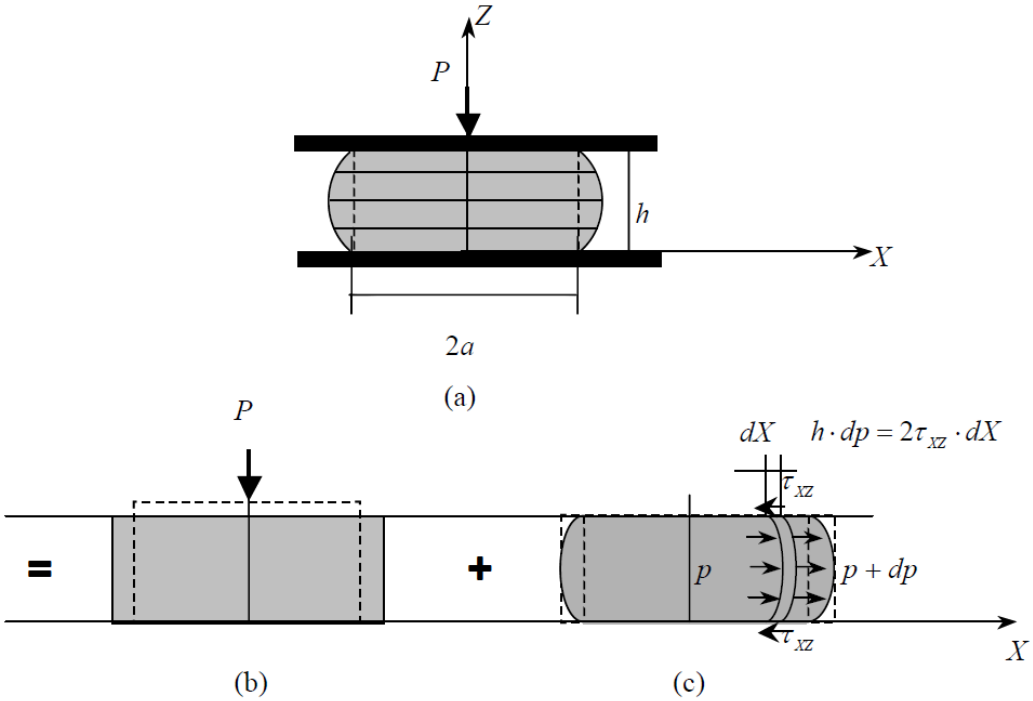

Fig. *4.1-3 Decomposition of bounded compression in frictionless compression and shear. Calculation of horizontal pressure [32]*

Finally the total vertical loading is found by summing the contribution of a frictionless compression stress *E*e* and the integral of the pressure along radial direction with boundary condition that *P=0* at the edge. In a similar way Gent et al [29] studied the problem considering frictional surfaces instead of bounding constraint. In this case the sample is divided in a slip area close to the edge where shear stresses at interface are equal to the contact pressure multiplied by μ and a non-slip area close to the center in which interfacial shear stress are lower than $\mu * Cpressure$ and the block results bounded. Part of the deformation in the slip region is accommodated by slipping:

$$k(r) = \frac{3(er-2u)}{4} \qquad 4.7$$

With an integration of the gradient of *P* along *r* on the two regions (slip and non-slip) and adding the contribution of frictionless compression stress *E*e* a final total force

needed for the deformation of the sample is found and it is related to the real modulus:

$$\frac{F}{\pi * a^2 Ee} = \left[\left(\frac{R_l^4 a^2}{2h^2}\right) + \left(\frac{R_l^3 a}{\mu h}\right) + \left(\frac{R_l^2}{\mu^2}\right) + \left(\frac{R_l h}{2a\mu^3}\right) - \left(\frac{h}{a\mu}\right) - \left(\frac{h^2}{2(a\mu)^2}\right)\right] \quad where\ R_l = \frac{r_l}{a} \qquad 4.8$$

Where R_l is the ratio between slip radius r_l (radius at which slip area begins) and maximum radius. Finally the ratio between the apparent modulus and bounded modulus E_{ns} for different values of COF is represented in figure 4.1.4. The bounded modulus E_{ns} is defined as the apparent modulus in bounded condition, thus it is related to the intrinsic modulus E by equation 4.1.

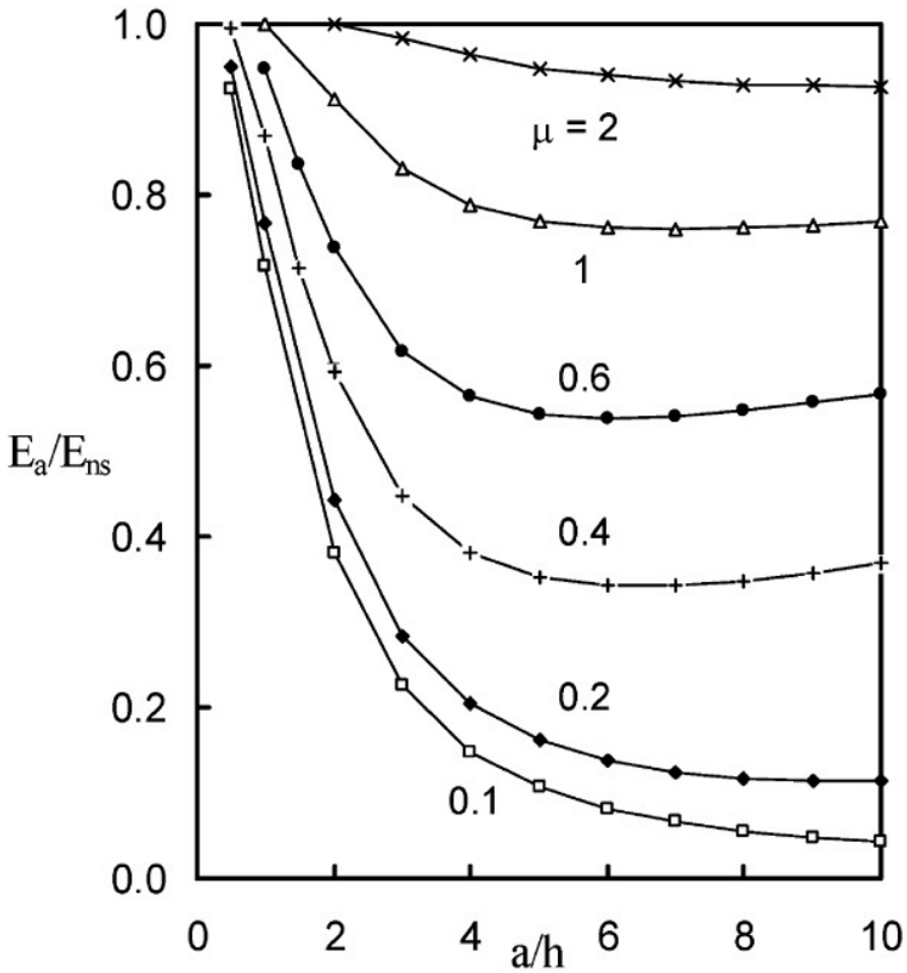

Fig. 4.1-4 Ratio of apparent modulus over bounded modulus versus radius over thickness ratio for different COFs [29]

Here it is possible to observe that as friction values increases the ratio E_a/E_{ns} tend to 1 because the sample is closer to the bounded condition. This graph can be converted to find the relation between ratio E_a/E and aspect ratio through the use of equation 4.1 which, as said before, links E_{ns} to E. The result is shown here in figure 4.1.5:

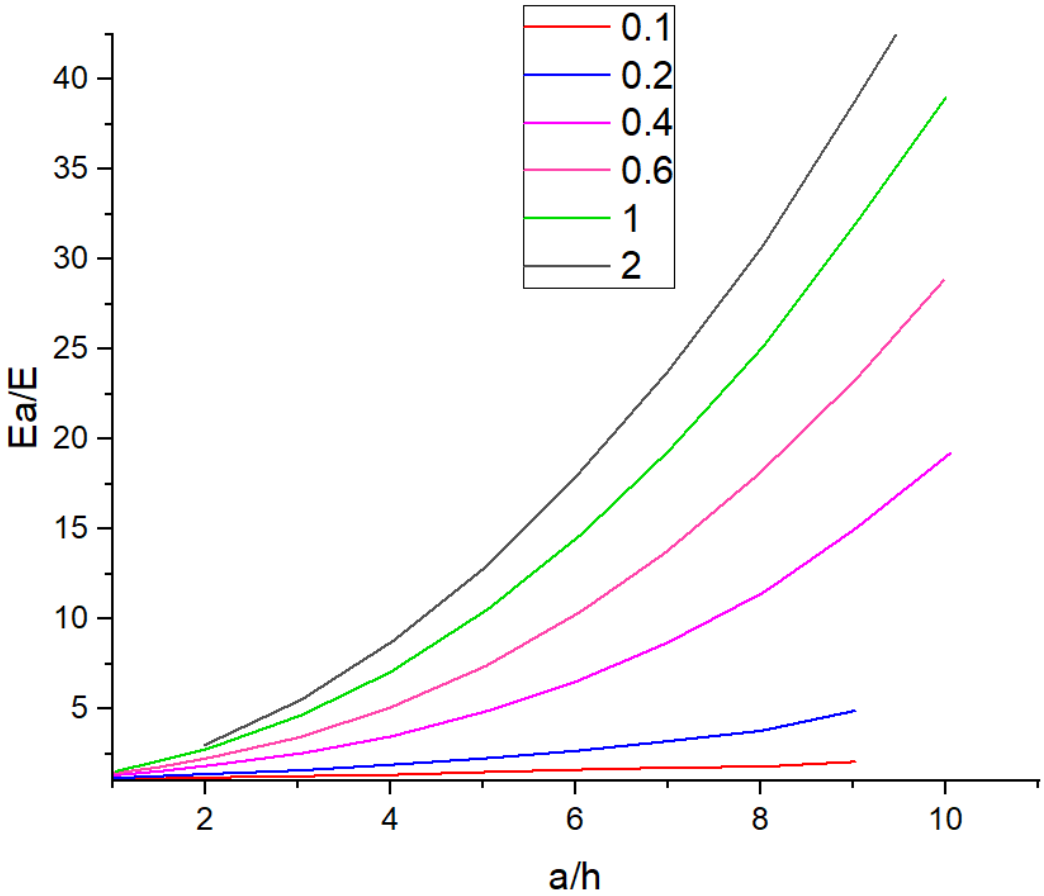

Fig. 4.1-5 Ratio of apparent modulus over real modulus versus radius thickness ratio for different COFs [29]

According to this theory when the a/h ratio is close to ten the apparent modulus can become even more than 40 times the intrinsic one; of course for such high stresses other phenomena like rubber cracking and compressibility should be taken into account.

4.2 Stress state of the block

The stress state in a block during a bounded compression is much different than that expected for an ideal compression. In fact if the surfaces of the sample and the disk are well lubricated in a way that friction is negligible shear stresses and normal stresses perpendicular to the loading direction are zero and the specimen is subjected to a pure uniaxial load. In this particular case one should expect to obtain the same compression curve in terms of stress versus stretch for any geometrical shape and aspect ratio of the sample. When friction is not negligible instead shear stresses are present at the interface between sample and disk; this stress is lower or equal to the value of the contact pressure multiplied by the friction coefficient accordingly to the Coulomb friction model (equation 3.47). The sample is therefore constrained to counterbalance friction force by deforming in a parabola-like shape that is supposed to provide the contact shear stress necessary for it to slip and expand. This shear stress varies along the height of the specimen and as a consequence for the equilibrium conditions, a gradient of horizontal pressure is created in the radial direction, in particular this pressure is higher when we get closer to the center. The horizontal pressure acts like a sort of hydrostatic pressure which works against the expansion of the specimen thus creating the need for a higher value of vertical stress to perform the compression. The magnitude of shear gradient and horizontal pressure are different when the aspect ratio or the shape of the specimen are changed, in particular when a/h is very high (greater than 6) expansion of the specimen becomes very hard and many suggest that stresses becomes high enough to make the compressibility of the material non-negligible [29].

The BS ISO 7743:2017 standard also suggests that for very low a/h ratio it is possible to neglect the effect of friction; quoting the standard itself [33] :

" In the case of a compression test piece, it is necessary to maximize the uniaxial stress component and to avoid shear and/or biaxial components. Ideally, a perfect compression test piece is a long cylinder with a small cross-section. Practically, such a test piece is not suitable for compression because of buckling. A series of tests performed on test pieces with various slenderness ratios together with finite element computations show that a uniaxial stress state can be created and preserved over a wide range of deformation when the slenderness ratio (length-to-diameter ratio) is greater than or equal to 1. If the test piece geometry is too flat, a correction factor is required to derive the compression properties from the test results.[…] The test piece geometry has little influence on the loading curve as long as the compression platens are well lubricated. However, if the test pieces are bonded, the effective stiffness increases when the slenderness ratio decreases."

5. MATERIALS AND METHODS

5.1 Materials

In this work four different materials has been considered: B, CF, EI and LG. All four materials (summarized in table 5.1) are the same described in [19] and had been produced by Mondo Spa by mixing natural and synthetic rubber (NR, SBR and EPDM) with fillers. Specimen had no macroscopic porosity and they didn't show any honeycomb pattern as it happens in usual athletic tracks. They were cut from 300 mm side plates obtained by compression molding at 165°C for about 10 minutes. Moreover they have experienced a different thermo mechanical history with respect to the corresponding tracks which are produced by continuous calendaring [19].

Material	Function	Density(g/cm^3)	Thickness (mm)	Color
B	Finishing	(1.302 ± 0.010)	4.67 ± 0.07	BLUE
LG	Base	(1.402 ± 0.020)	4.67 ± 0.04	GREY
EI	Finishing	(1.373 ± 0.0030)	4.67 ± 0.03	LIGHT BLUE
CF	Base	(1.247 ± 0.010)	4.72 ± 0.06	BLACK

Table 5.1 Description of materials investigated [19]

5.2 Experimental compression and stress relaxation tests

Since the thickness of the rubber sheets provided didn't allow the realization of samples with an acceptable aspect ratio, as suggested earlier by [33], the only way to identify constitutive parameters of the 4 materials was to perform compression tests

with well lubricated interfaces. In the previous work by [19] a first attempt was done with the use of soap as liquid lubricant along with the use of PTFE as solid lubricant. However the author mentions that with this configuration the sample was squeezed away from the machine platens making the collection of reliable data impossible. For this reason in the present work experimental compression tests and stress relaxation tests were carried out using again PTFE and soap together for the lubrication of the sample-platens interface. The test parameters are the same used by [19] and described in paragraph 2.4.1. Three velocities were used for the compression: 0.6; 0.06 and 0.006 s^{-1}, up to a nominal deformation of 40%. Stress relaxation tests followed ramp of slope 0.06 s^{-1} and maintained at a deformation of 10% or 30%. For the fastest compression tests an offset of 3 mm from the sample was suggested by [19] to avoid crosshead inertial effects. The tested specimens were circular with a nominal radius of 9 mm and a thickness of about 4.7 mm. To solve the problem described in [19] the first idea was to use a guide for the compression punch in order to confine the specimen and prevent it from being squeezed away. This set up is represented in figure 5.2.1. The guide was realized on purpose in order to avoid any interference with the punch and it is represented in figure 5.2.2.

Test	Velocity (s^{-1})	Final deformation (%)	Total Time (s)
Compression	0.006	40	66.67
Compression	0.06	40	6.667
Compression	0.6	40	0.6667
Stress relaxation	0.06 (ramp)	30	305.0
Stress relaxation	0.06 (ramp)	10	301.7

Table 5.2 Parameters for compression and stress relaxation tests.

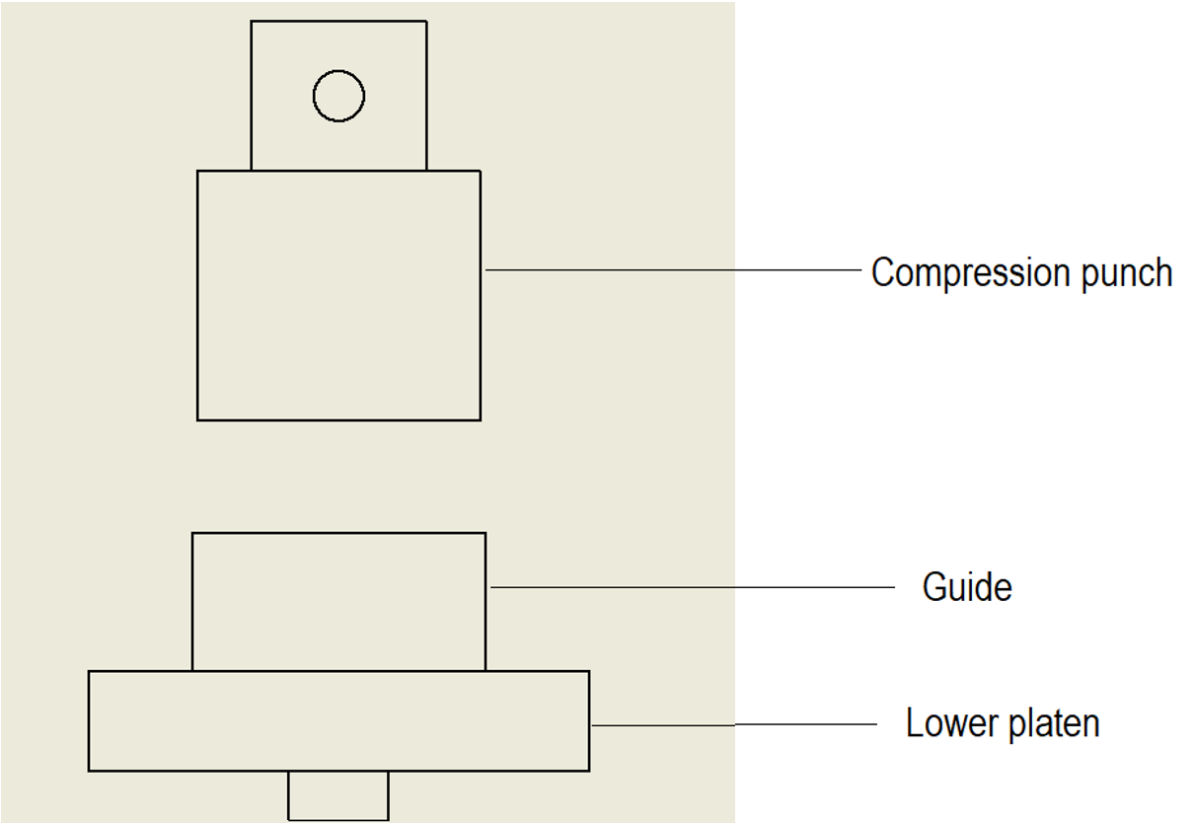

Fig. 5.2-1Experimental setup for compression tests and stress relaxation tests.

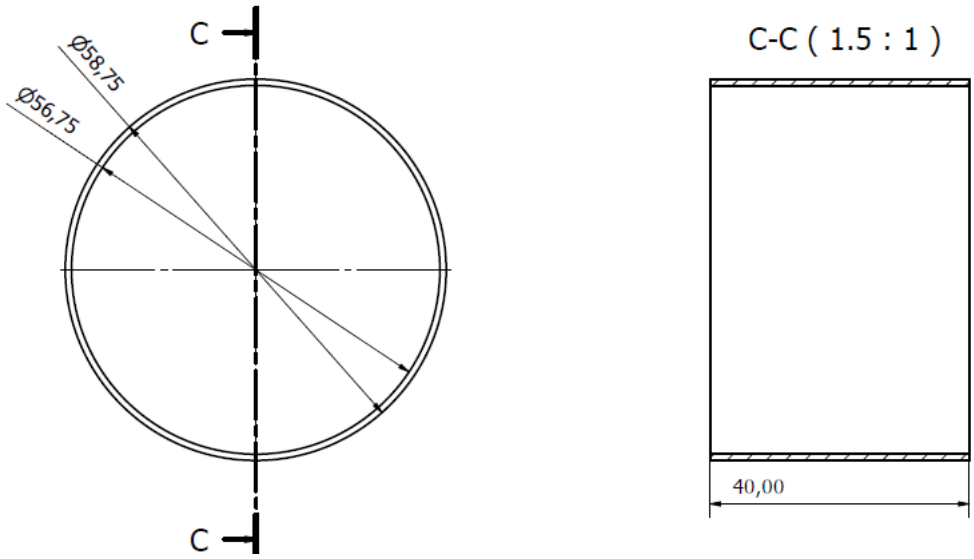

Fig. 5.2-2 Guide for the punch.

For the lubrication of the interfaces two possible configurations have been tested (figure 5.2.3):

-First soap was used to lubricate the Rubber-PTFE interface by wetting the PTFE film with liquid soap

-In the second option soap was put between two PTFE films that stood between the sample and the steel surfaces.

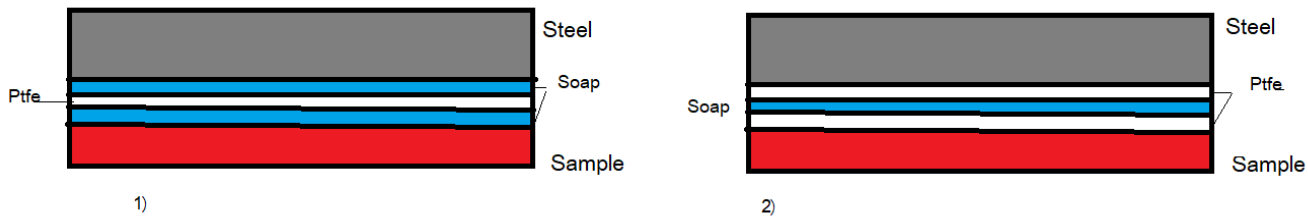

Fig. 5.2-3 Lubrication types of interface used during tests. First method on the left and second method on the right. The configuration was repeated identical for the lower surface

5.3 Friction coefficient measurement

5.3.1 Velocity estimation

As already described, during the compression tests the specimen expand laterally and as a consequence, their bottom and upper surface slip against the disk with a certain friction coefficient. To properly measure the value of this coefficient first we have to estimate the order of magnitude of the velocity at which the specimen surface travels. We can therefore exploit the incompressibility of the rubber thus setting at zero the infinitesimal volume change for a circular specimen:

$$dV = 0 = \frac{dV}{dh} * dh + \frac{dV}{dr} * dr = \pi r^2 dh + 2\pi h r dr \quad 5.1$$

$$\frac{dr}{dt} = -\frac{dh}{dt} * \frac{r}{2h} \quad 5.2$$

Being the specimen dimension given by approximately r =9 mm and h=5 mm:

$$\frac{dr}{dt}(t=0)=\frac{dh}{dt}*\frac{9}{10}=-0.9*\frac{dh}{dt} \quad 5.3$$

We can notice that radial velocity is very close to the vertical displacement velocity. Integrating the equation we can obtain the velocity variation during the test:

$$\frac{dr}{dt}(t)=\frac{Ro}{2}*\frac{1}{sqrt\left(\frac{Ho}{Ho+\frac{dh}{dt}*t}\right)}*Ho*\frac{\frac{dh}{dt}}{\left(Ho+\frac{dh}{dt}\right)^2} \quad 5.4$$

Knowing that compression test have been carried out at 3 different crosshead displacement velocity equal to about 180,18 and 1.8 mm/min the velocities at which friction coefficients has to be measured become: 162,16.2 and 1.62 mm/min.

5.3.2 Experimental apparatus

The experimental apparatus used to measure friction was inspired by the standard test method for measurement of plastic film friction ASTM D1894 [34]. The sample, which was a square sheet of about 100X100X4.7 mm, was tied to a steel weight with double adhesive tape and the whole system was weighted with a scale. The resulting normal forces slightly change due to the variations in density from one material to another, adding to the nominal value of 12N applied for all samples. The weight was then linked with a string to the crosshead of a dynamometer through a pulley as shown in figure 5.3.1. As reported in table 5.3 the tests were carried out at 3 different velocities: 162, 16.2 and 1.62 mm/min for 4 different materials. The crosshead was moved with a fixed velocity for 100 mm in the case of 162 and 16.2 mm/min but, due to the longer time needed for the lowest velocity tests, only for 40 mm in the case of 1.62 mm/min. The force needed to pull the sample was measured by the dynamometer. The friction coefficient was finally computed as:

$$COF=\frac{Ft}{Fn} \quad 5.5$$

The procedure was repeated with 4 different substrates and lubrication techniques described below and shown in figure 5.3.2:

-The first substrate was the bare steel surface of the sled.

-For the second a thin PTFE film of 200μm was fixed on the steel to study the friction between rubber and PTFE

-In the third case the interface between rubber and PTFE was lubricated by wetting the whole film with soap

-The last configuration consisted in putting two free PTFE film lubricated with soap between the sample and the steel substrate

These configurations aimed at representing the different frictional interfaces acting during the compression tests realized both in this work and in the previous work by [19].

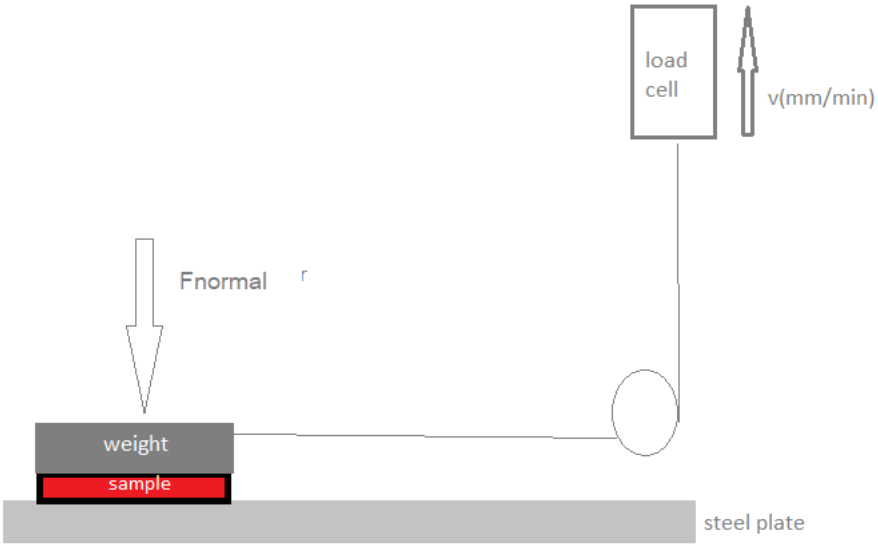

Fig. 5.3-1 Experimental apparatus for COF measurement

Velocity(mm/min)	Run(mm)	Normal Force (N)
162	100	12
16.2	100	12
1.62	40	12

Table 5.3 Parameters of friction sled experimental tests

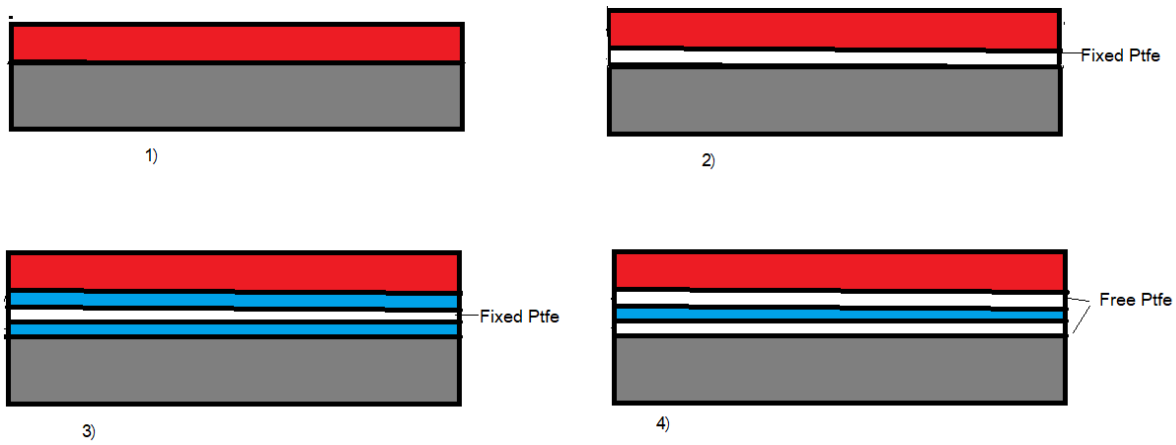

Fig. 5.3-2 Interface between sample and sled substrate with different lubrication systems. Grey= steel substrate, red= sample, white= PTFE film, blue=soap layer

5.4 Numerical simulations of compression and stress relaxation tests

Numerical simulations of the compression and stress relaxation were carried out. In particular different models were created on the commercial software for FEA analysis Abaqus 2018. These simulations were than run changing the friction coefficient between the disks and the sample in order to investigate how the amount of friction influences the results of the test.

5.4.1 2D axisymmetric model

The first model created was a 2D axial symmetric one. The sample was modeled as deformable shell and meshed with hybrid elements CAX4RH. Dimension of the sample were given by [19] as h=4.7 mm and r=9 mm. The bulk of the sample was defined as homogeneous with properties including time domain Prony viscoelasticity, general density and hyper elasticity defined with instantaneous coefficients. Compression disks were instead modeled as analytical rigid wire surfaces. Given that steel has much higher stiffness than rubber there was no need to model them as deformable bodies. Surfaces had a normal hard contact component and a penalty friction tangential behavior. As boundary conditions (summarized in figure 5.4.1) instead the lower disk was clamped while the upper one was vertically displaced to reach a 40% vertical deformation of the specimen. In the case of compression tests the displacement was applied in a single dynamic implicit quasi

static step, with a time varying between 0.6667 s, 6.667 s and 66.67 s according to the strain rate desired. For stress-relaxation tests instead two steps were needed: the first is equivalent to the one for compression tests except for the final value of deformation and time of the step which are: 30% deformation in 5s and 10% deformation in 1.667s. The second is still a dynamic implicit step of 300 s in which the displacement is maintained fixed at its last value while time elapses.

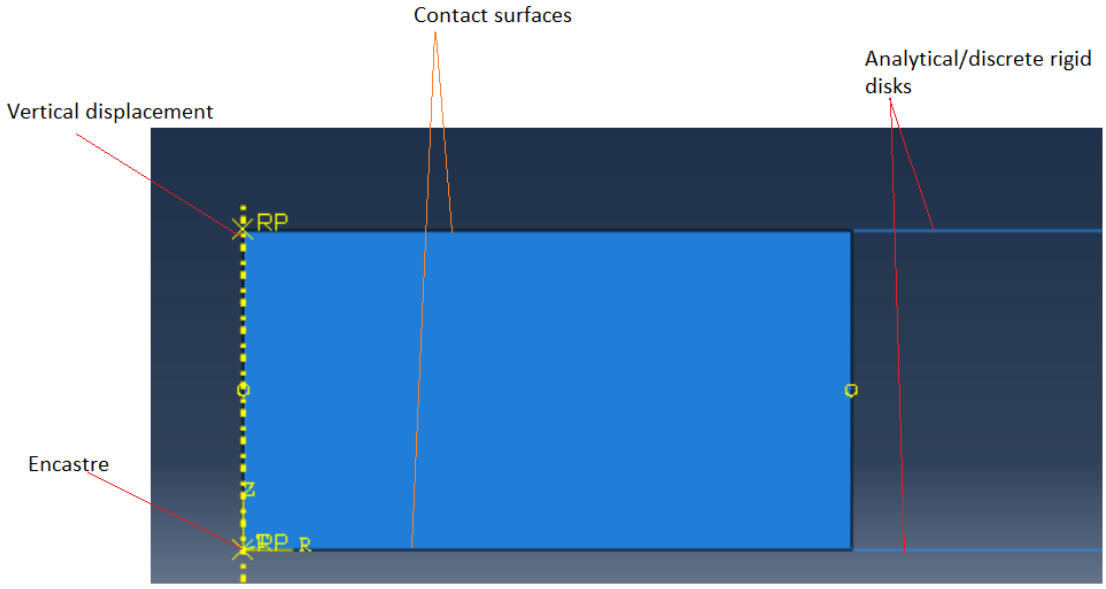

Fig. 5.4-1 Assembly and BCs for 2D axisymmetric model.

5.4.2 3D model

A completely equivalent 3D model was also created by designing just a quarter of the sample and putting Y and X symmetry boundary conditions on the cut faces of the sample. In this case C3D8RH hybrid elements were used. The assembly is shown below in figure 5.4.2, the red face is the Y symmetric one while the blue is the X symmetric one.

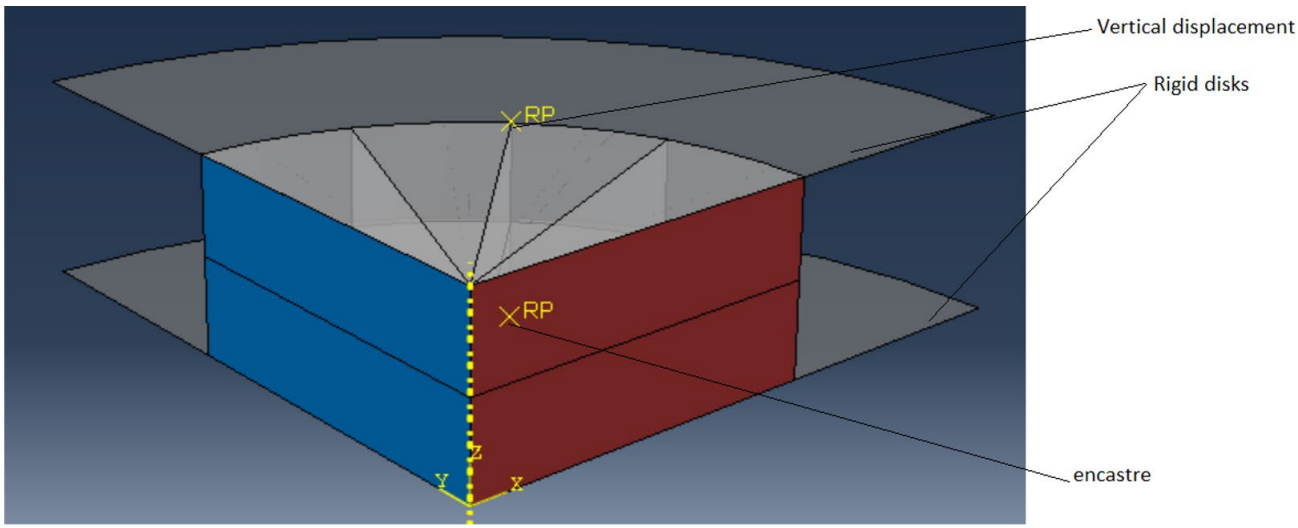

Fig. 5.4-2 Assembly and BCs for 3D axisymmetric model. Red face is the Y symmetric one while the blue is the X symmetric one.

5.5 Friction sled simulations

The friction sled test were simulated too, also in this case both 2D and 3D models were developed. The sample was a rectangular rubber block and it was tied to a rigid body on which a body force corresponding to the sample-weight system mass was applied along with a horizontal displacement of 100 mm. The substrate was again fixed as rigid surface fixed in its reference point and with friction contact defined as before with the sample.

5.5.1 2D sled

In the 2D model the substrate and the weight are two rigid wires while the sample is a 2D deformable planar body. The analysis is divided in two steps: application of the gravitational force and sliding of the sample. In the former a 12 N body force is applied on the weight statically (static general step) to neglect viscoelastic effects which shall not be considered in this phase. The second step is a horizontal displacement at given velocity (step time) of the weight reference point (RP). The sample must move with the weight and for this reason they are tied at the interface. The substrate instead present a hard normal contact behavior along with a tangential penalty friction.

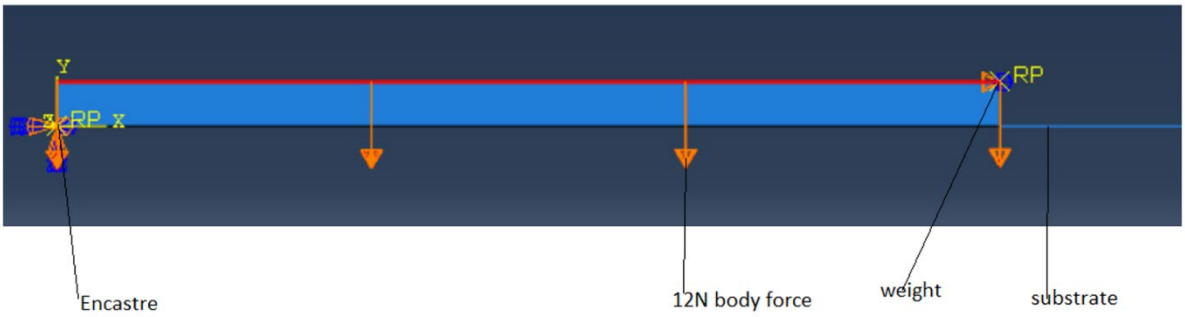

Fig. 5.5-1 Assembly and BCs for 2D sled model.

The mesh adopted is a simple all quad CPS4R 2D mesh showed in figure 5.5.2.

Fig. 5.5-2 Mesh used for the 2D sled model.

5.5.2 3D sled

The 3D model is composed by 2 discrete rigid planar bodies which represent the weight and the substrate and a 3d deformable body is used for the sample. The boundary conditions and steps are the same as described for the 2D model, in particular the force is applied as a surface pressure which corresponded to a total load of 12N. Elements used are C3D8RH and the mesh is represented below in figure 5.5.4.

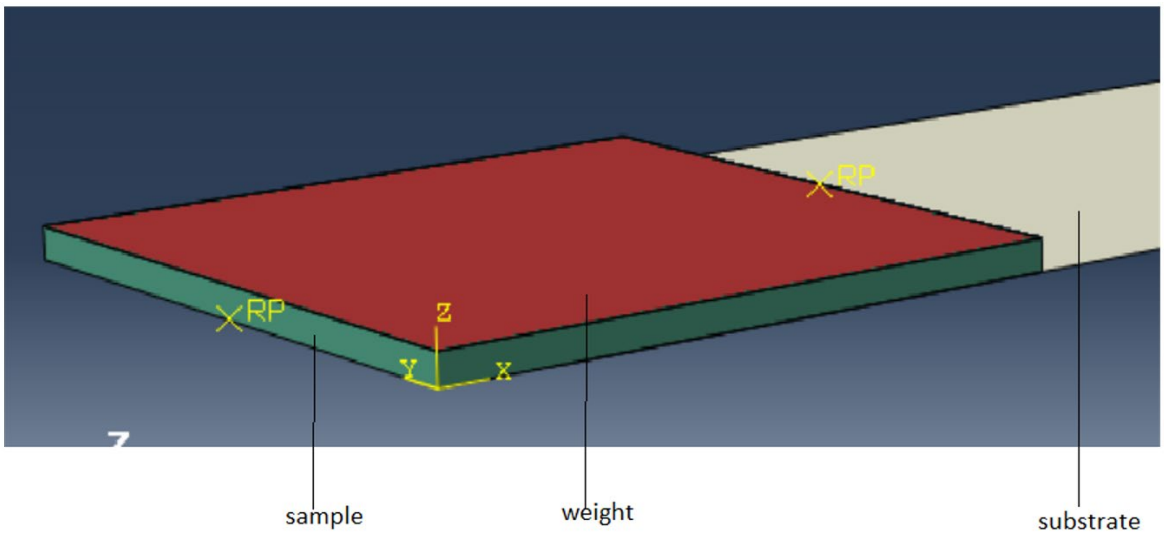

Fig. 5.5-3 Assembly and BCs for 3D sled model.

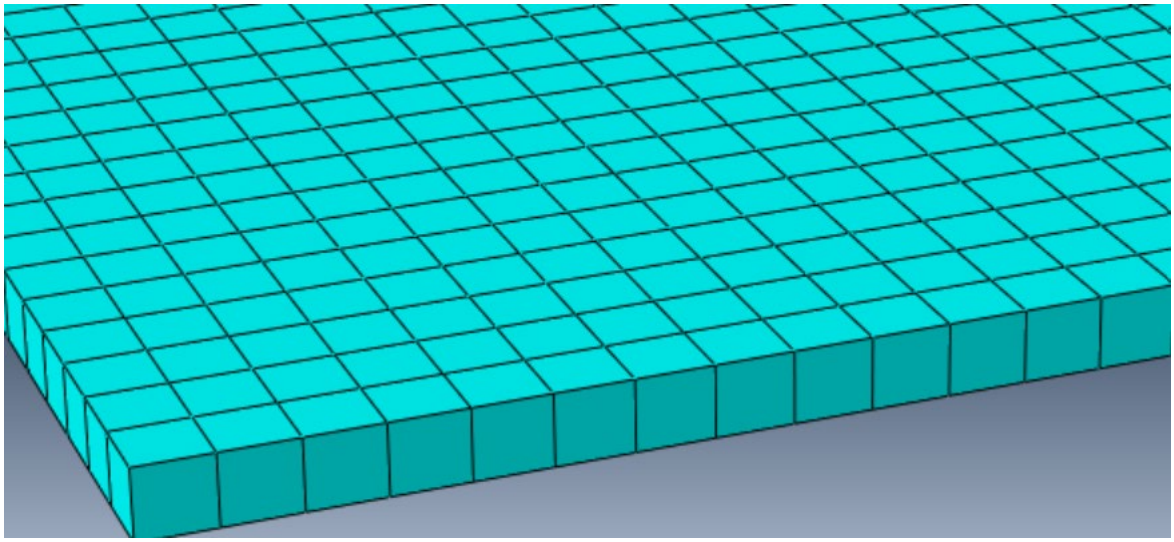

Fig. 5.5-4 Mesh used for the 3D sled model.

5.6 Mesh of the models for compression and stress relaxation tests

In order to account for the very large displacement and deformation of the sample during a 40% strain input, different meshes have been tried to help convergence and

to get the best and most accurate solution. In particular convergence problem can show up as the lateral surface rolls over coming in contact with the disk. Also a mesh sensitivity analysis comparing the results from different meshes was carried out. All the meshes that were tested during the work are presented below

5.6.1 Mesh for 2D axisymmetric model

Mesh A: First mesh was a simple all-Quad structured mesh.

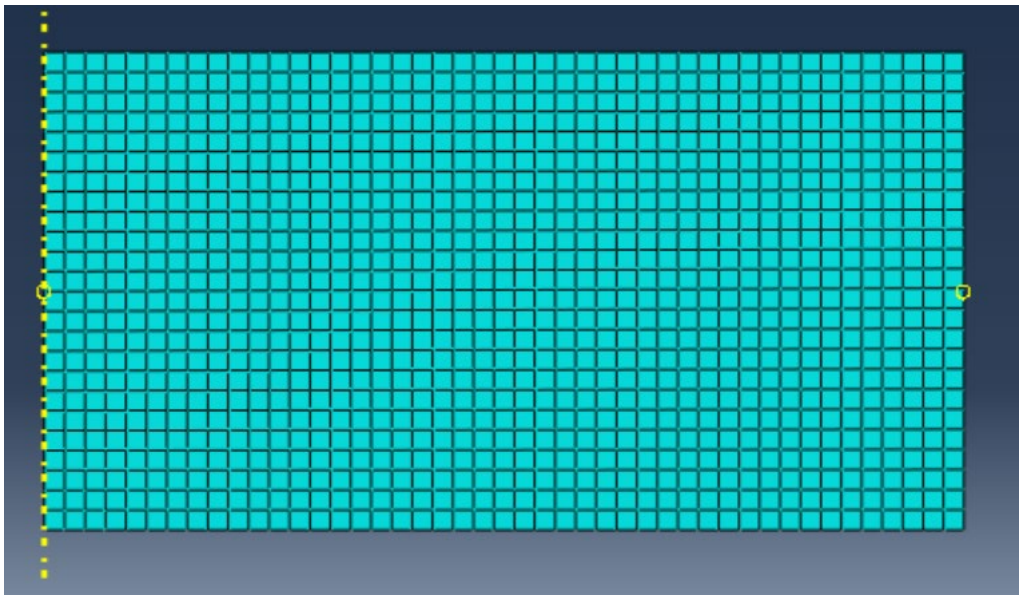

Fig. 5.6-1 Mesh A for 2d axisymmetric model

Mesh B: in mesh B a biased seed was added on the vertical edges in order to refine mesh on the corner which is the most critical point.

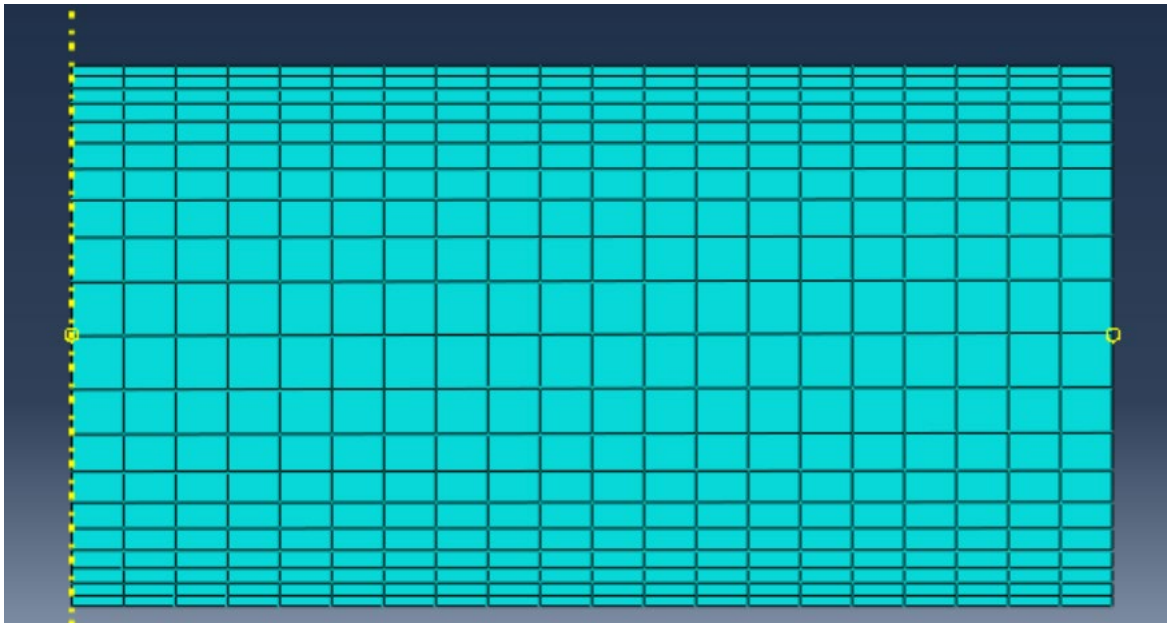

Fig. 5.6-2 Mesh B for 2d axisymmetric model

Curvature radius (Mesh C): A little curvature radius (0.1 mm) was added at the corners to help convergence when the friction is high enough to provoke a lateral surface roll-over. The sample face was also partitioned in order to have a sweep mesh on the corners and a structured one in its bulk.

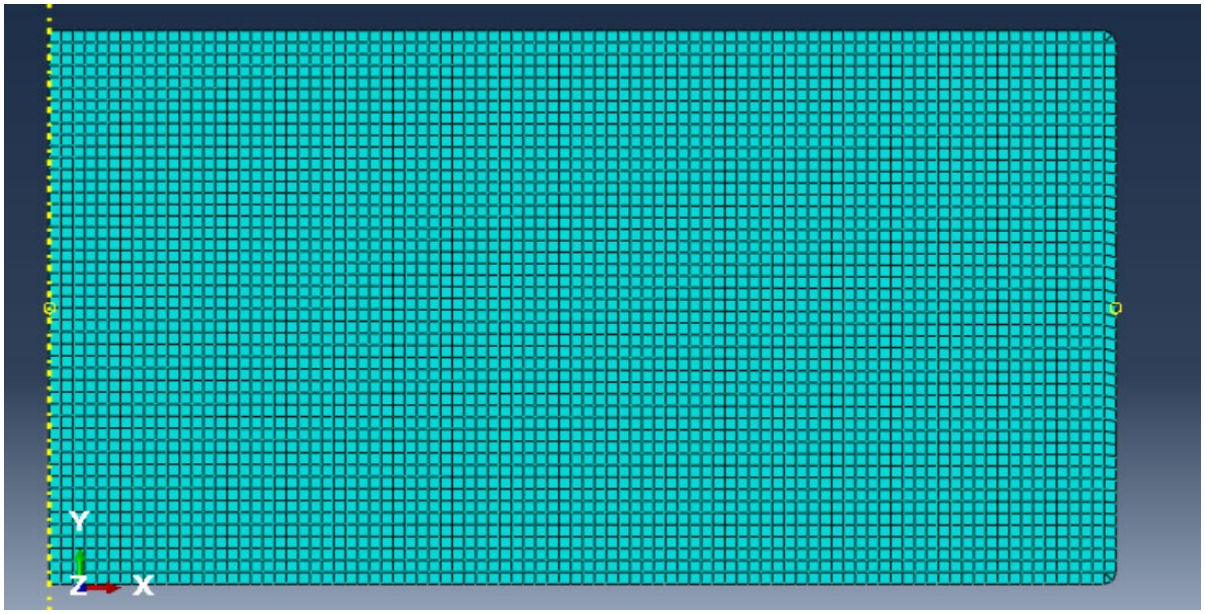

Fig. 5.6-3 Mesh C for 2d axisymmetric model

Remeshing rule meshes: An adaptive mesh procedure with 2 iterations was also run. The analysis requires an error indicator value to decide where and how the mesh has to be modified. In this case the selected error was the distortion energy error indicator ENDENERI. All error indicators are only available for static general or explicit step field output, as a consequence for this analysis a static general step had been selected thus neglecting the viscoelastic properties of the material. The iterative procedure started from a mesh of type B and then was automatically updated by the software to minimize the error indicator selected.

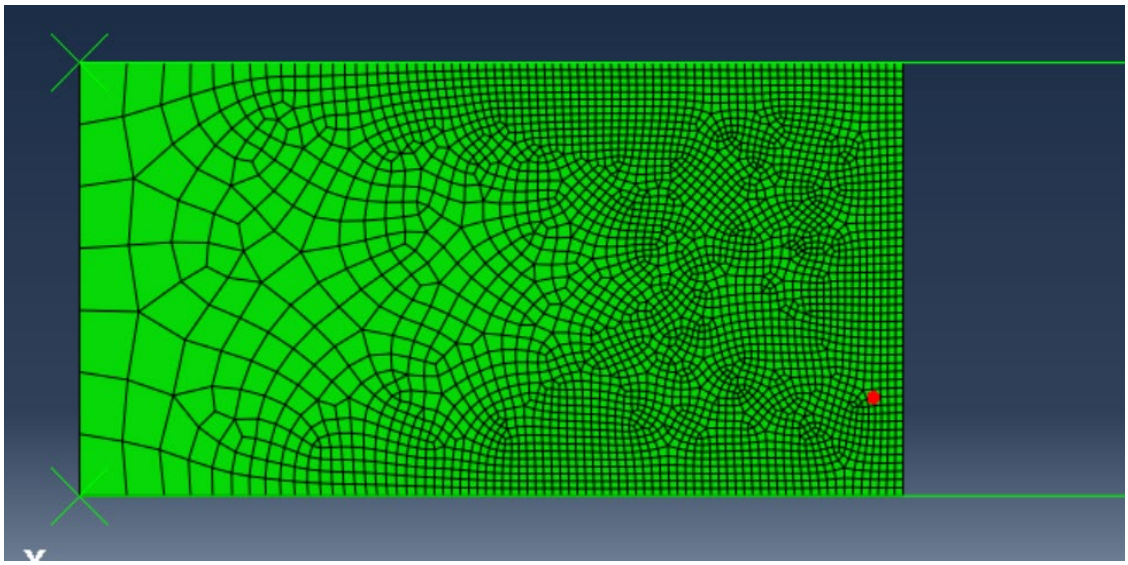

Fig. 5.6-44Mesh after first iteration for adaptive mesh procedure.

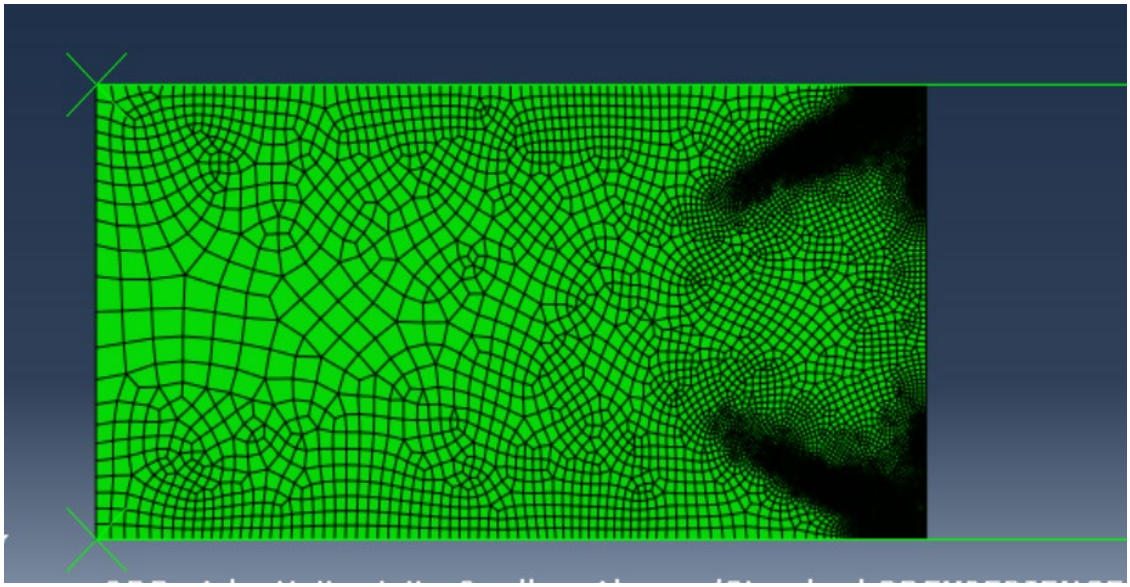

Fig. 5.6-5 Mesh after second iteration for adaptive mesh procedure.

5.6.2 Mesh for 3D model

Sweep mesh: First mesh used for the 3D model was a sweep mesh like the one shown below

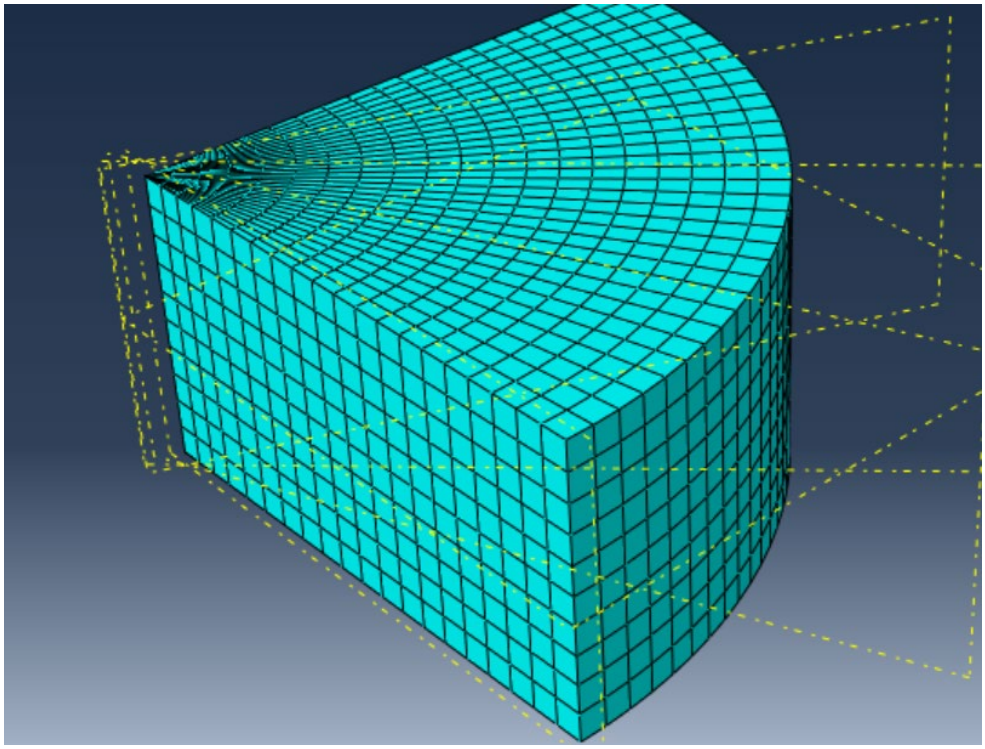

Fig. 5.6-6 Mesh sweep for 3d model

Structured mesh: After partitioning the sample in 8 equivalent parts with a height equal to one half of the sample height and an angle of 22.5 degrees it was possible to use a structured mesh as the one shown below. Anyway the mesh presented many distorted elements as we can observe looking at the upper face of the sample.

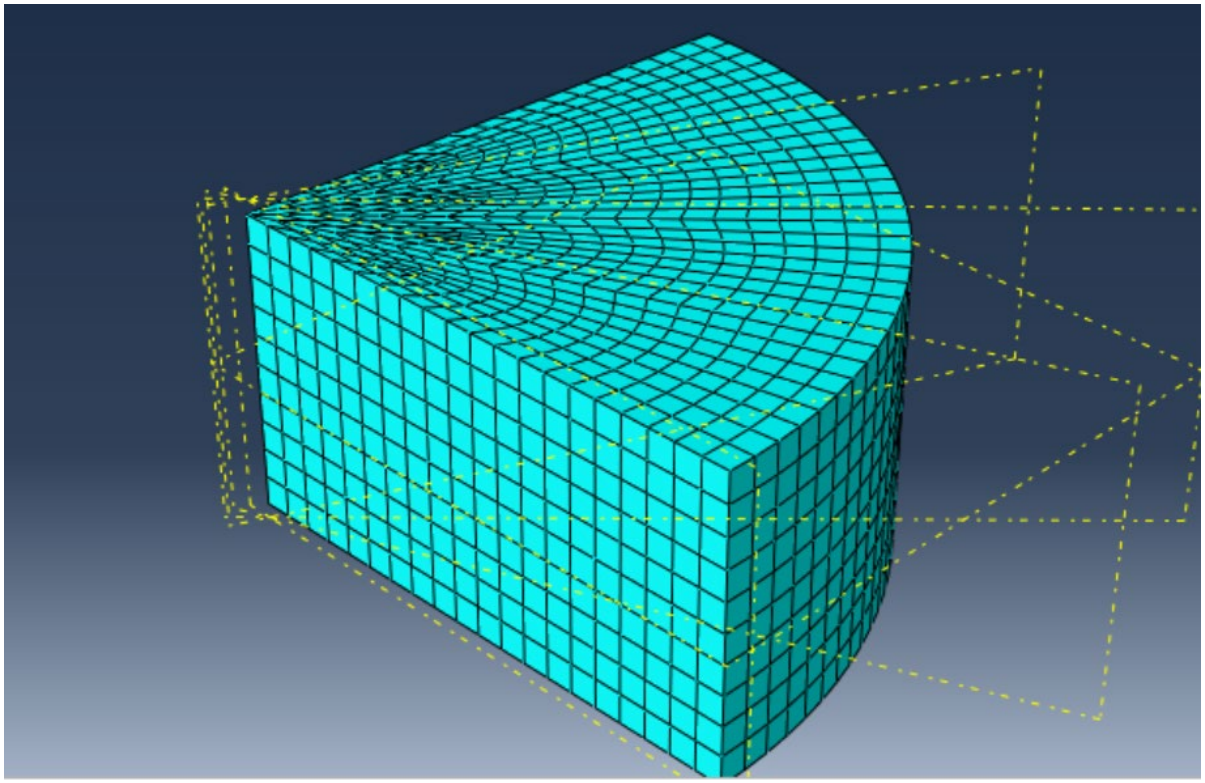

Fig. 5.6-7 Mesh structured for 3d model

5.7 Fitting procedure

The fitting procedure used to extrapolate new material coefficients is the same described in [19]. The procedure is divided in different steps:

1. Curves that must be fitted are sampled through linear interpolation at specific times. The sampling parameters are shown in table 5.4.
2. Time, stress and stretch data obtained from the sampling are inserted in the excel file in figure 2.4.2 that computes the total sum of the square differences between the experimental stresses input in the file and the stresses computed with the visco-hyperelastic model described above from the given stretch history.
3. The excel solver is run to minimize the sum of the square errors varying the cells representing the hyperelastic coefficients and the Prony series dimensionless moduli g_i while the τ_i values were fixed at 0.3,3,30 and 300 seconds. The g_i values were constrained to be positive and their sum had to be equal to one.

4. Newly identified coefficients are collected and implemented in the experimental tests models to compare simulation results with the experimental data fitted.

Test	Velocity (s^{-1})	Strain (%)	Δt (s)	Number of points
Compression	0.006	40	0.1	667
Compression	0.06	40	0.01	667
Compression	0.6	40	0.001	667
Stress relaxation	0.06 (ramp)	30	0.1	3050
Stress relaxation	0.06(ramp)	10	0.1	3017

Table 5.4 Sampling of curves for fitting

6. RESULTS AND DISCUSSION

6.1 Compression and stress relaxation tests results

6.1.1 Compression tests results

The results of compression tests are presented as stress-stretch curve which are obtained after the elaboration of the Force-displacement data given by the dynamometer. Firstly the toe of the curve was removed; then a correction had to be applied due to the intrinsic compliance of the compression apparatus. To remove the toe, curves were shifted horizontally by a value found with the intercept of two linear fits: one representing the approach phase and one representing the first part of the loading curve. An example is shown in figure 6.1.1.

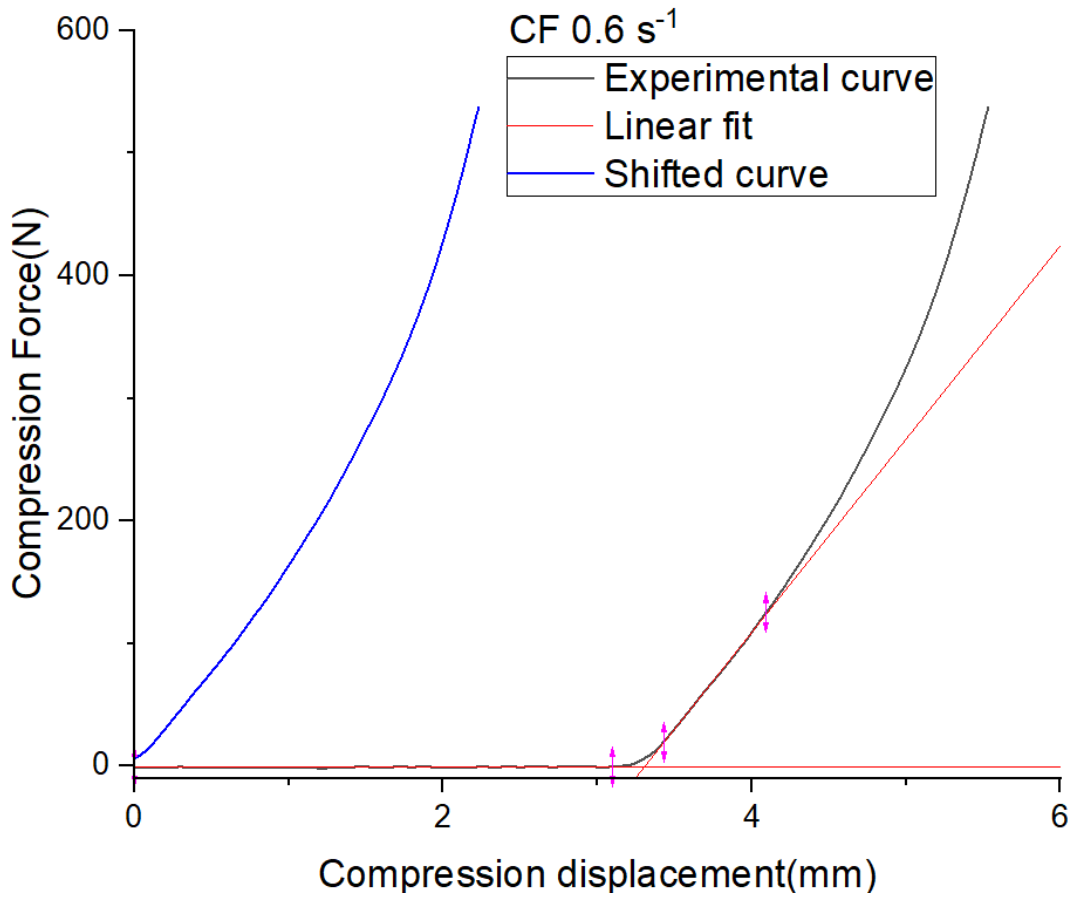

Fig. 6.1-1 Example of curves toe removal.

To apply the compliance correction instead a specific formula for the machine was used [19].

$$u = u_{ch} - 2.07793 * 10^{-4} \left[\frac{mm}{N^{0.72848}}\right] F^{0.72848} \qquad 6.1$$

where u is the displacement corrected, u_{ch} is the measured compression displacement and F the output compression force. These curves are shown in comparison with the ones obtained in [19] for PTFE and bare steel interfaces. The two configurations described in 5.2 were compared. Apparently they both gave the same result as it can be observed in figure 6.1.5 for material LG. This is probably due to the fact that soap permeates through the PTFE film during the compression wetting in this way all the interfaces. It was observed in fact that at the end of the test the sample had soap on its surfaces even if the lubricant had been put between the two PTFE films. Figures 6.1.2, 6.1.3 and 6.1.4 show that the addition of soap as liquid lubricant has a visible effect on the curves proving that the use of dry PTFE was not enough to avoid

friction influence , although effective in reducing it compared to bare steel [19]. We can observe that the effect of soap is more and more visible as velocity is increased. This result, as we will see in the next paragraph, is in agreement with the friction sled results: in fact the friction measured with soap is relatively constant with velocity while it is highly dependent on velocity for other interfaces. For what concerns the guide for the punch it was observed that the sample was actually still during the compression so there was no need to use the guide at any test velocity. It is possible that the problems encountered by the author of [19] were due to a poor alignment of the lower plate.

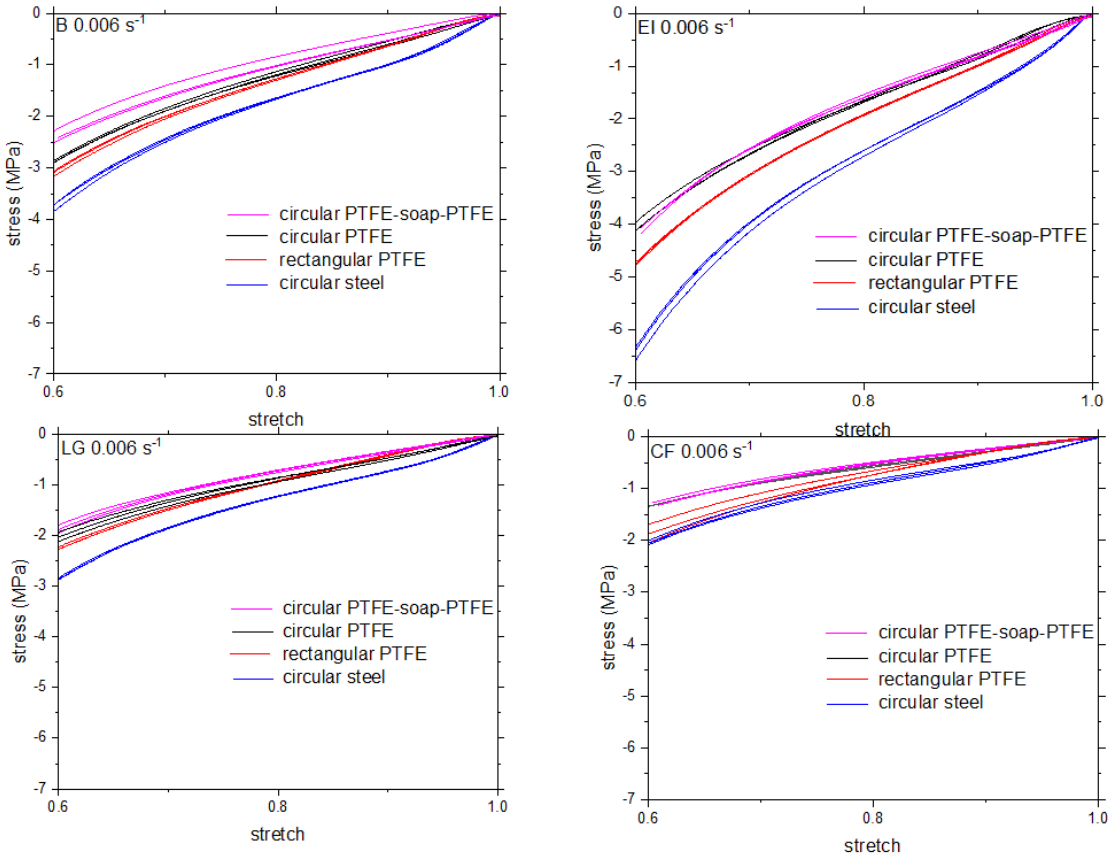

Fig. 6.1-2 Results of compression tests at 0.006 s^{-1} for all materials for different interfaces and shapes.

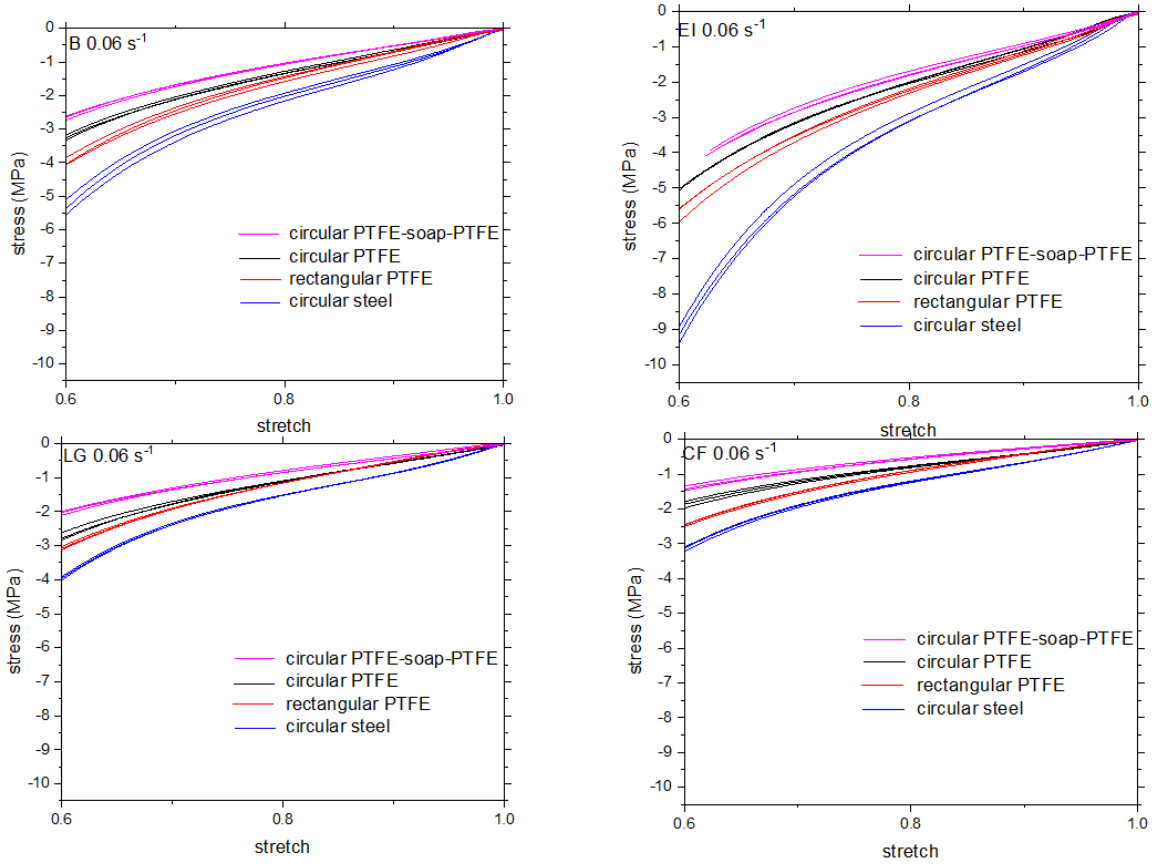

Fig. 6.1-3 Results of compression tests at 0.06 s^{-1} for all materials for different interfaces and shapes.

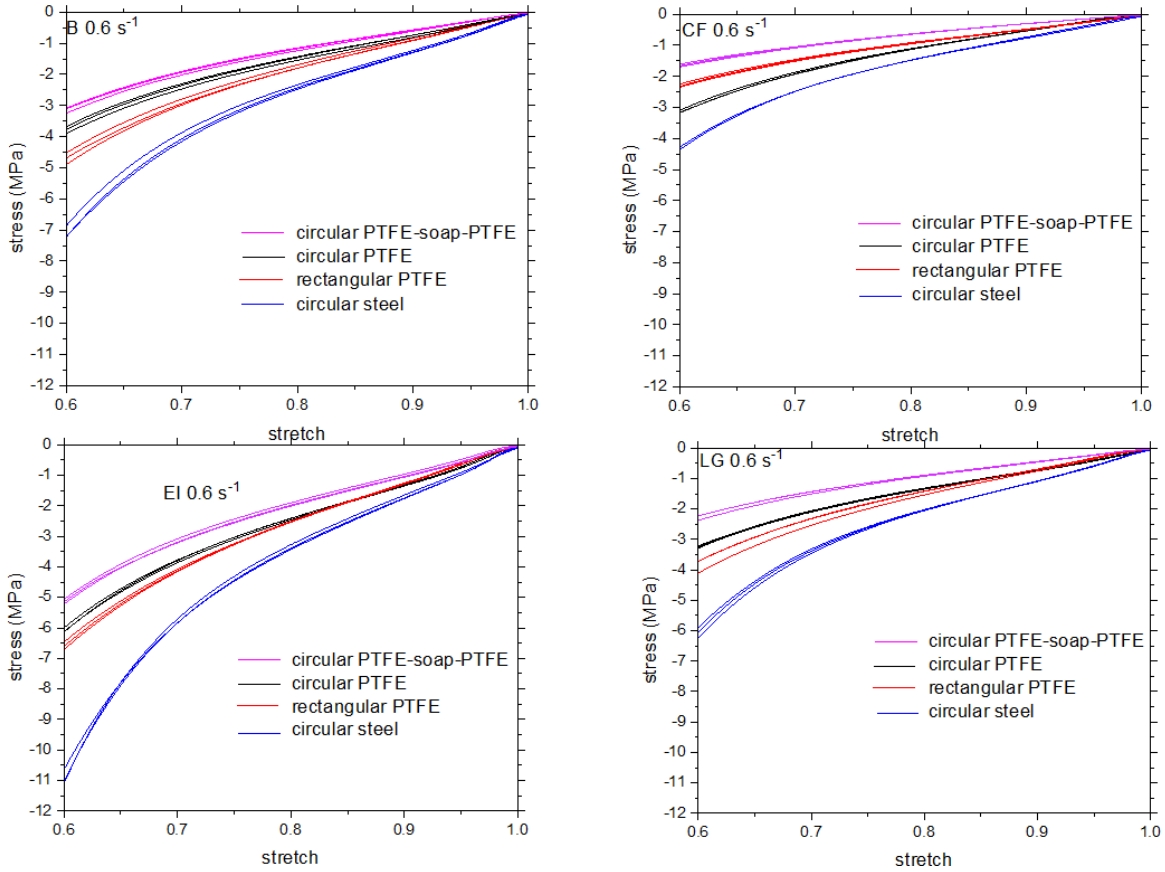

Fig. 6.1-4 Results of compression tests at 0.6 s^{-1} for all materials for different interfaces and shapes.

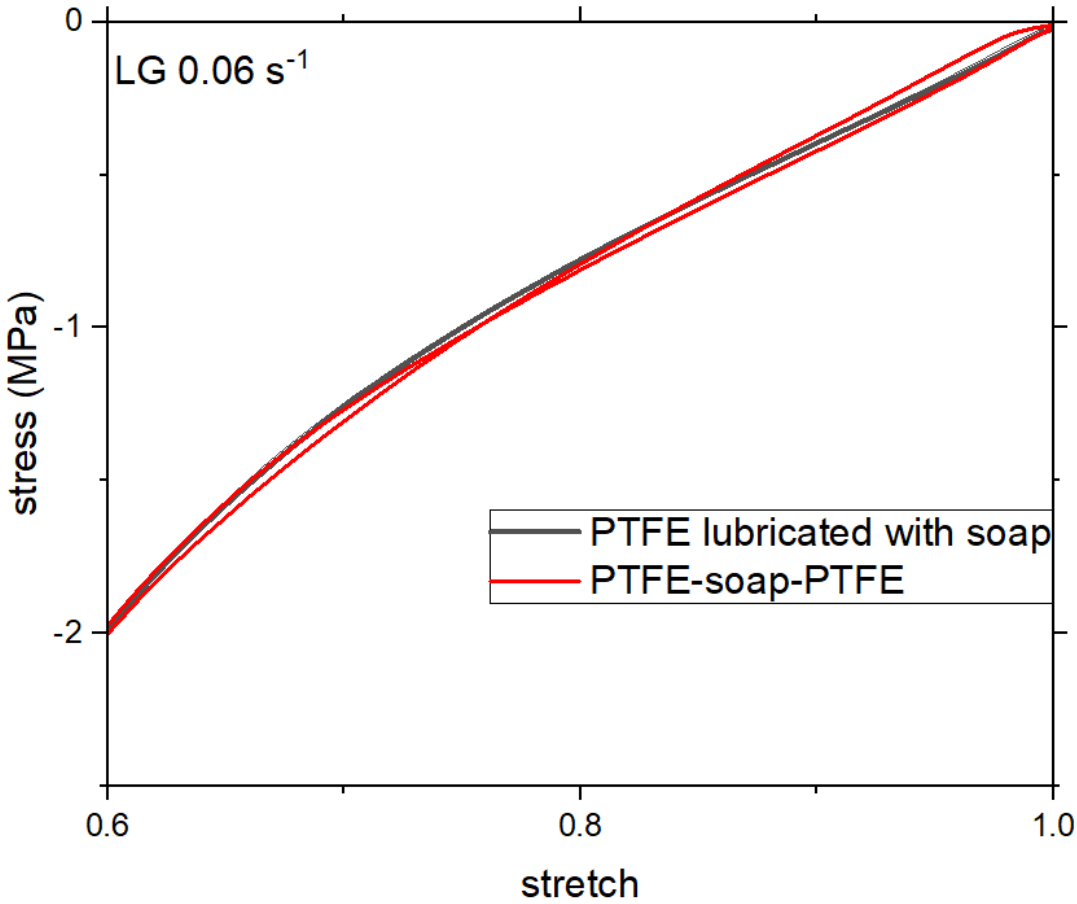

Fig. 6.1-5 Comparison between the two configurations with soap.

6.1.2 Stress-relaxation results

The results of stress relaxation tests for the PTFE-soap-PTFE configuration are shown in figures 6.1.6 and 6.1.7 in comparison with the results obtained by [19]. The same correction of compression tests were applied to the stress-relaxation tests data. Finally also for these curves the reduction of the friction influence by the addition of soap is visible.

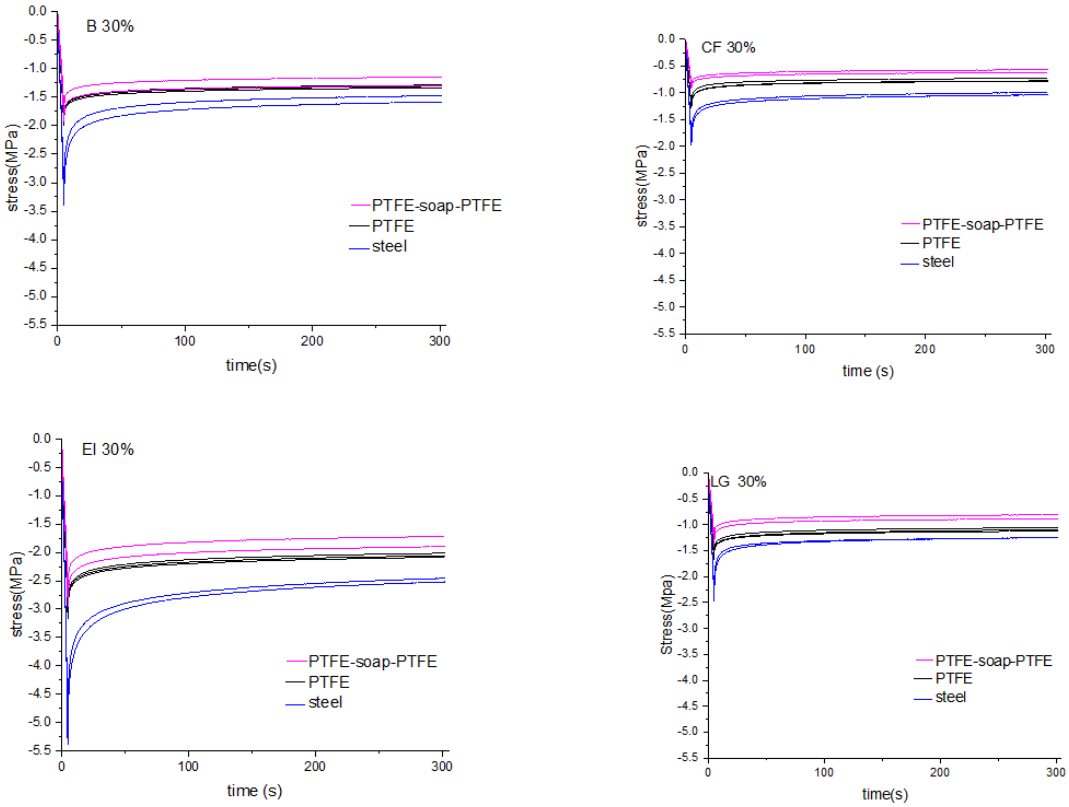

Fig. 6.1-6 Stress relaxation with stretch 0.70 results for all materials

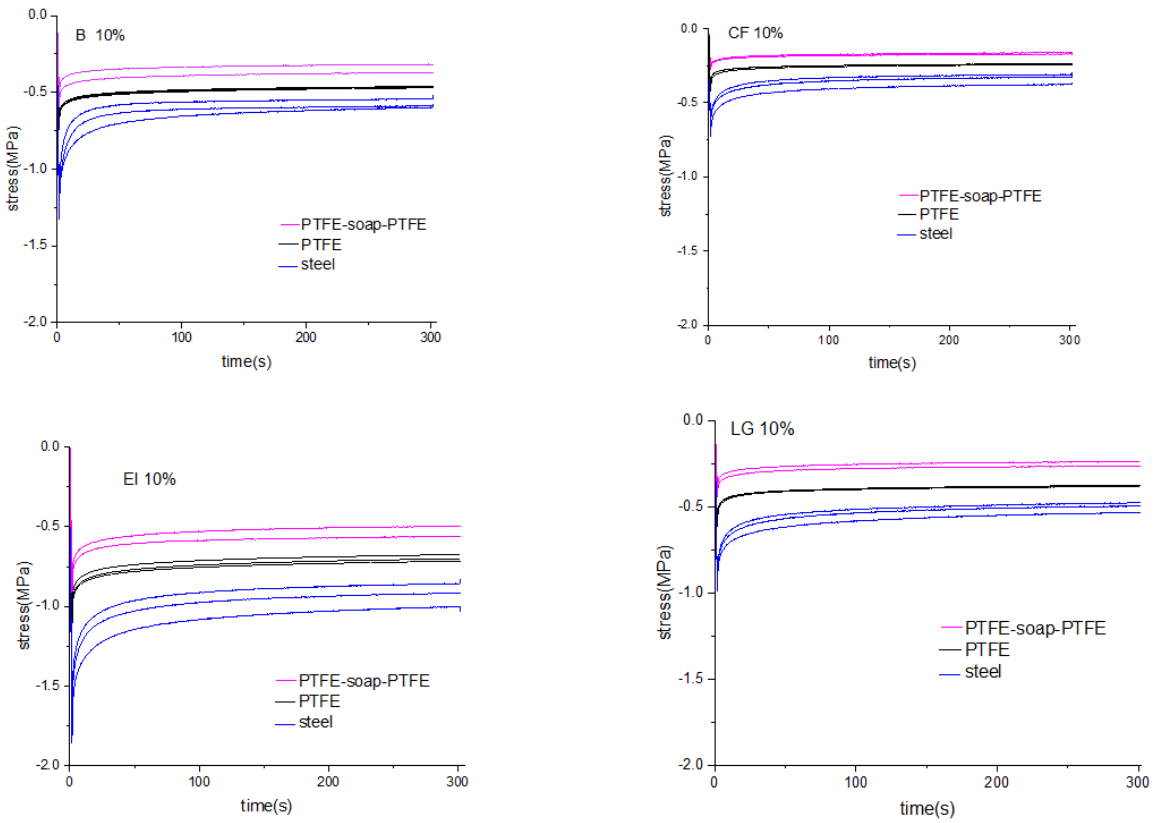

Fig. 6.1-7 Stress relaxation with stretch 0.90 results for all materials

6.2 Friction sled experimental results

In this paragraph results of the friction coefficient, measured as described in 5.2, are presented. The COF values are plotted versus the logarithm of the velocity. It is possible to observe that the friction coefficient of rubber against steel is very high (around unity) while of course values decrease from 0.2 to 0.7 when PTFE is added. Higher values of COF are generally recorded at higher velocities but this trend seems to vary according to the material: in fact, values measured on EI are quite constant while CF shows a greater dependence on velocity. EI also shows the lowest values of friction while CF has the highest, reaching values up to 1.6 against steel. As anticipated before when soap is added the dependency of COF on velocity vanishes. The values measured are around 0.1-0.2 and seems to be consistent with the ones found for PTFE and steel. The addition of soap, as shown by the graphs 6.2.1, has a visible effect in decreasing the value of COF. Finally in figure 6.2.2 the results for the PTFE-soap-PTFE system are presented. As expected the COF for this configuration

doesn't depend on the material tested. In fact, as it was possible to observe form the experiment, the sliding occurred between the two PTFE films thus the measured COF was the one of the PTFE-PTFE lubricated interface. The values measured are around 0.1 and are quite independent on velocity.

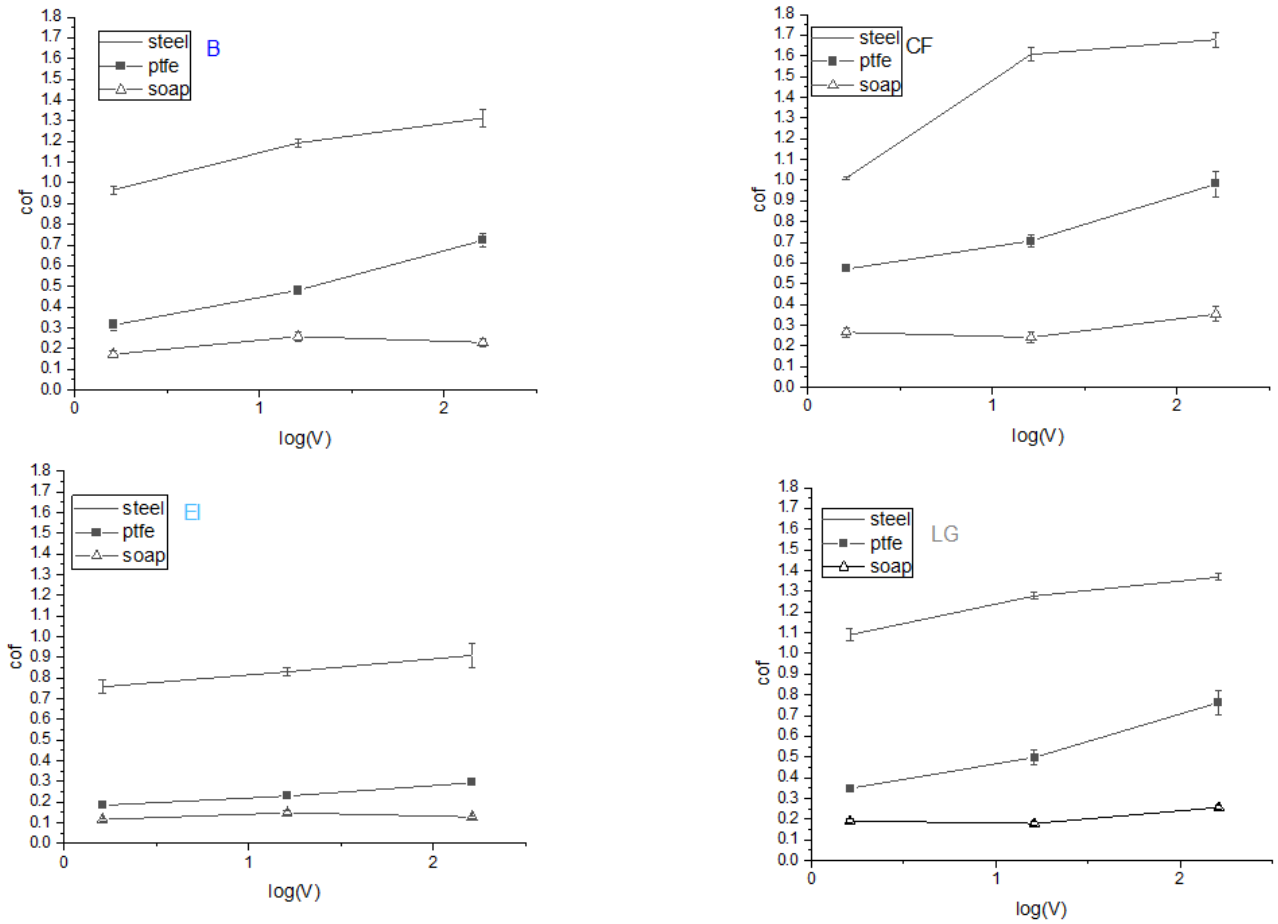

Fig. 6.2-1 COF against log (v) for all materials for steel, PTFE and soap lubricated PTFE interfaces

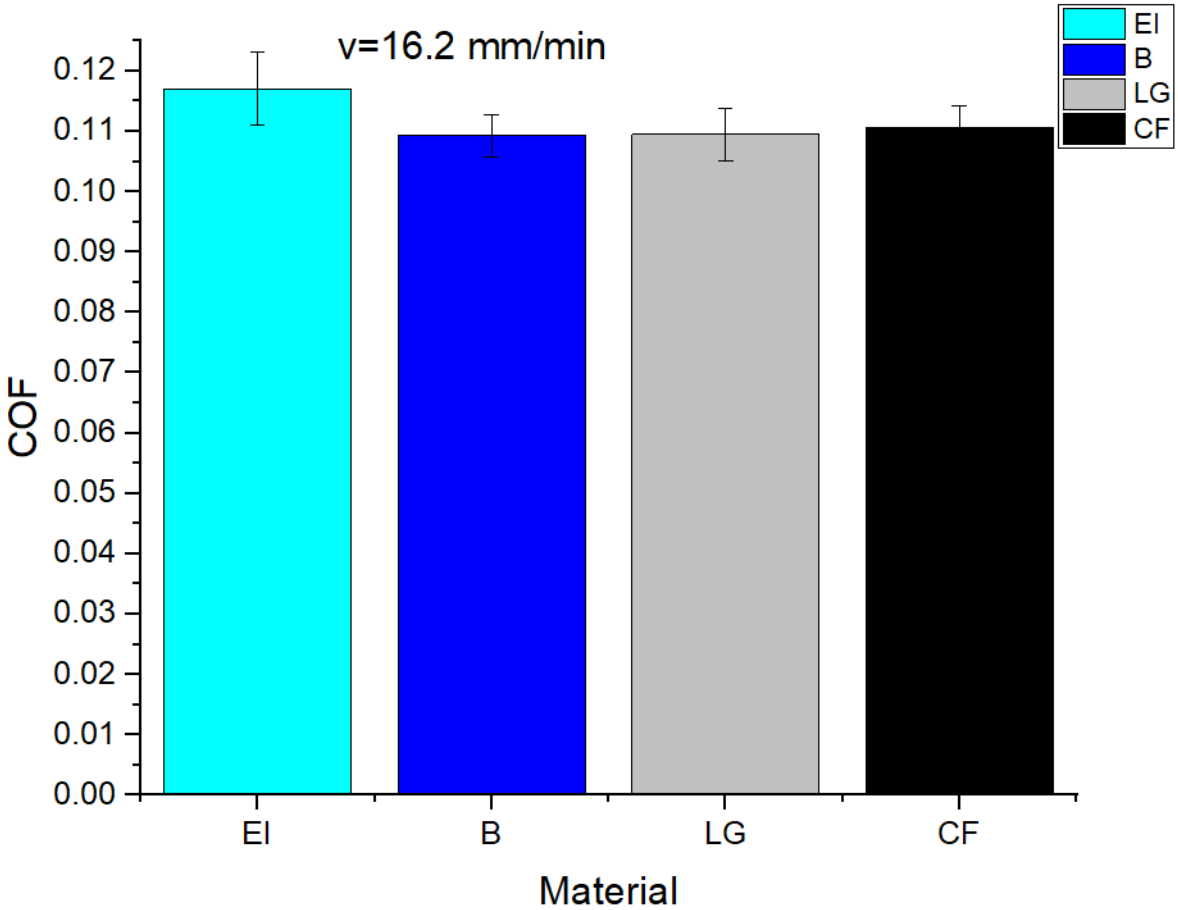

Fig. 6.2-2 COF of PTFE-PTFE lubricated interface at 16.2 mm/min. Results obtained are almost velocity independent

6.3 Simulation of compression results

6.3.1 Model: Compression between platens

Results from simulations carried out with ABAQUS as described in paragraph 5.3 are here presented. To extrapolate compression curves from the field output the vertical component of reaction force taken at the reference point of the movable disk is plotted along with the vertical displacement of the same point. It is then easy to calculate nominal stress and stretch through the use of these formulas:

$$\sigma = \frac{RFv}{A} \quad 6.1$$

$$\lambda = \frac{Uv}{H} \qquad 6.2$$

Where A is the cross-sectional area of the specimen, RF_v is the vertical reaction force U_v the vertical displacement and H is the initial height of the specimen. In this way stress-stretch curves are plotted.

6.3.2 Mesh type sensitivity

The influence of mesh type used on stress-stretch curves is investigated in this paragraph. Changing from a mesh of type A to the one of type B has no effect when friction value is low (0.1) and has an almost negligible effect when COF is higher (0.6-1). However it helps convergence and gives a smoother solution when COF is 0.3.

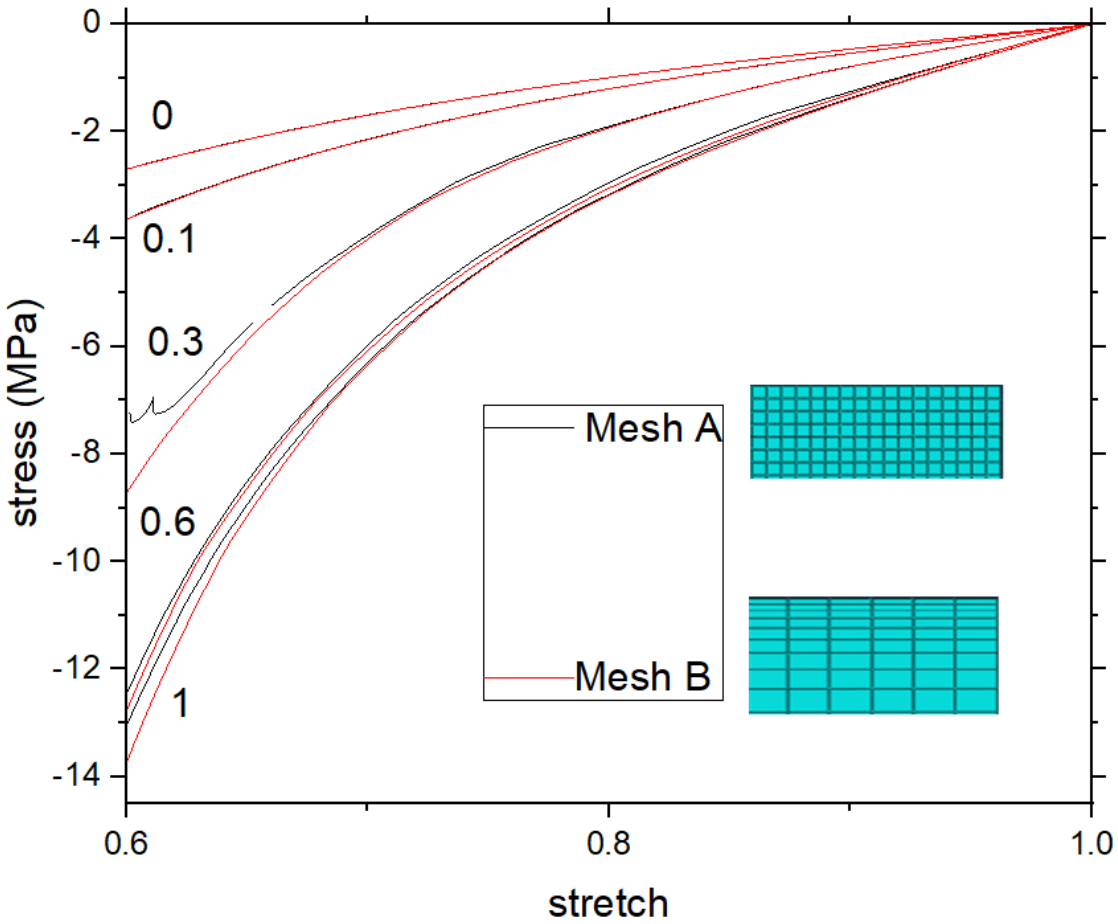

Fig. 6.3-1 Comparison between mesh A and B for different values of COF, material B (Mooney-Rivlin) at 0.006 s^{-1}

Almost the same considerations can be done when a curvature radius is added on the specimen corners (mesh C).

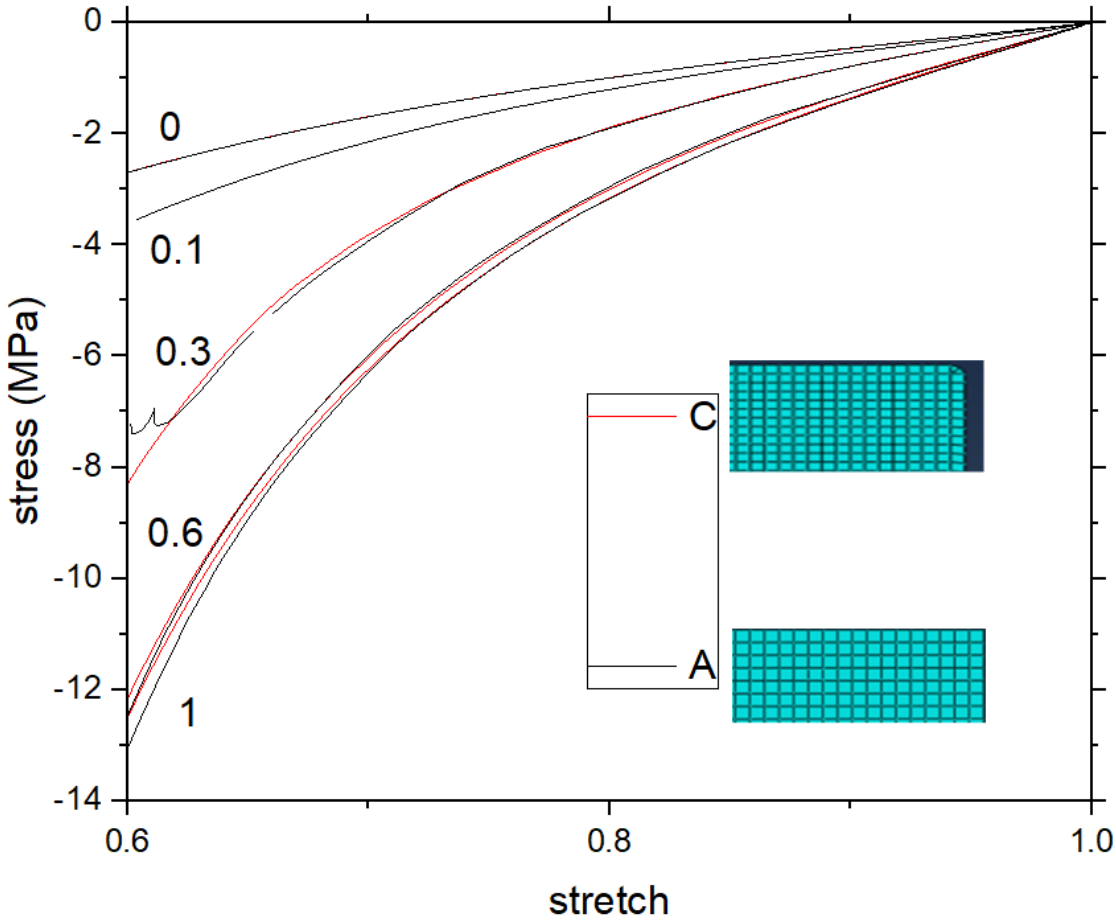

Fig. 6.3-2 Comparison between mesh A and C for different values of COF, material B (Mooney-Rivlin) at 0.006 s^{-1}

6.3.3 Mesh size

A mesh size sensitivity was also carried out to find out what was the ideal mesh size in terms of results accuracy and computational time. For mesh C an example is reported for COF equal to 0.6 and 0.3. Meshes with seed size from approximately 0.2 mm to 0.025 mm were tested. It was observed that a mesh of 0.1 mm approximate size is a good compromise between accuracy and computational cost.

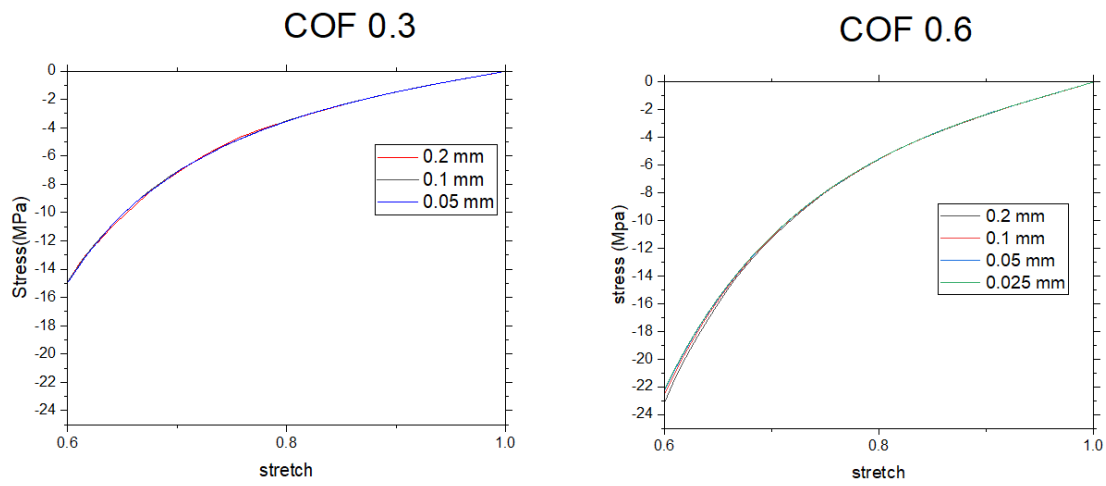

Fig. 6.3-3 Mesh C sensitivity for COF 0.3 and 0.6 EI (Mooney-Rivlin) 0.06 s^{-1}

Similarly on mesh B an optimal mesh of maximum approximate size of 0.2 and minimum size at the corners of 0.09 was adopted.

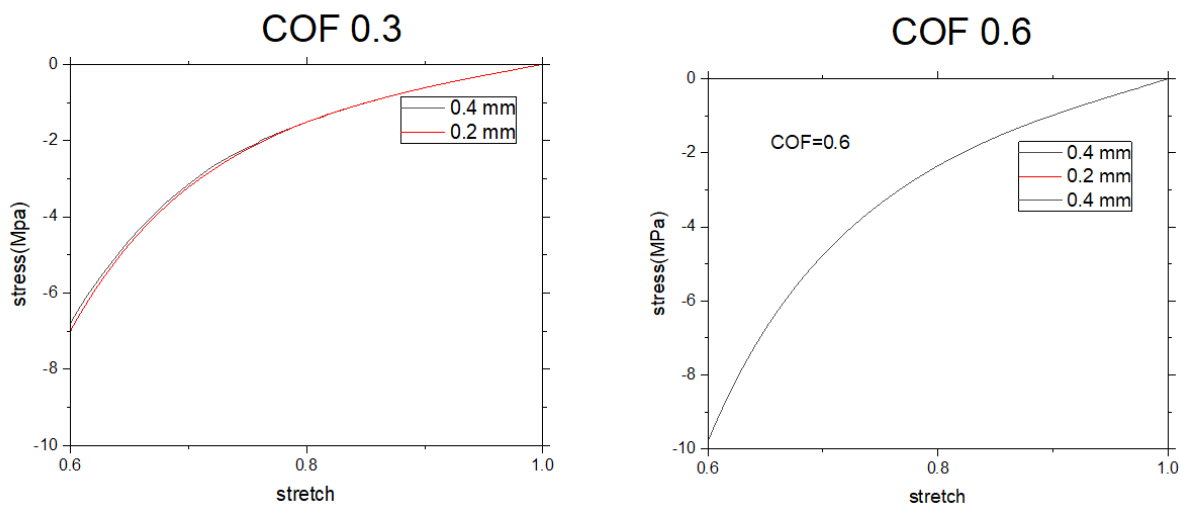

Fig. 6.3-4 Mesh B sensitivity for COF 0.3 and 0.6, LG (Mooney-Rivlin) 0.06 s^{-1}

Finally mesh size was analyzed on mesh A, here an example is reported in figure 6.3.5 for lower friction curves. For COF 0.22 and a mesh size of 0.4 mm the solution was not smooth while when the mesh was refined this problem disappeared.

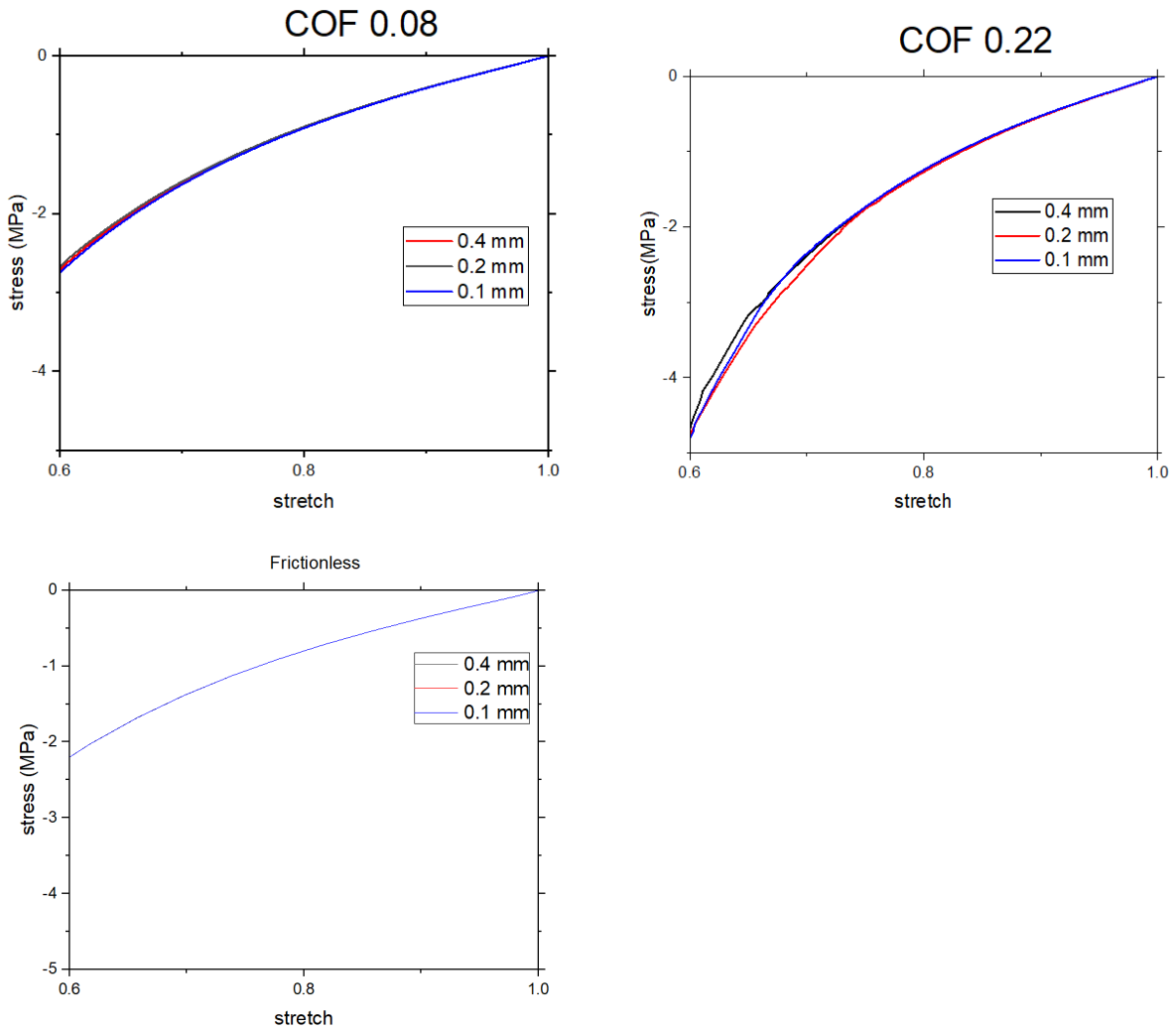

Fig. 6.3-5 Mesh A sensitivity for COF 0.08 and 0.22 and 0 LG (Mooney-Rivlin) 0.006 s^{-1}

6.3.4 Other parameters

The influence of other parameters on the stress-stretch curve and on the contact behavior was investigated.

-First the use of discrete rigid bodies instead of the analytical rigid ones seemed to have no influence on simulations nor in terms of solutions, as expected, neither for the convergence of the analysis.

-Changing the normal contact stiffness or using an exponential normal behavior can be useful to help convergence. However in our case it didn't seem to have any significant effect.

-The contact slip tolerance of the tangential behavior which is the amount of slip that a node can undergo even if, for the friction constraint, it should be in non-slip condition doesn't seem to have any effect even if changed of different orders of magnitude.

-The use of an adaptive mesh didn't result in any improvement of the model accuracy, in addition it is a very long and complex procedure.

6.3.5 Velocity estimation

The 2D model was first used to prove that the estimated radial velocity used for COF measurement was reasonable. For this purpose the 2D model was used to find this velocity by plotting the lateral displacement against time and using the equation 6.3:

$$v = \frac{u(t_2)-u(t_1)}{(t_2-t_1)} \qquad 6.3$$

The results is plotted in figure 6.3.6 with values predicted analytically by equation 5.4, in the case of a circular sample with these dimensions: *Ro*=9 mm and *Ho*=4.7 mm and compressed at a velocity: $\frac{dh}{dt}$ = -1.8 mm/min. The numerical and analytical results agree reasonably with each other proving that the estimation of the radial velocity was correct. The two results are not identical though; this can be because of the way in which velocity was calculated from the numerical results; in fact equation 6.3 assumes a constant velocity in the time interval considered (approximately 0.6667 s) and might differ from the analytical solution. Reducing the time interval may lead to better solutions; however for our purpose this estimation was enough and that is why this specific analysis was not considered.

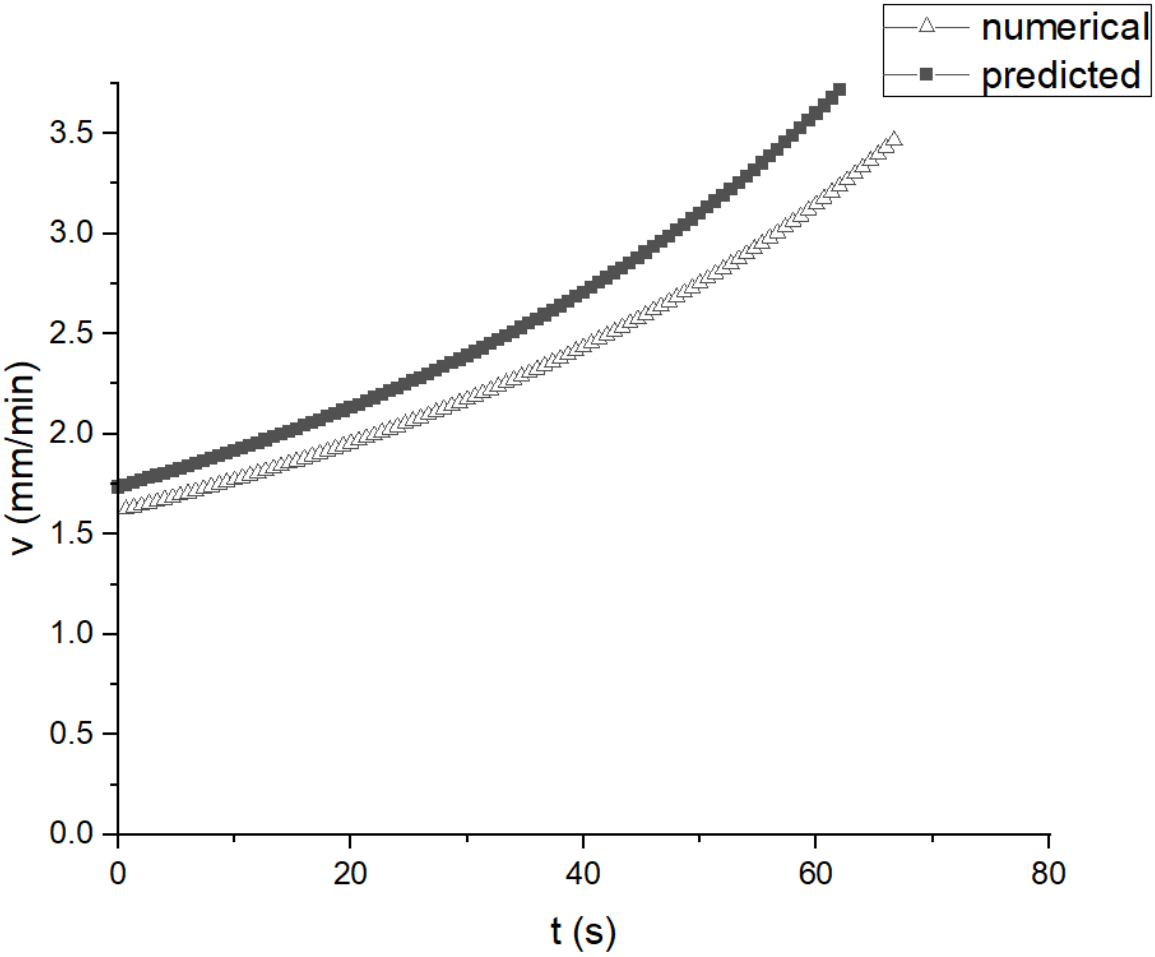

Fig. 6.3-6 Numerical and analytical prediction of radial velocity of the up right corner of a circular specimen during a 66.67 s compression of 40% strain.

6.3.6 Results and comparison with theory and experimental data

Simulations were carried out for different materials, velocities and, in particular, for a wide range of friction coefficients. Finally the variation of the compression behavior with the friction coefficient was studied and compared for different materials and velocities. In figure 6.3.7 an example of set of compression curves for different values of friction is reported.

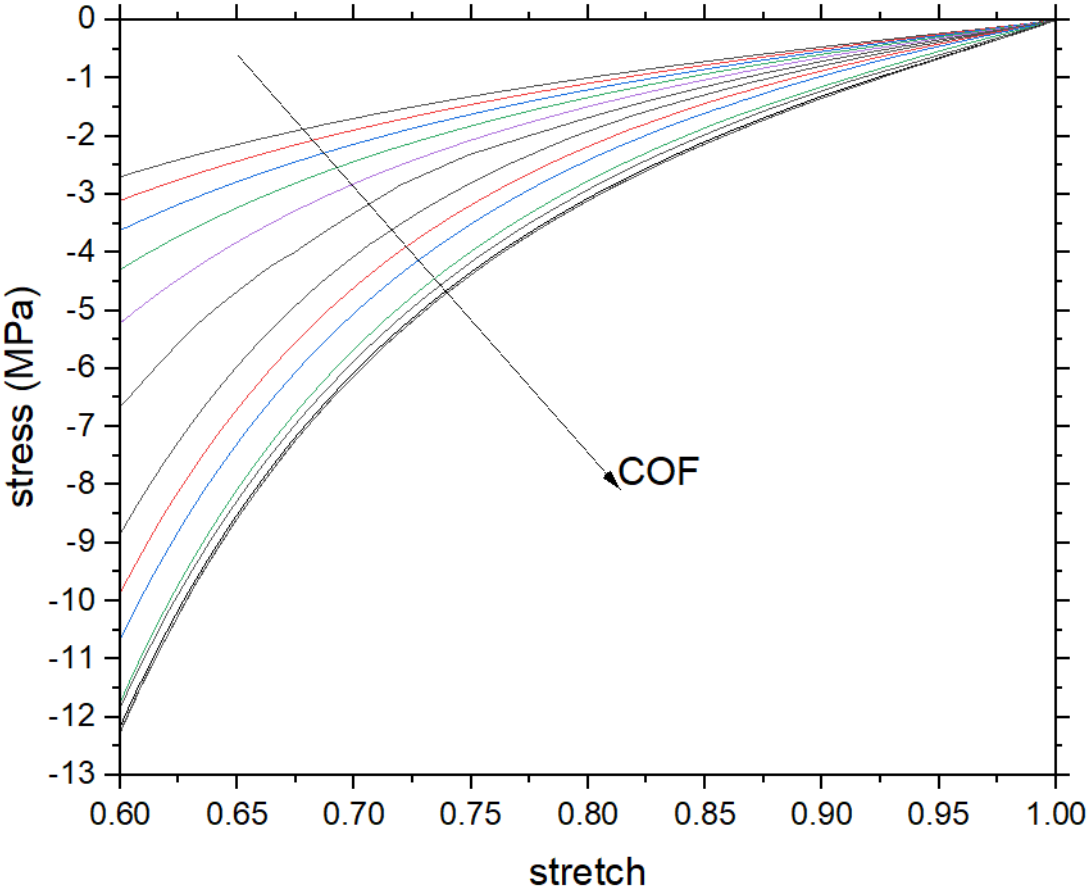

Fig. 6.3-7 Compression curves at different values of COF (from 0 to 2) material B (Mooney-Rivlin) at 0.006 s^{-1}

These curves shows a trend which is quite regular: the curves normalized to the frictionless curve were plotted against the value of COF (figure 6.3.8). To do so every curve was interpolated at a regular intervals of stretch ($\Delta\lambda$=0.0006) and then each value of stress, averaged over the available data at varying stretch, was divided by the corresponding one on the frictionless curve. As we can observe from the graph below (6.3.8) the effect of friction seems to be quite independent on the material and testing velocity. In the lower range of COF (about 0-0.4) the ratio has a strong, linear dependency on friction, then it reaches an asymptotic value of about 0.3 around COF=0.7. The trend obtained was compared with the one extrapolated from the analytical model by Gent et al [29] described above, which was interpolated from graph 4.1.4 for the right aspect ratio (a/h=1.9). The comparison is shown in figure 6.3.9. The curves are quite comparable even if the analytical model suggests a lower initial slope and a higher asymptotic value (0.35) which is reached at higher COF.
Both numerical and analytical results significantly disagree with experimental ones In fact if we assign to the experimental curves the COF measured with the sled for

the same material at the right velocity we see that experiments suggest there is still a strong dependency on friction at high values of COF (>0.6) where numerical and analytical results present an asymptote. In order to show this result curves were normalized to the PTFE curve, whose value of friction depended on material and velocity according to the friction sled results shown above. In this way it was possible to represent the experimental mean ratios and compare them with the analytical and experimental ones. Figure 6.3.10 exemplifies the fact that numerical and analytical results disagree for most materials and velocities. As we can observe the ratio between curves obtained with steel and the PTFE curve is underestimated when the testing velocity is higher than 0.006 s^{-1} (for example material B in fig. 6.3.10) or when material CF is considered. On the contrary it is overestimated for material EI at 0.006 s^{-1}. The ratios between the soap and the PTFE curves, assigning to the soap curve the values of friction measured in PTFE-soap-PTFE condition, were instead always underestimated. In this case the higher is the value of friction assigned to the PTFE curve the worse is the agreement.
The discordance between numerical and experimental results could be due to a numerical problem in the model or to the fact that the real friction value during compression is different from the one measured with the sled. The former possibility will be investigated in the following paragraph.

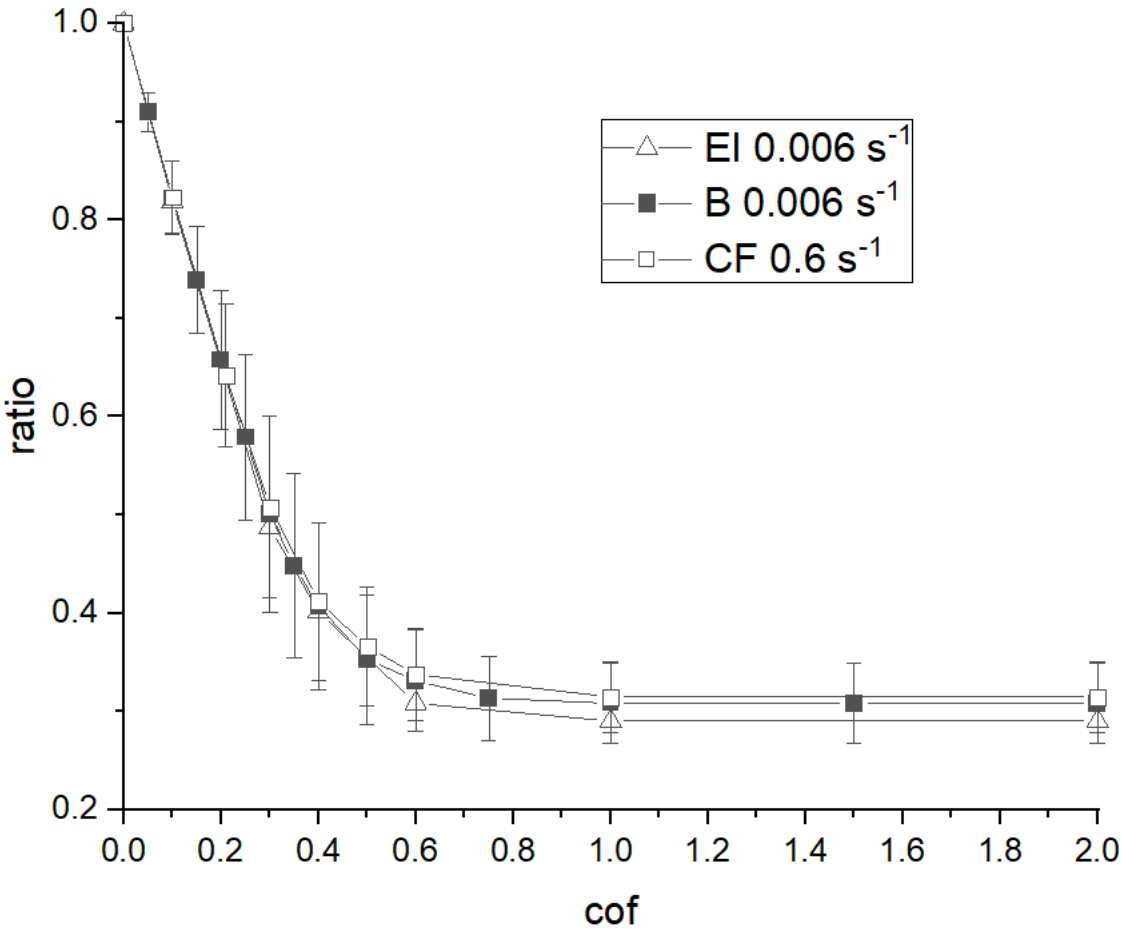

Fig. 6.3-8 Ratio of frictionless curve over curves at different level of friction for different materials and velocities

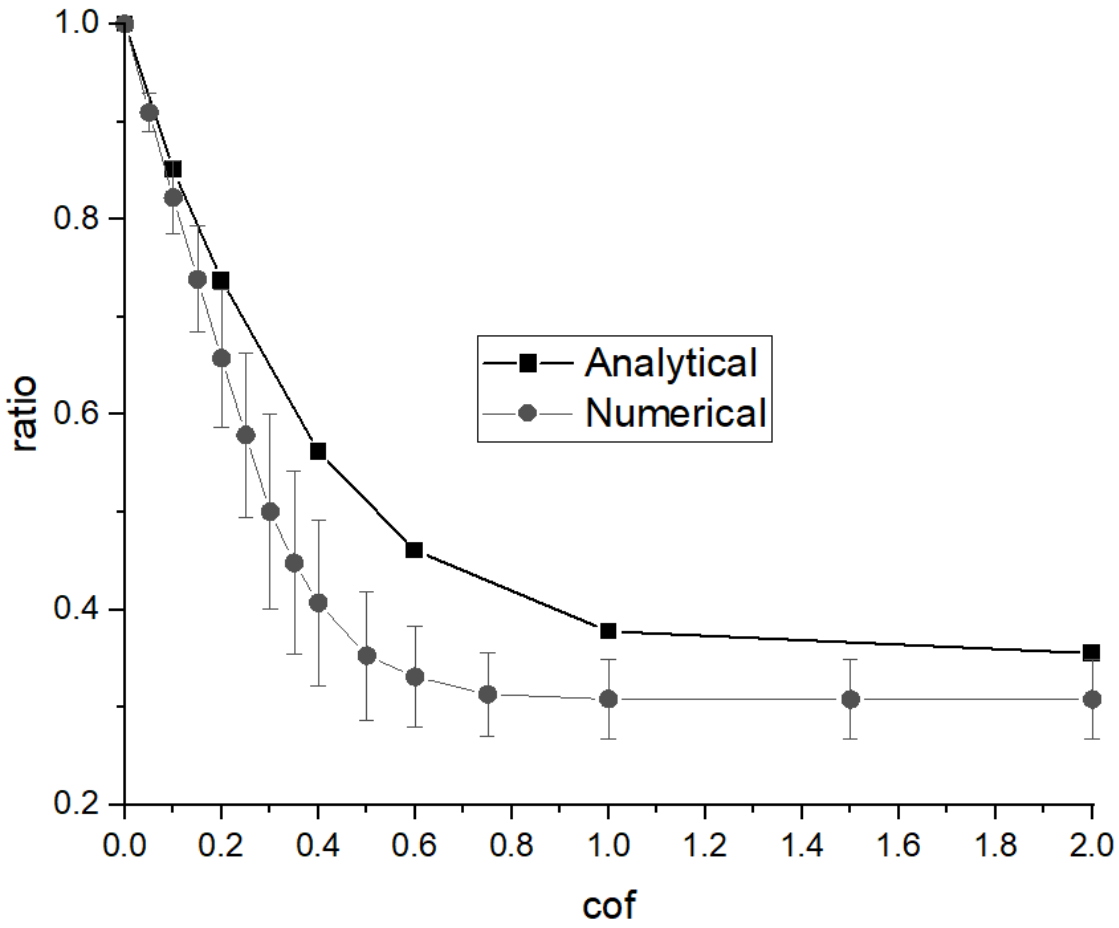

Fig. 6.3-9 Comparison between analytical and numerical results for mean ratio with frictionless curve versus COF

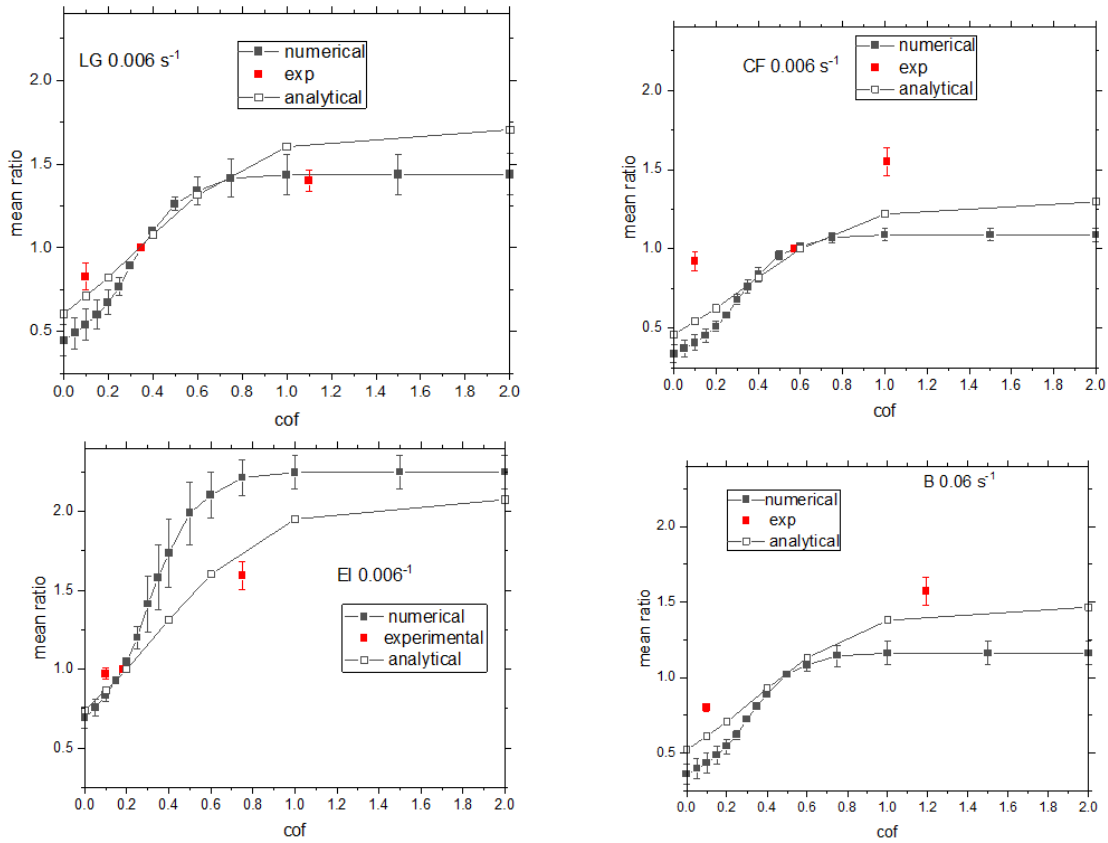

Fig. 6.3-10Experimental, analytical and numerical mean ratios with the PTFE curve for different materials and velocities.

6.3.7 Stress state and contact pressure distribution

The stress state computed with the numerical model agree with the one predicted by the analytical model. Shear stresses S_{12}, provoked by the contact condition, are concentrated at the corners, then decreasing to zero towards the center. The vertical stress S_{22} has instead an opposite trend with a maximum absolute value in the center of the sample and is constant along vertical direction (figures 6.3.11 and 6.3.12). Stress plots change a little when lateral surface roll-over happens (figure 6.3.13). It was noticed that an important edge effect was present at the corners of the sample which unrealistically increased the contact pressure at the very last node of the edge (figure 6.3.15). This effect is well-known also in simple shear problems and it may be due to the rotation of the sample given by the shear stress [22]. It can be observed that the increase in contact pressure is preventing the last node from slipping when the COF is around 0.6, thus putting the sample in a bounded condition when it shouldn't, according to the theory. The same sharp increase in contact pressure in

numerical models is found in some literature works [29], [31] and it is said to disappear when the aspect ratio *a/h* of the sample is increased (figure 6.3.14). It is also important to notice that a very high distortion of the corner elements was always observed in the final results when the COF was high enough to provoke a lateral surface roll over (COF>0.25). This problem was less important when mesh C was adopted, however even in this case a strong stress gradient in the corners elements was recorded (figure 6.3.16).

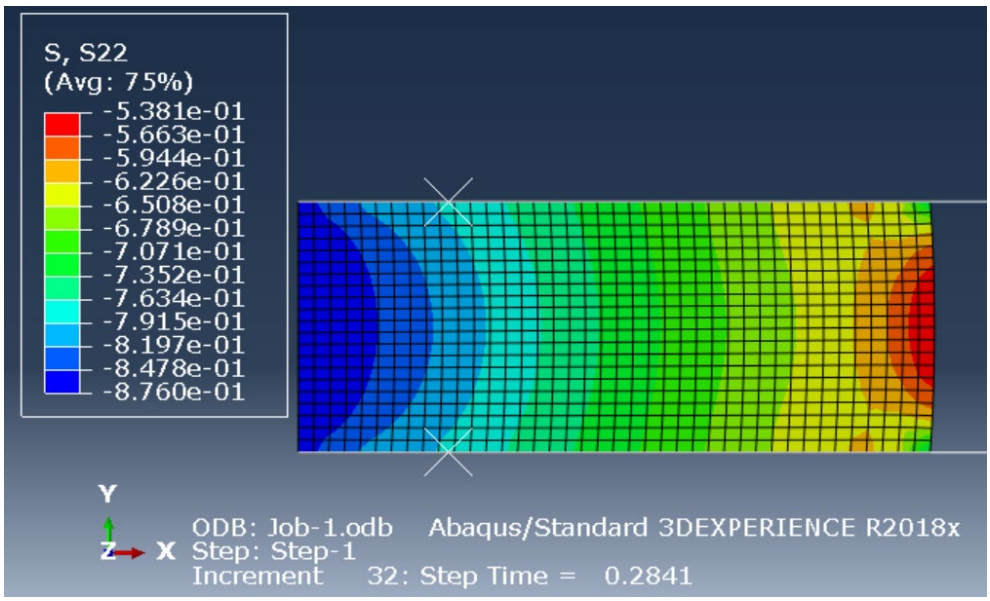

Fig. 6.3-11 Plot of vertical stress (MPa) at a level of about 20% compression deformation (CF Mooney-Rivlin at 0.6 s^{-1})

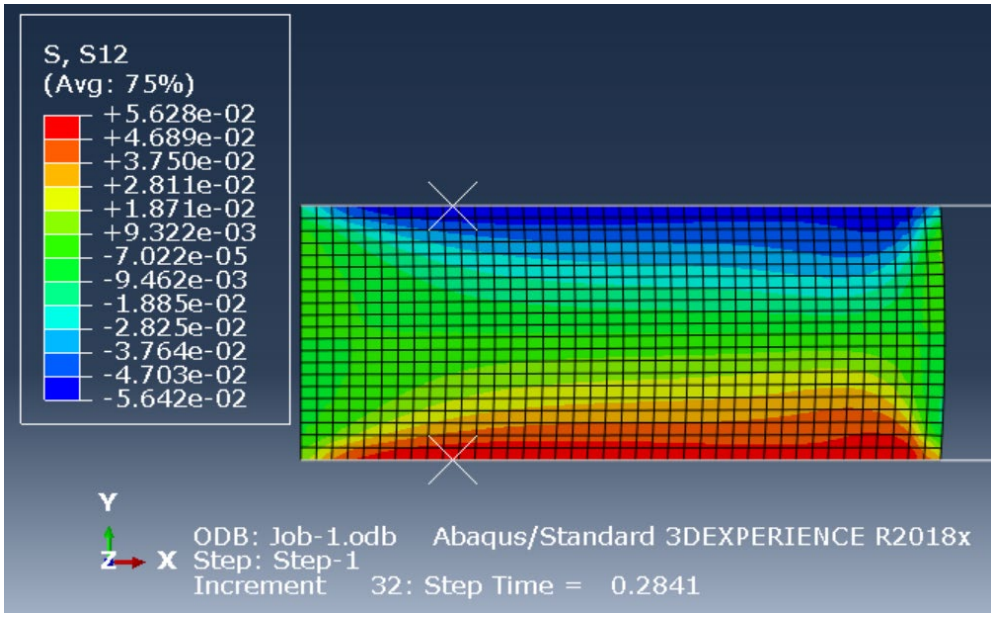

Fig. 6.3-12 Plot of shear stress (MPa) at a level of about 20% compression deformation (CF Mooney-Rivlin at 0.6 s^{-1}),

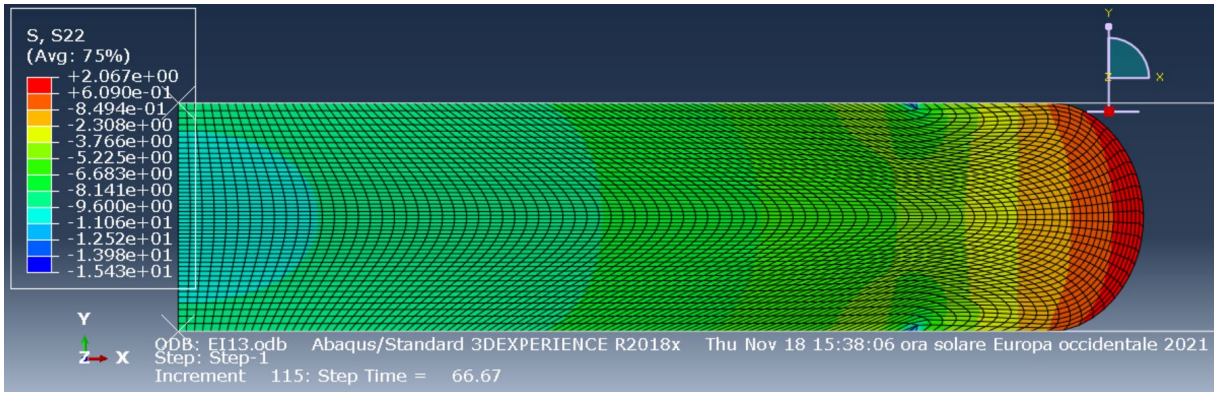

Fig. 6.3-13 Stress plot (MPa) after roll-over at COF=1. Deformation=40% (CF 0.006 s^{-1})

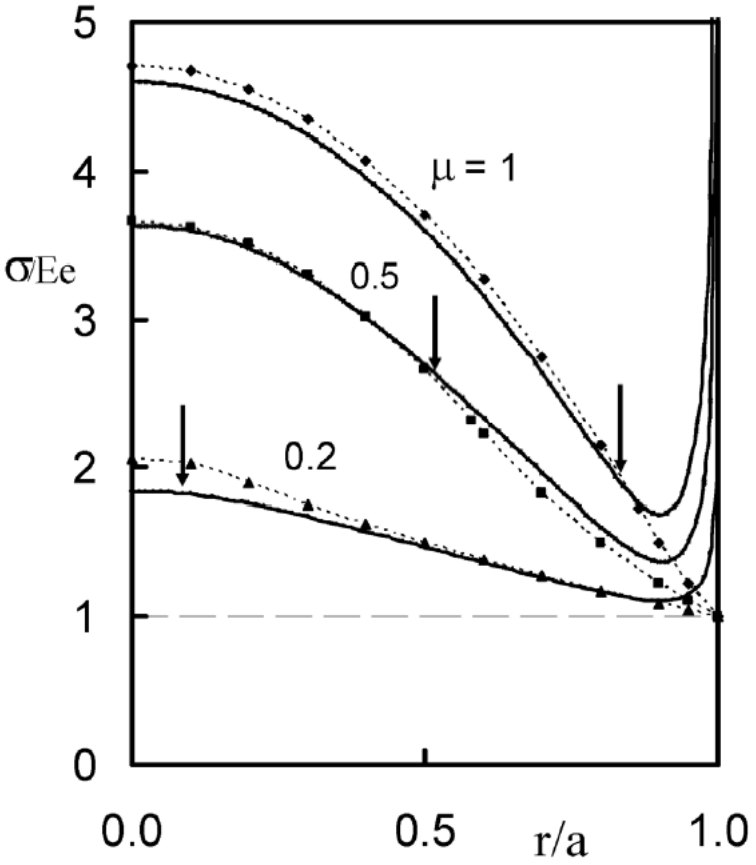

Fig. 6.3-14 Points and broken curves: analytically calculated distributions of reduced compressive stress σ/Ee for disks with aspect ratio a/h = 2, compressed between surfaces with friction coefficient μ. Full curves: FEA results. Vertical arrows indicate radius r1 of non-slip zone. Compression deformation=2%, linear elastic material of E=18 MPa [29]

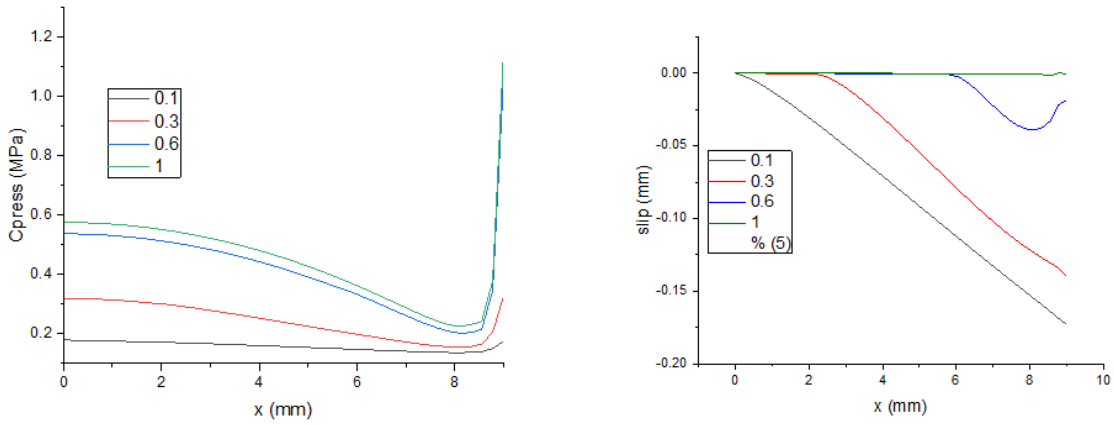

Fig. 6.3-15 Contact pressure versus radial distance (r=9 mm) for different COF on the left. Slip displacement versus radial distance for different COF on the right. Deformation= 10%; CF (Mooney-Rivlin) at 0.6 s^{-1}

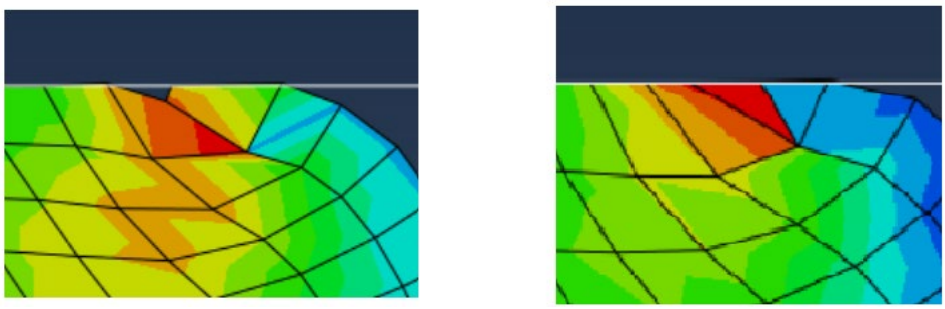

Fig. 6.3-16 Deformation of corners for Mesh A (left) and C (right) during roll over at COF=0.6. CF (Mooney-Rivlin) at 0.6 s^{-1}

6.4 3D Model

6.4.1 Mesh type sensitivity

The sweep and the structured meshes used for the 3D model gives almost the same result for all values of COF investigated as shown by graph 6.4.1

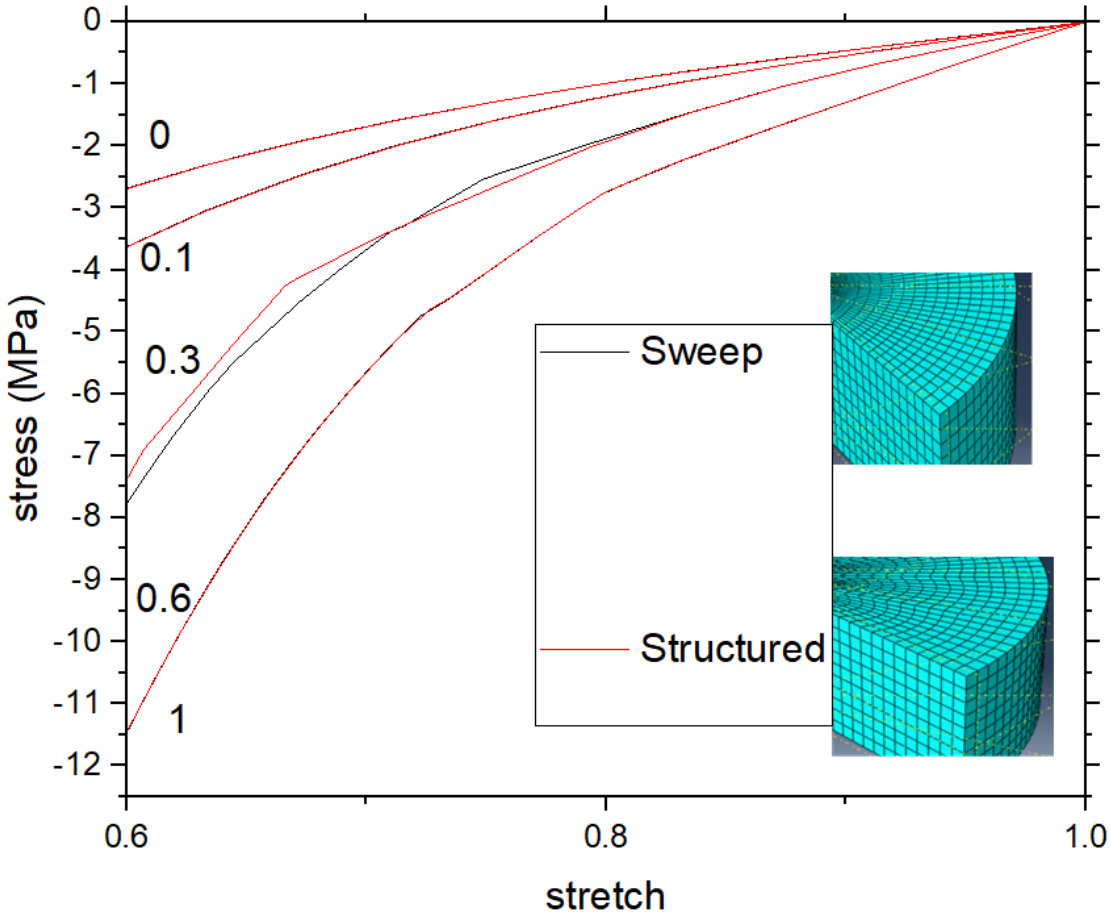

Fig. 6.4-1 Comparison between sweep and structured meshes. B (Mooney-Rivlin) at 0.006 s^{-1}

6.4.2 Mesh size sensitivity

A mesh size sensitivity analysis was conducted to identify the best mesh size. In the graph below the results for three representative COF values 0.1, 0.3 and 0.6 are shown. For low COF a mesh of 0.9 mm resulted fine enough and meant very low computational time. When COF is increased a finer mesh of 0.45mm approximate

size was selected as a good compromise between solution accuracy and computational cost.

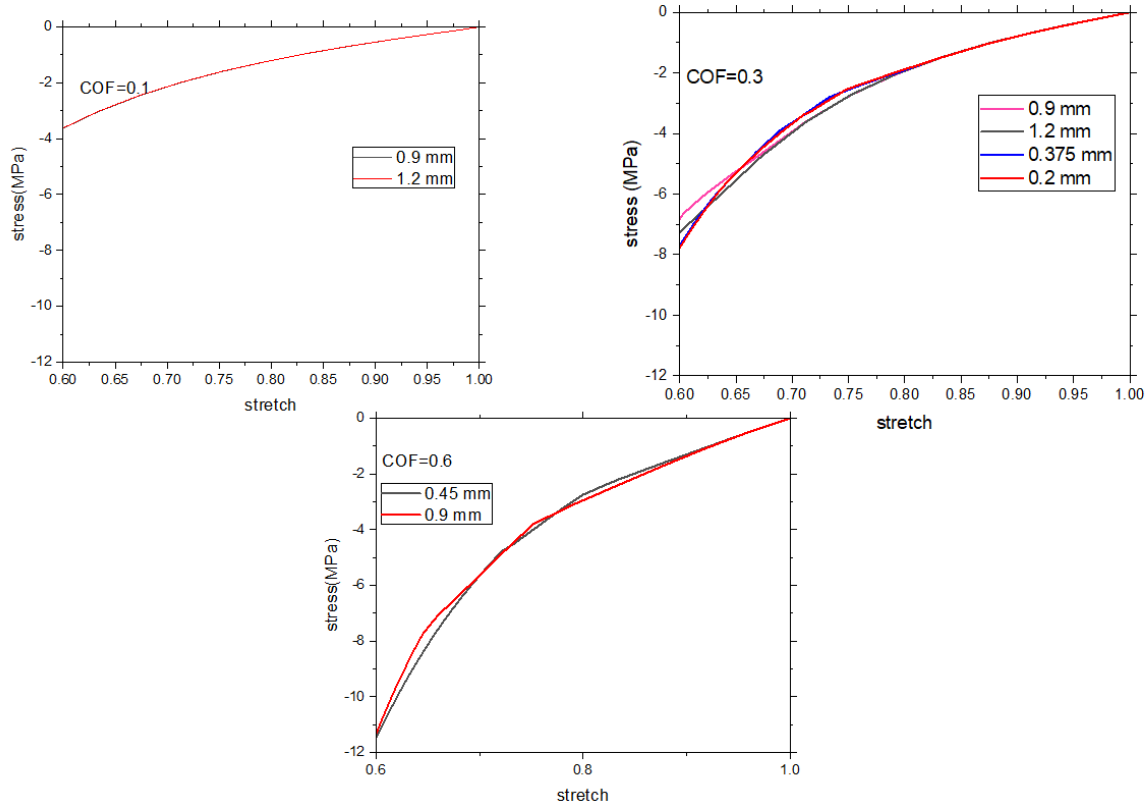

Fig. 6.4-2 Mesh sensitivity for 3D sweep mesh for COF=0.1, 0.3 and 0.6 B (Mooney-Rivlin) at 0.006 s^{-1}

6.4.3 Comparison with 2D results

The curves obtained with the 3D model are consistent with those of the 2D model. For the lowest values of friction (up to 0.2) curves are identical. Curves instead slightly translate toward lower compression stresses for higher values of COF. Anyway the relative distances between curves seem to be the same (figure 6.4.3). The 3D model didn't add any advantage with respect to the 2D one. Furthermore as shown in figure 6.4.3 the 3D model gives less smooth results for COF>0.3. Due to this facts and given the higher computational cost required for the 3D model the use of a 2D axisymmetric model is finally suggested for the simulation of compression tests.

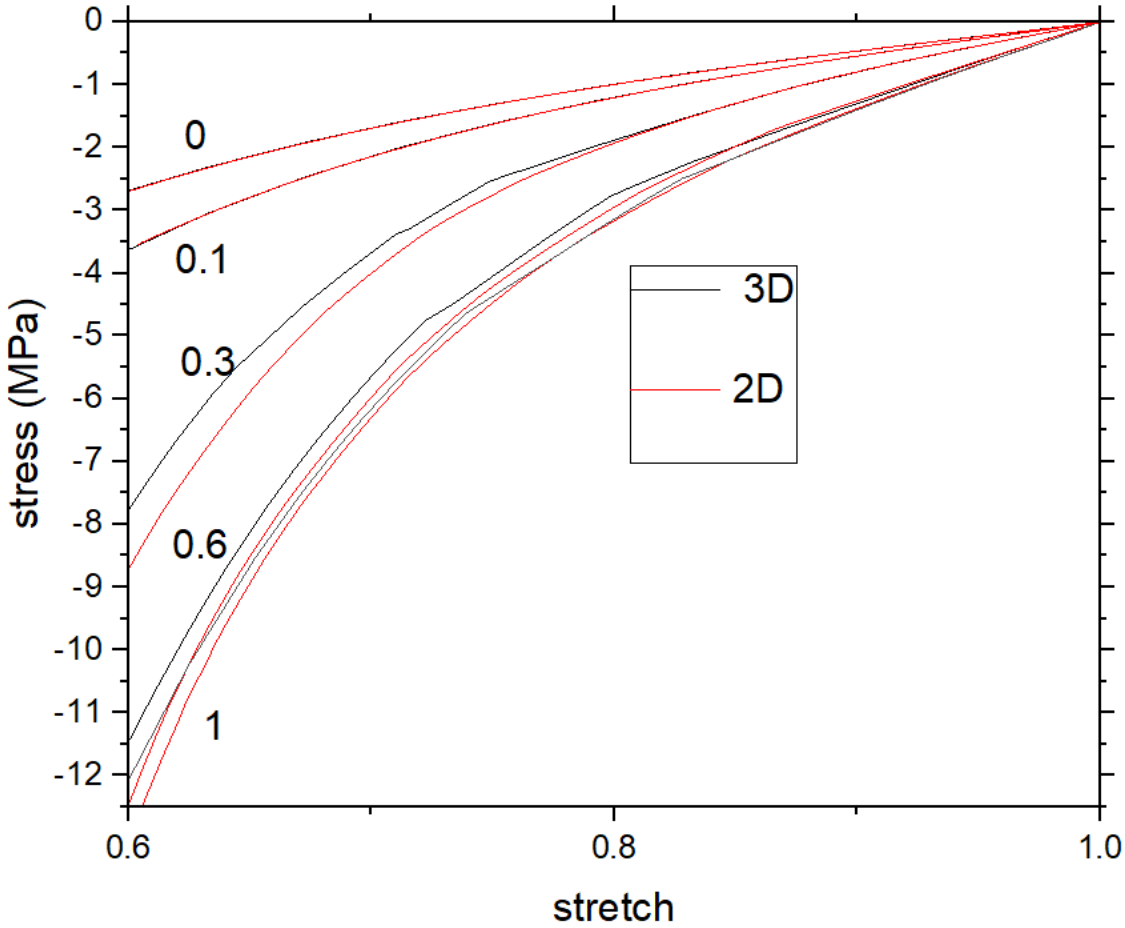

Fig. 6.4-3 Results for 3D and 2D models. B (Mooney-Rivlin) at 0.006 s^{-1})

6.4.4 Stress state and contact pressure distribution

The output plot of the 3D model suggests the same considerations made for the 2D one (figure 6.4.4). Also the same increase in contact pressure is recorded at the maximum radial distance (figure 6.4.5).

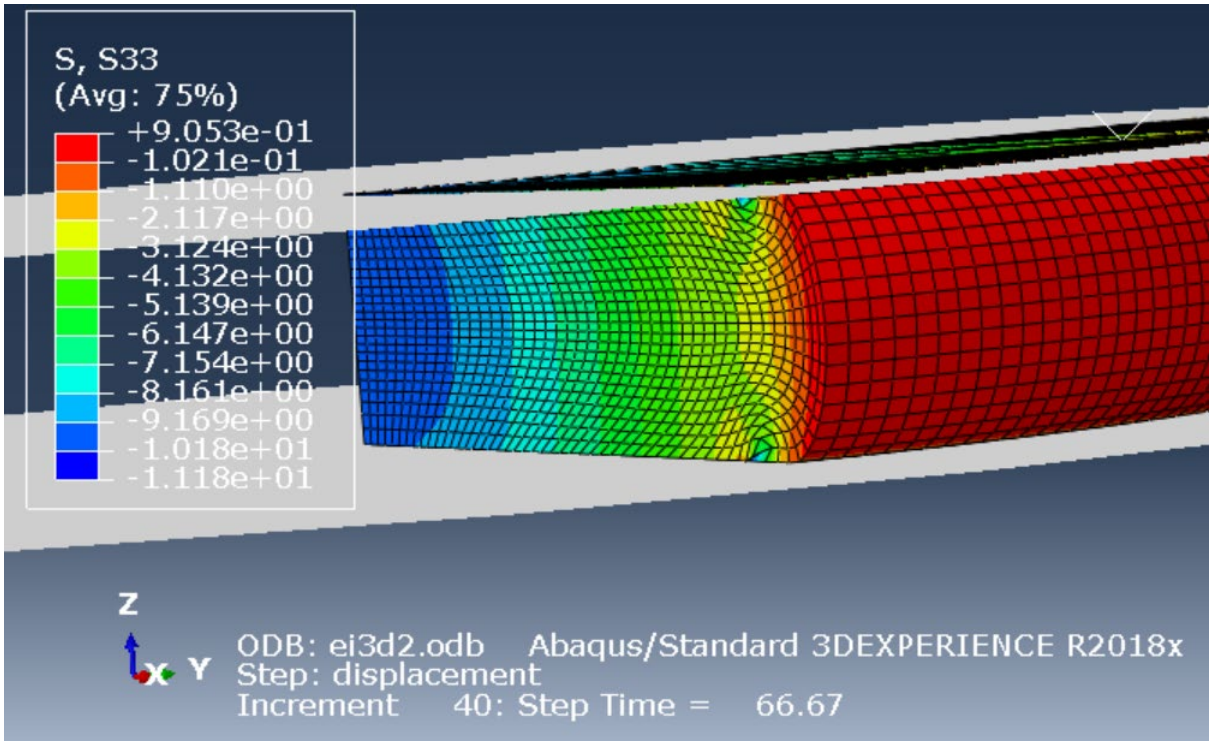

Fig. 6.4-4 Vertical stress (MPa) plot at stretch 0.6 for COF 0.6 3D sweep mesh 0.2 mm, B at 0.006 s^{-1}

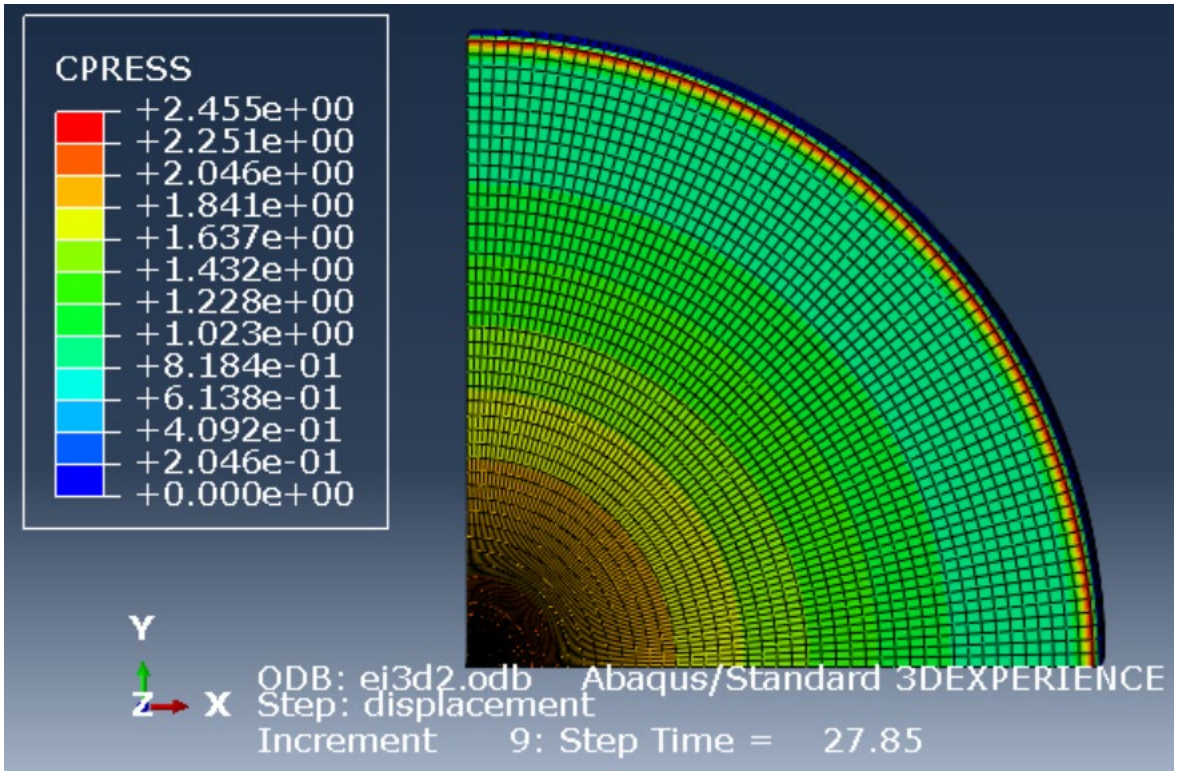

Fig. 6.4-5 Contact pressure (MPa) on the upper face of the sample.

6.5 Sled simulation results

During the simulation of the friction sled horizontal displacement is forced on the weight; the sample, being tied to it, moves sliding against a frictional surface (the substrate). In this way the test looks like a simple shear problem where the stress applied is equal to:

$$\tau = COF * \frac{F_n}{A} \qquad 6.4$$

The aim of the model is to verify that the contact frictional behavior is correctly defined, to identify possible problems in the more complex model of the compression test.

6.5.1 Tangential force

The tangential force predicted by the model obviously matches the expected one. Here results are reported for different values of COF ranging from 0.1 to 2 (figure 6.5.1).

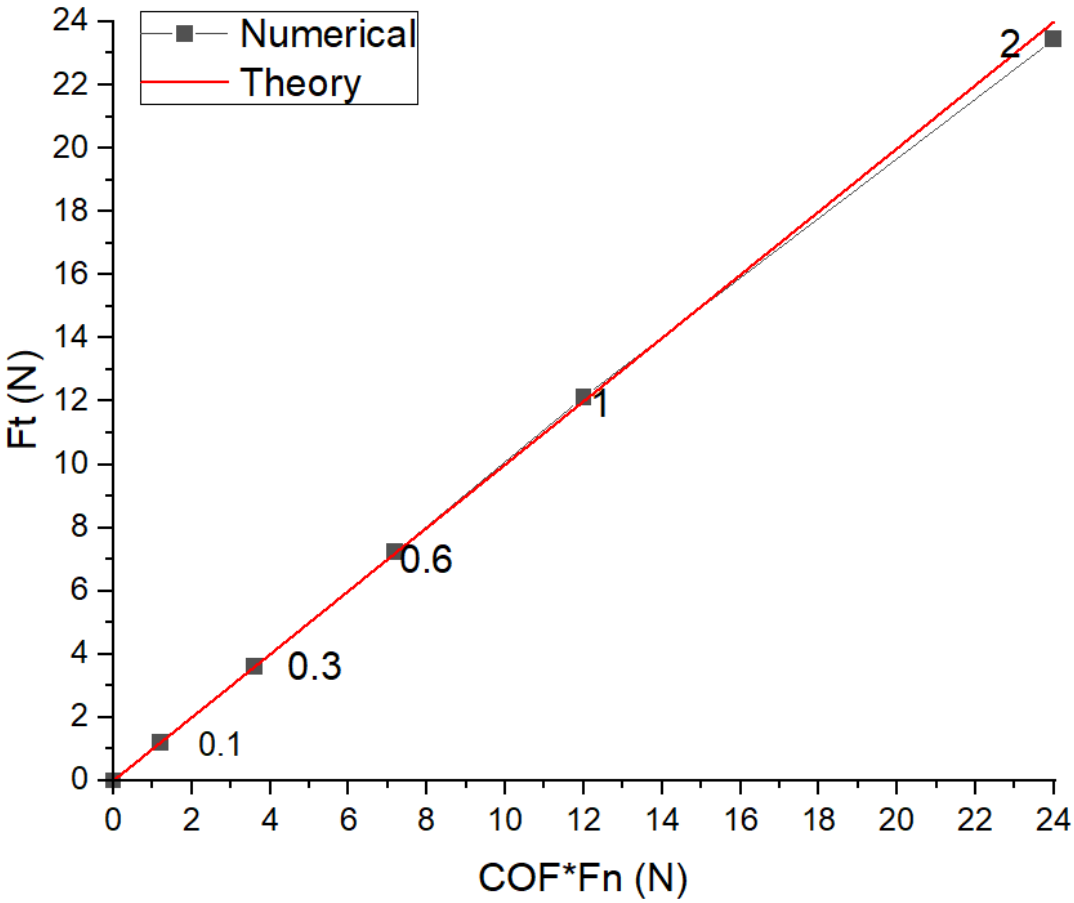

Fig. 6.5-1 Tangential force against COFF_n; COF from 0.1 to 2. Material EI*

As we can observe tangential force is always equal to the normal force multiplied by the COF except for the curve at COF=2 where the force is slightly underestimated. This is probably due to some edge effects that are explained in detail in the next paragraphs.

6.5.2 Investigation on contact behavior

In order to investigate possible problems in the contact behavior of the model different values of normal force were considered, ranging from the 12 N of the sled

test to much higher loads for which the contact pressure is closer to the typical values of the compression tests. Apparently the tangential reaction force is always well described except for being underestimated at higher forces, (figure 6.5.2 shows results for COF=0.6).Having fixed the COF at 0.6, if the force is increased over 10000 N the sample tends to rotate at the edges and penetrates the rigid floor. Furthermore when the normal force is increased over 20000N, the analysis aborts before the sample starts moving. If the shell thickness is decreased, or the COF is increased, this happens for much lower forces; as shown in figure 6.5.3, a 500 N normal force is enough to give this effects if shell thickness is decreased to 1 mm. Despite this the central part of the specimen is always well described and the deformations and stresses in it are consistent with those expected from the theory. The contact pressure against the substrate shows the same edge effect recorded for the axisymmetric model, with a sharp increase at the corners for all normal forces (figure 6.5.4). The edge effect seems to disappear only when the shell thickness is increased drastically (figure 6.5.5). In addition the influence of the element type on the results was considered. The element types tested were plane stress elements (CPS4R) and plane strain ones (CPE4RH). A difference between these results were recorded both in the contact pressure trend along path and in the plot of the shear stresses. In particular CPE4RH elements gave less homogeneous results whereas the CPS4R ones showed results quite constant along the length of the sample (figures 6.5.6. and 6.5.7).

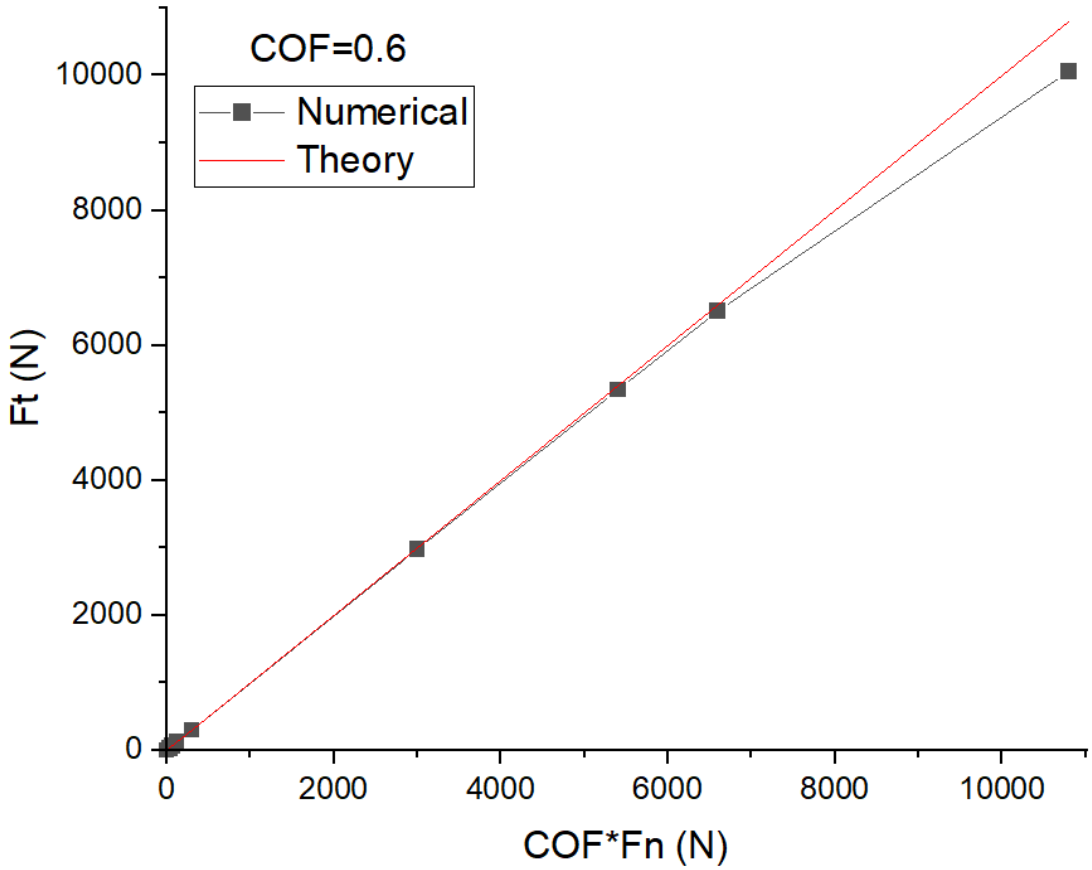

Fig. 6.5-2 Tangential reaction force versus COF(F_n) for COF=0.6, for different normal forces, Material EI*

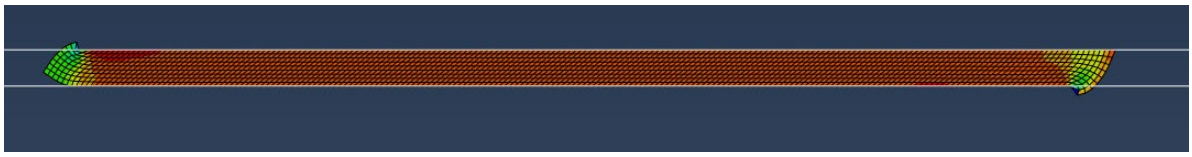

Fig. 6.5-3 Shear stress output plot for Fn=500N shell thickness=1. Material EI

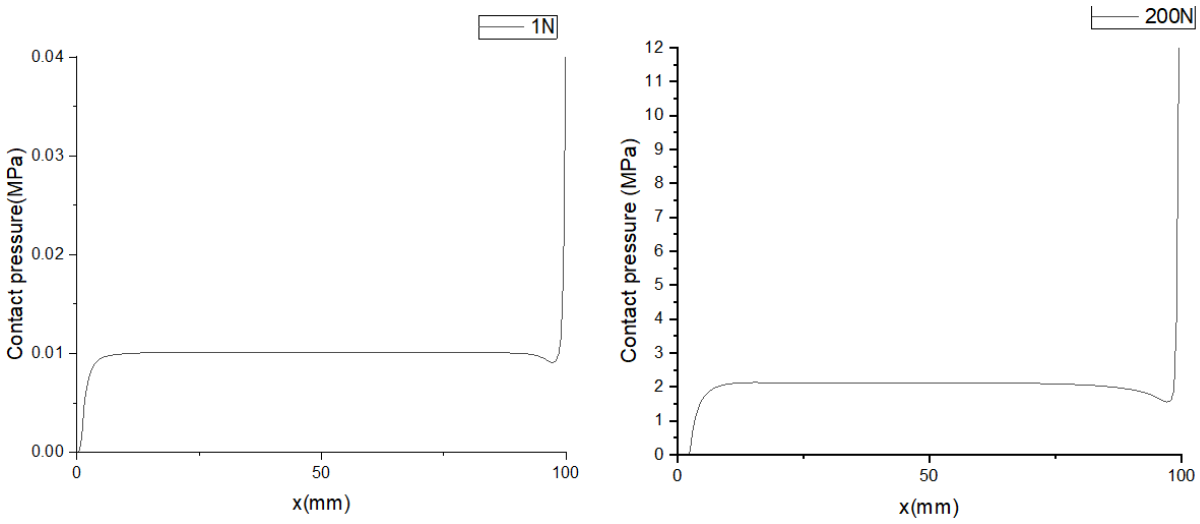

Fig. 6.5-4 Contact pressure along the sample edge in contact with the substrate for F_n=1N and F_n=200N, Material EI

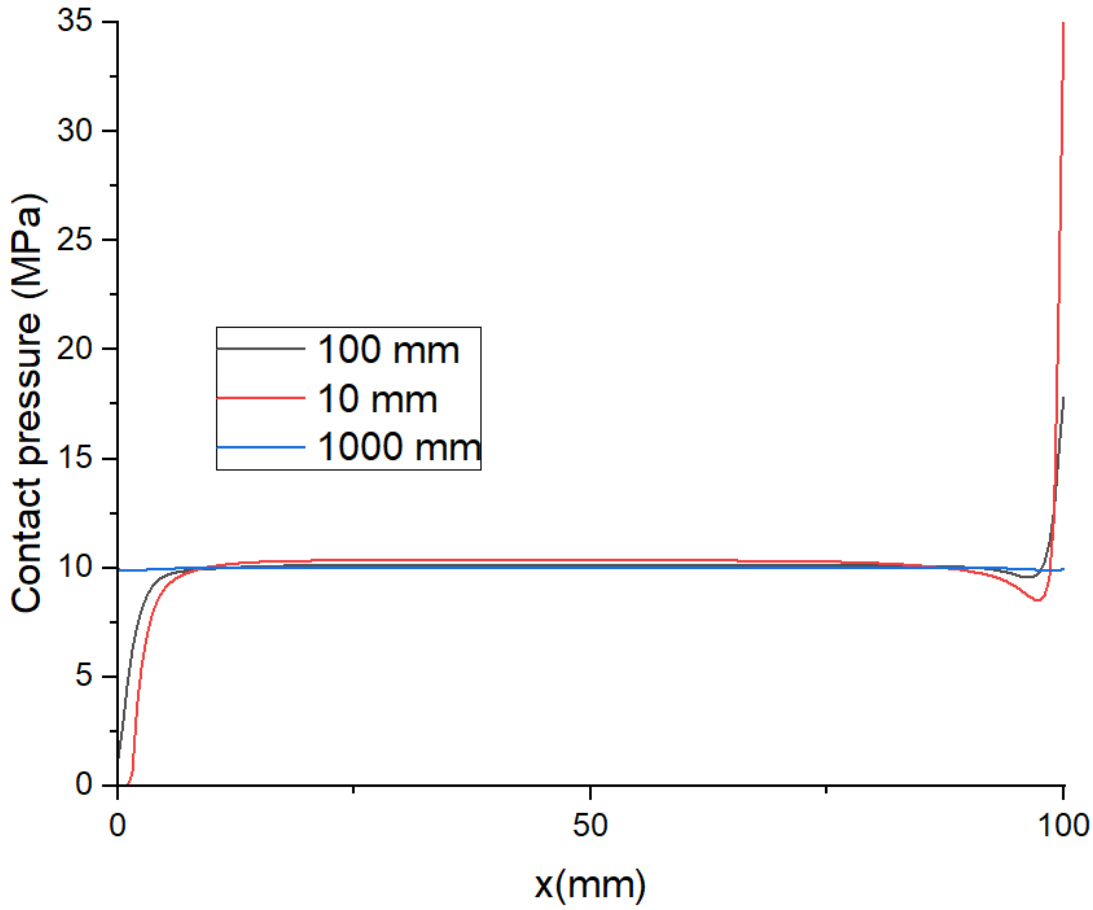

Fig. 6.5-5 Dependence of contact pressure along path (edge between sample and substrate) for different shell thicknesses applied. F_n= 1000N (Material EI)

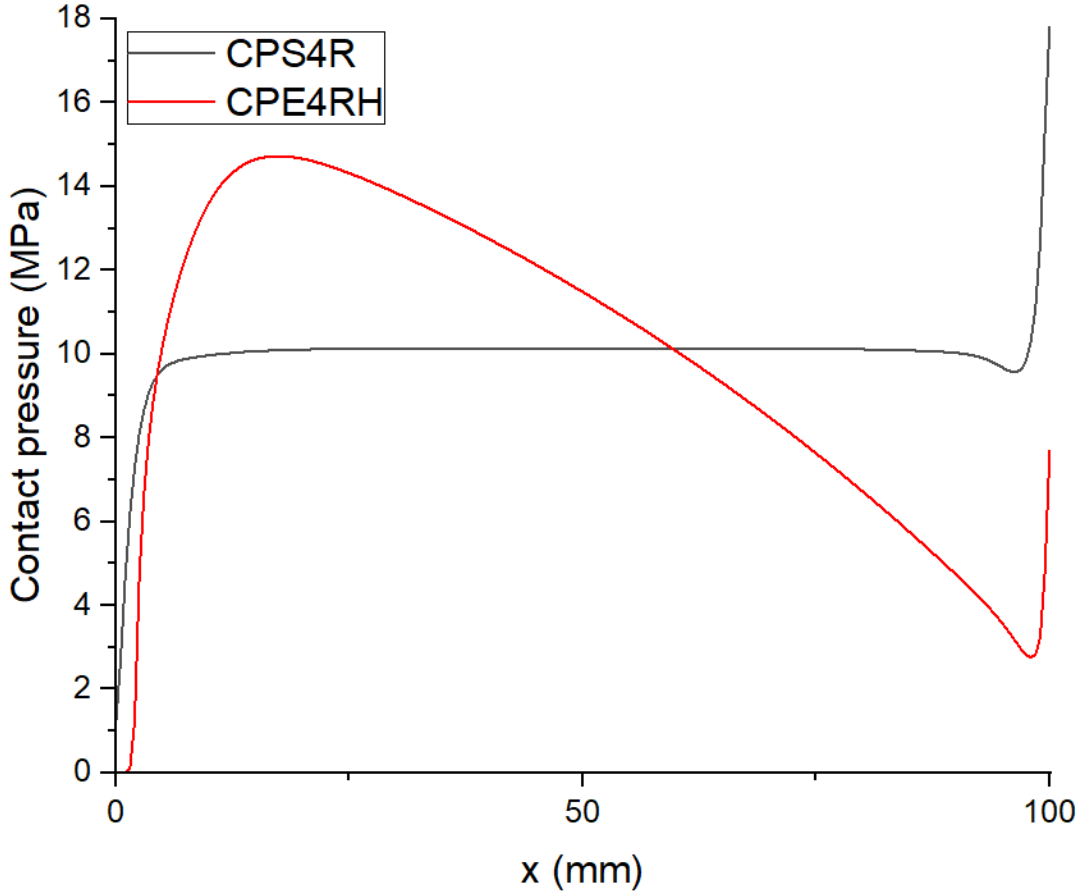

Fig. 6.5-6 Influence of element type on contact pressure trend along path. F_n=1000N Material EI

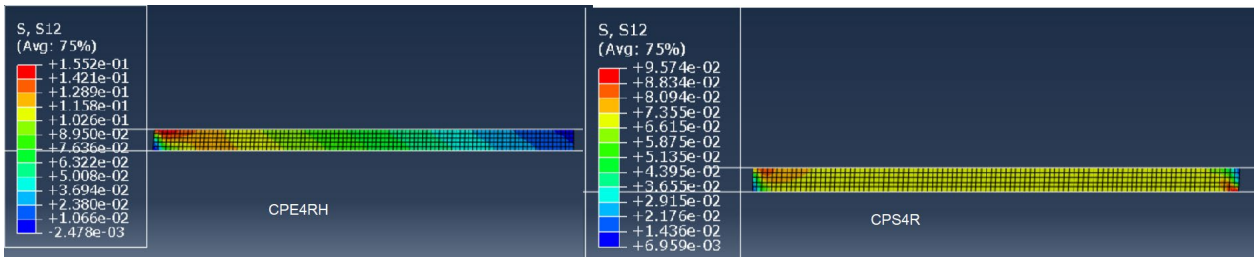

Fig. 6.5-7 Stress plot (MPa): comparison between CPE4RH and CPS4R elements.

6.5.3 Shear stress and strain

Shear stress and strain predicted for the case of 12 N normal force are shown. The shear stress is constant in time, as the tangential force and is predicted by equation 6.3, where the area is equal to the length (100mm) multiplied by 100 mm (shell thickness).Shear stresses are shown in figure 6.5.8 for different values of COF. The shear strain instead increases with time due to viscoelasticity of the material. In fact even if the stress is constant an increase in shear compliance should be recorded. Despite the fact that some edge effects are present the magnitudes considered, both the reaction forces and the strains in the sample, are well predicted by the model. We can compare the strain results with the theoretical results predicted knowing the initial shear modulus from the models described in chapter 3. In this case we see a good agreement between the numerical and theoretical value of strain at *t=0s* for COF values lower than 2 (figure 6.5.9).

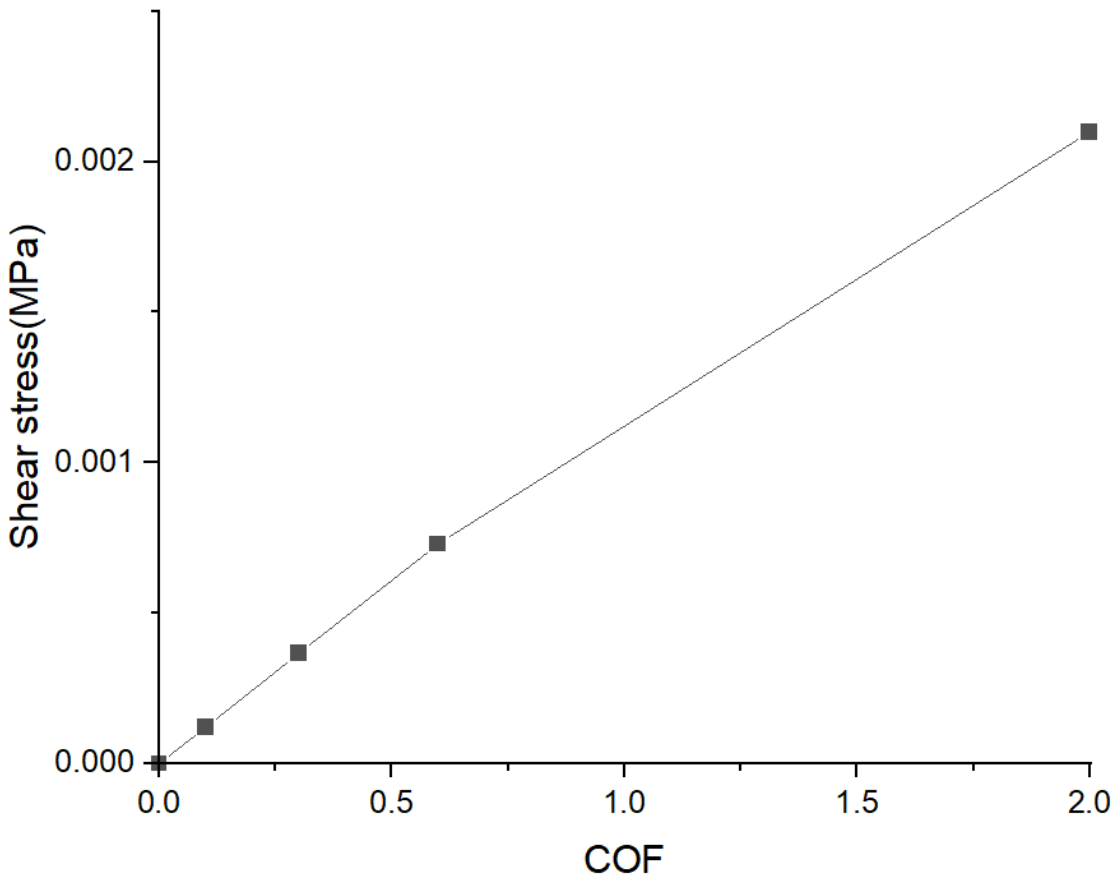

Fig. 6.5-8 Shear stress in sample versus COF. Material EI

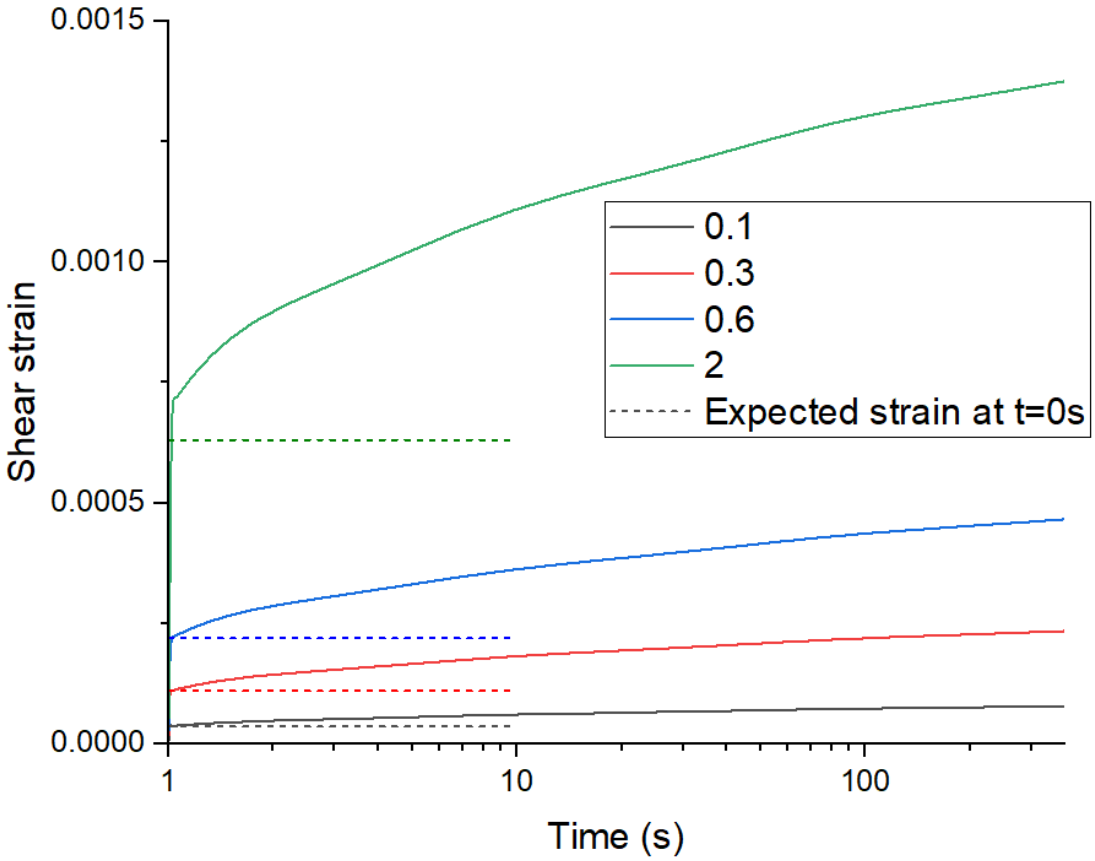

Fig. 6.5-9 Shear strain in sample against time (log scale) from numerical model and theoretical values of strain at t=0s (dashed lines), Material EI

6.5.4 Stress state analysis

The edge effects described above can be seen also in the resulting output plot. In principle one should expect to have a homogeneous shear stress in the whole sample. Actually the integral result of the reaction force is not much affected by these effects and the shear stresses and strains doesn't vary much along the specimen except for the zone very close to the corners (figure 6.5.10). The edge effect of the stresses and strains is higher when the sample is subjected to higher shear, therefore when the COF and/or normal force are increased. This is shown in figure 6.5.11 where we can observe an increase in the strain gradients acting on the corner.

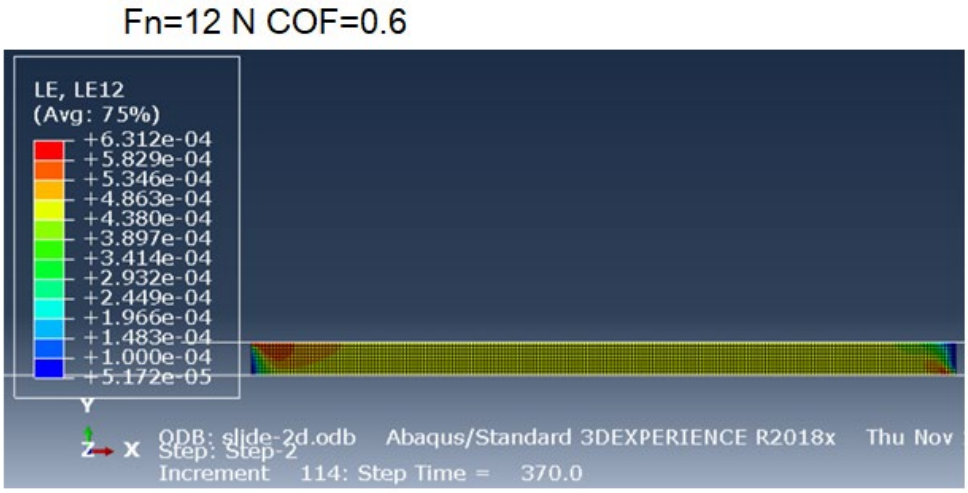

Fig. 6.5-10 Shear strain plot for COF 0.6 material at the end of step 2(Plane stress, Fn=12N) (EI)

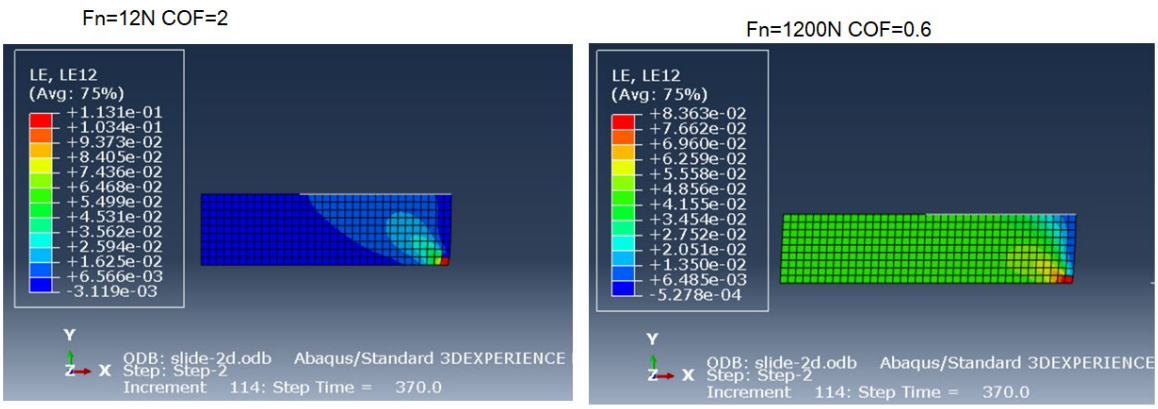

Fig. 6.5-11 shear strain plot (right edge of the sample): edge effect on specimen corner when COF is inceased(left) and when F_n is increased(right) (EI)

6.5.5 Mesh sensitivity

A mesh sensitivity analysis was carried out in order to choose the right mesh size. Meshes of 1, 0.5 and 0.25 mm were tested at this purpose. Both the tangential force and the logarithmic strain history didn't result to be influenced by mesh size in this range of dimensions. That is why a mesh size of 1 mm can be chosen.

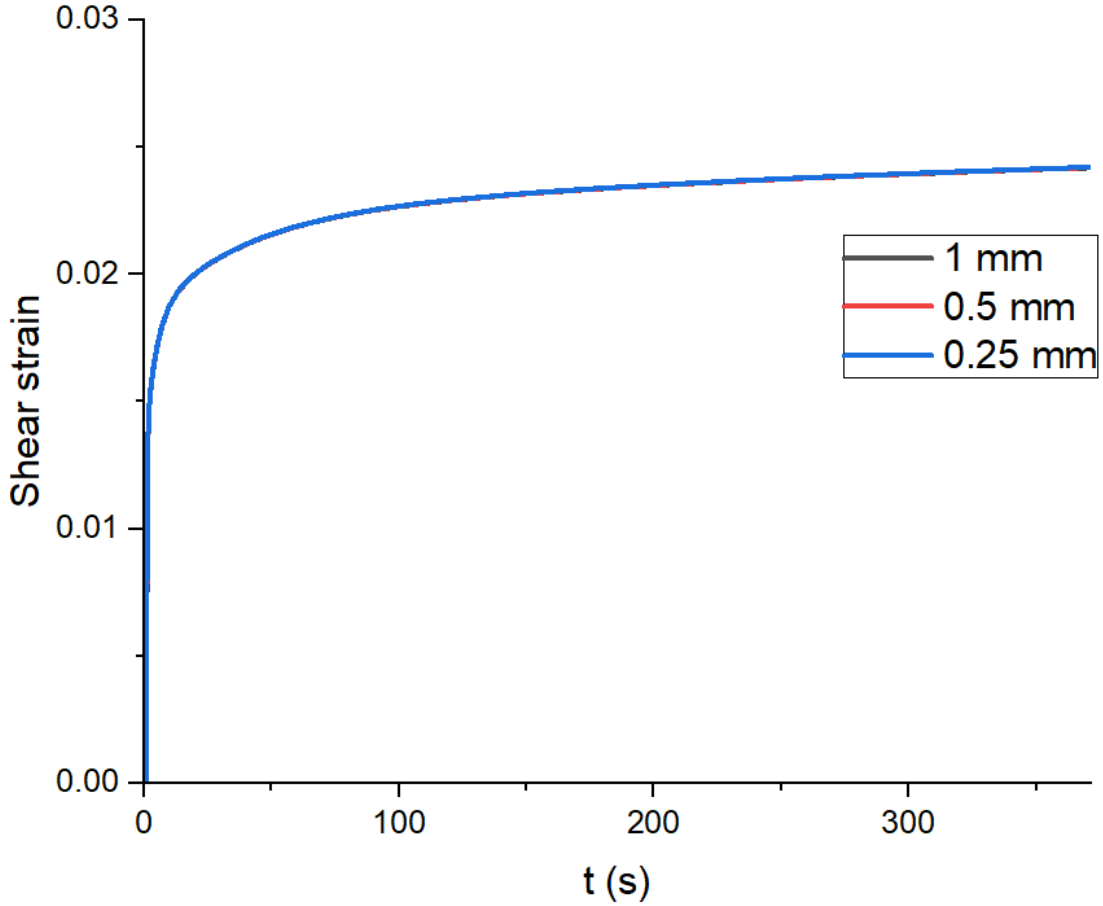

Fig. 6.5-12 Shear strain history for different mesh size. Material (EI)

6.5.6 Sled 3D results

Results found with the 3D model doesn't add much to the one obtained with the 2D sled. The main difference is in the stress and strain plots of the sample. In fact these magnitudes are not equally distributed in the sample and seems to change from plane to plane (figure 6.5.13). However the values are perfectly in agreement with the ones expected that, also in this case, are calculated on an area corresponding to

A=100X100=10000 mm^2. The tangential force was well described also in this case up to loads of about 60000 N, value over which no convergence is reached. The same edge effects were observed, in particular in the half width of the specimen as shown in figure 6.5.14.The mesh chosen had an approximate size of 1mm.

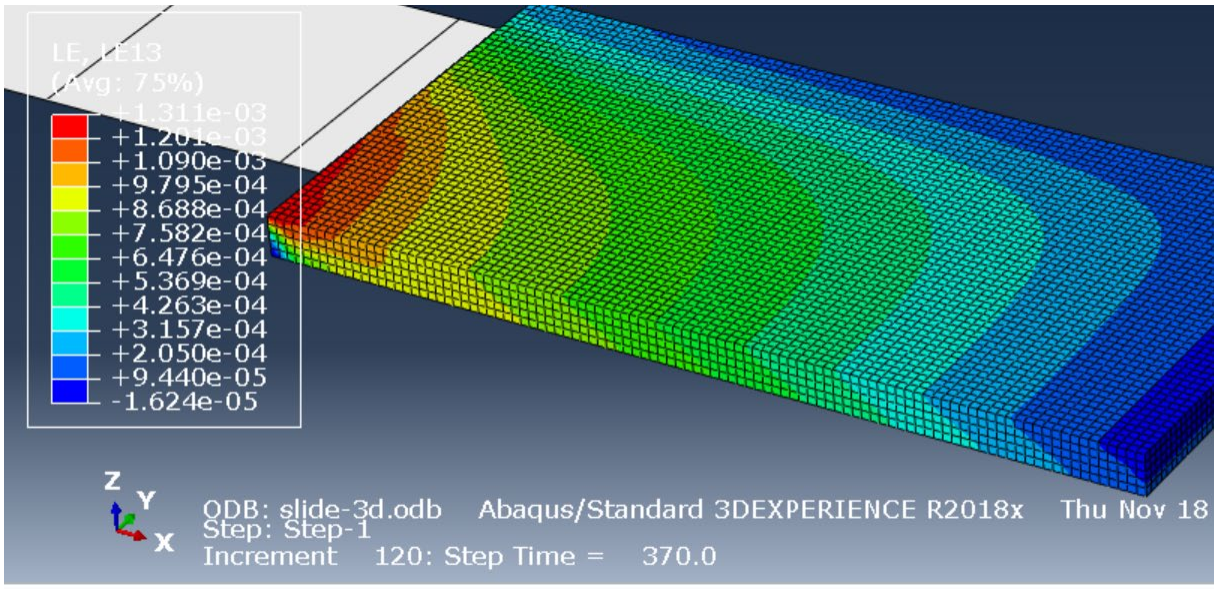

Fig. 6.5-13 Shear strain in sample, COF=0.6, half width XZ plane cut view (F_n=12N) (material EI)

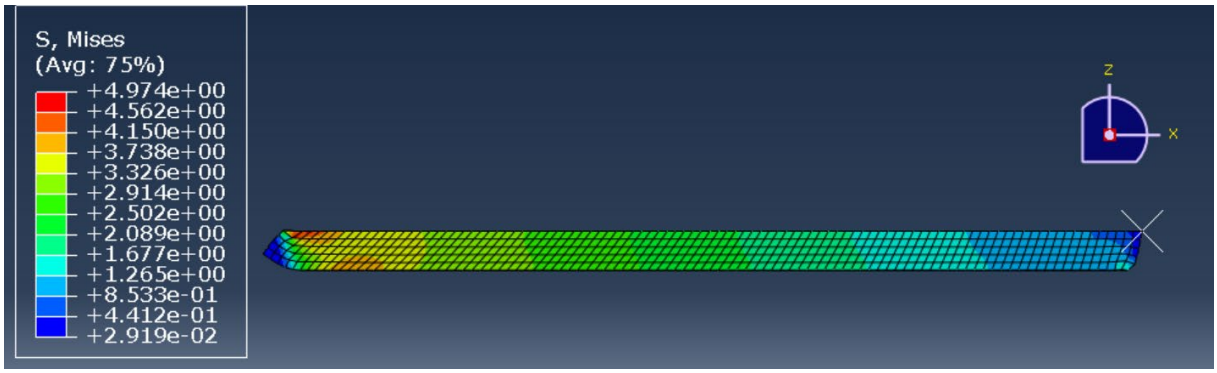

Fig. 6.5-14 Mises plot (MPa), half width XZ plane cut view, F_n=60000N, COF=1

6.6 Fitting of new parameters

Following the fitting procedure described in 5.7 new parameters for the four materials have been extrapolated using the curves obtained with soap lubrication. For this fitting the simpler case of Mooney-Rivlin model was chosen for all materials

and the results were then compared with the one obtained in [19] for the same hyperelastic model. Furthermore, using the friction coefficients measured with the sled and the numerical model, experimental curves were rescaled to obtain virtual frictionless ones and the fitting was repeated again on these new curves. The τ_i coefficients were again fixed as: 0.3s, 3s, 30s and 300 s.

Results of the fitting of new experimental curves are shown in table 6.1 in comparison with the ones obtained in [19]. As expected new coefficients show a less stiff hyperelastic component. The comparison between the hyperelastic coefficients is shown in graph 6.6.1 for C_{10}, coefficients C_{01} resulted again to be equal to zero in all cases as it was observed in [19]; in fact, even in this case, the materials could be well described by using the simpler Neo-Hookean hyperelastic model. As already stated in chapter 3, we can remind that for this model the C_{10} coefficient is directly proportional to the elastic modulus (equation 3.22) and, as a consequence, is suitable to compare the materials stiffness.

Notably, the viscoelastic function which was expected to be independent on friction, changed as well. Figure 6.6.2 plots all the *g(t)* functions up to the time $t = \tau_4 = 300s$. We observe that the newly found viscoelastic function is always decaying more slowly and present a higher asymptotic value. A hypothesis could be that with the new lubrication system curves at higher rate were performed at a level of friction closer to the ones at slower rate, contrarily on what happened with the PTFE lubrication. It was already observed in fact in paragraph 6.1 that the influence of soap on the compression curves was more and more visible as the velocity of the test was increased. The different variation of curves at different velocity may have affected the coefficients which describes the time dependency of the materials, since the loading part influences them as well.

New parameters obtained were finally validated with numerical simulations results compared with experimental curves (figure 6.6.3 and 6.6.4); the agreement seems good. These results represent a reliable set of coefficients able to describe the materials more accurately with respect to the previous one. The tested PTFE-soap-PTFE lubrication system resulted able to decrease significantly the influence of friction in compression tests.

Material (lubrication)	C_{10} (MPa)	C_{01}(MPa)	g_1	g_2	g_3	g_4
B (PTFE)	0.96	0	0.10	0.17	0.18	0.04
B (soap)	0.81	0	0.19	0.059	0.14	0.060
EI (PTFE)	1.6	0	0.20	0.19	0.10	0.057
EI (soap)	1.3	0	0.091	0.14	0.19	0.066
CF (PTFE)	0.60	0	0.10	0.33	0.050	0.060
CF (soap)	0.44	0	0.24	0	0.24	0.050
LG (PTFE)	0.87	0	0.15	0.25	0.067	0.047
LG (soap)	0.56	0	0.089	0.11	0.096	0.24

Table 6.1 Fitting of parameters on experimental curves obtained with soap lubricated PTFE interfaces (grey) and old coefficients obtained with just PTFE [19] (white)

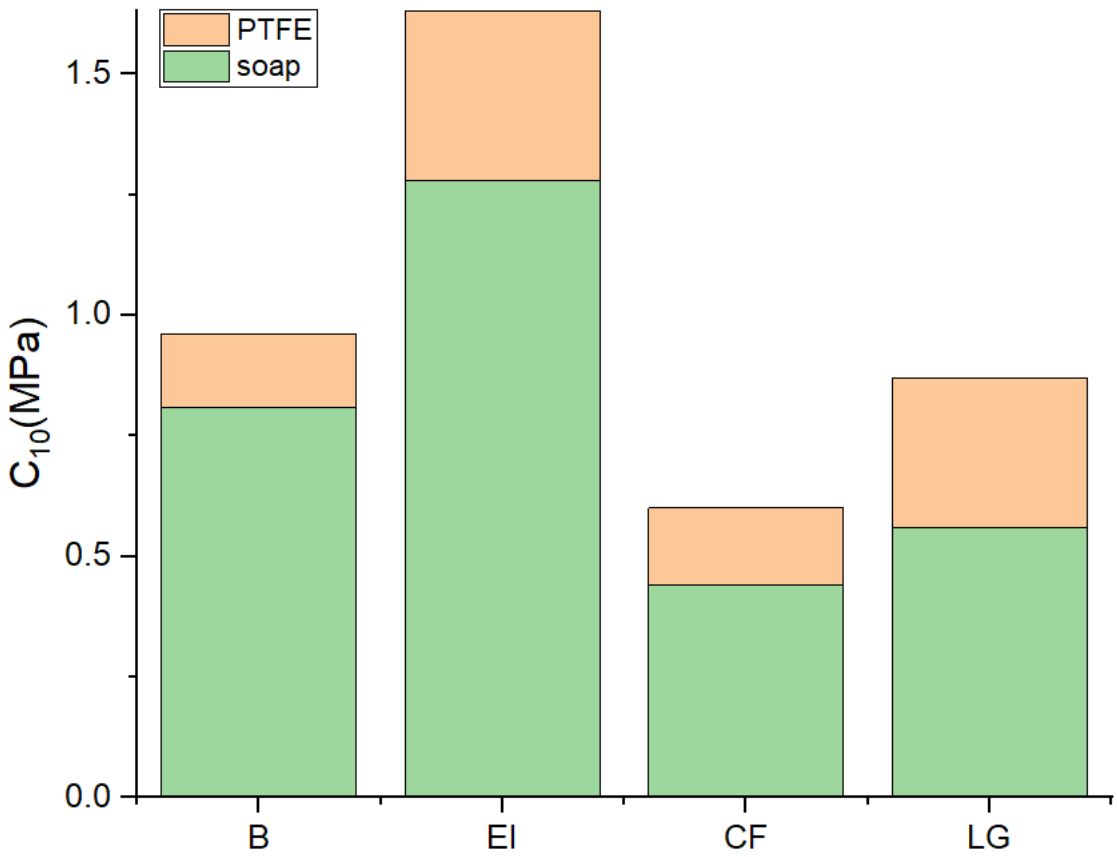

Fig. 6.6-1 Comparison between coefficients obtained with PTFE and the one obtained with soap

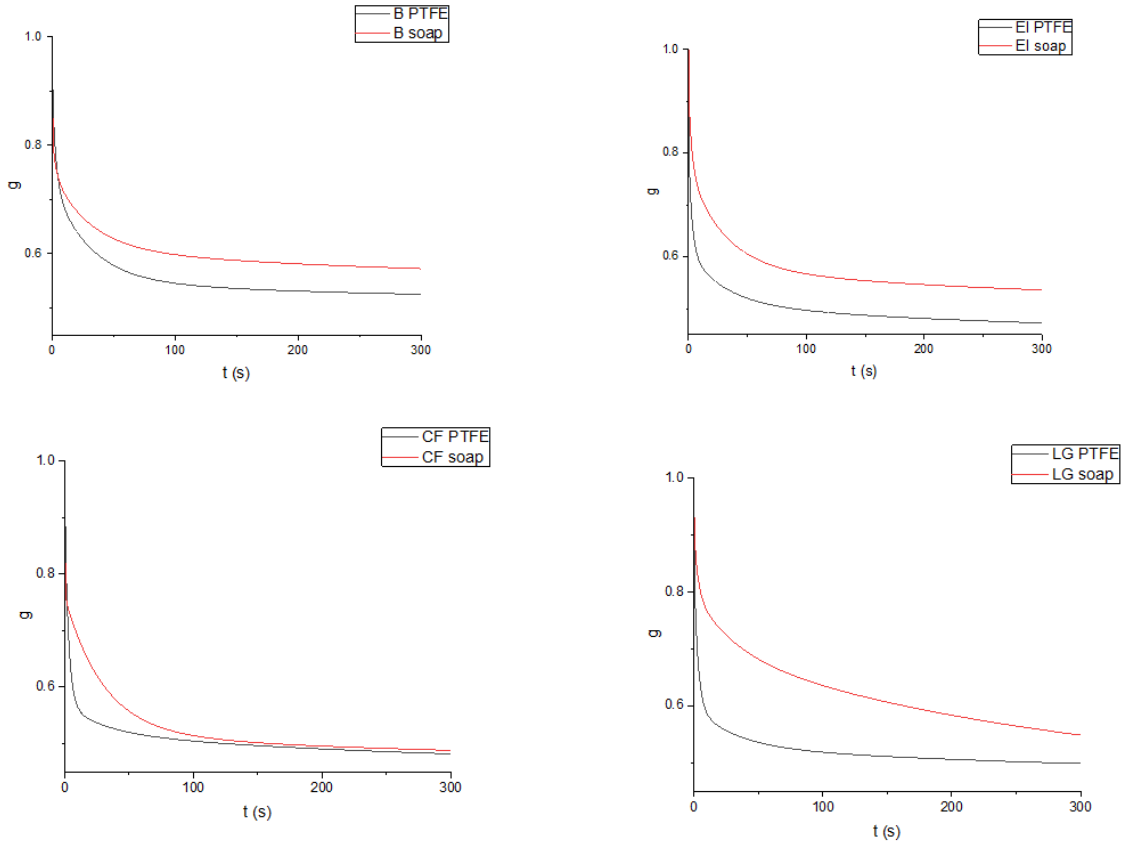

Fig. 6.6-2 Comparison between viscoelastic functions obtained with PTFE [19] and the one obtained with soap

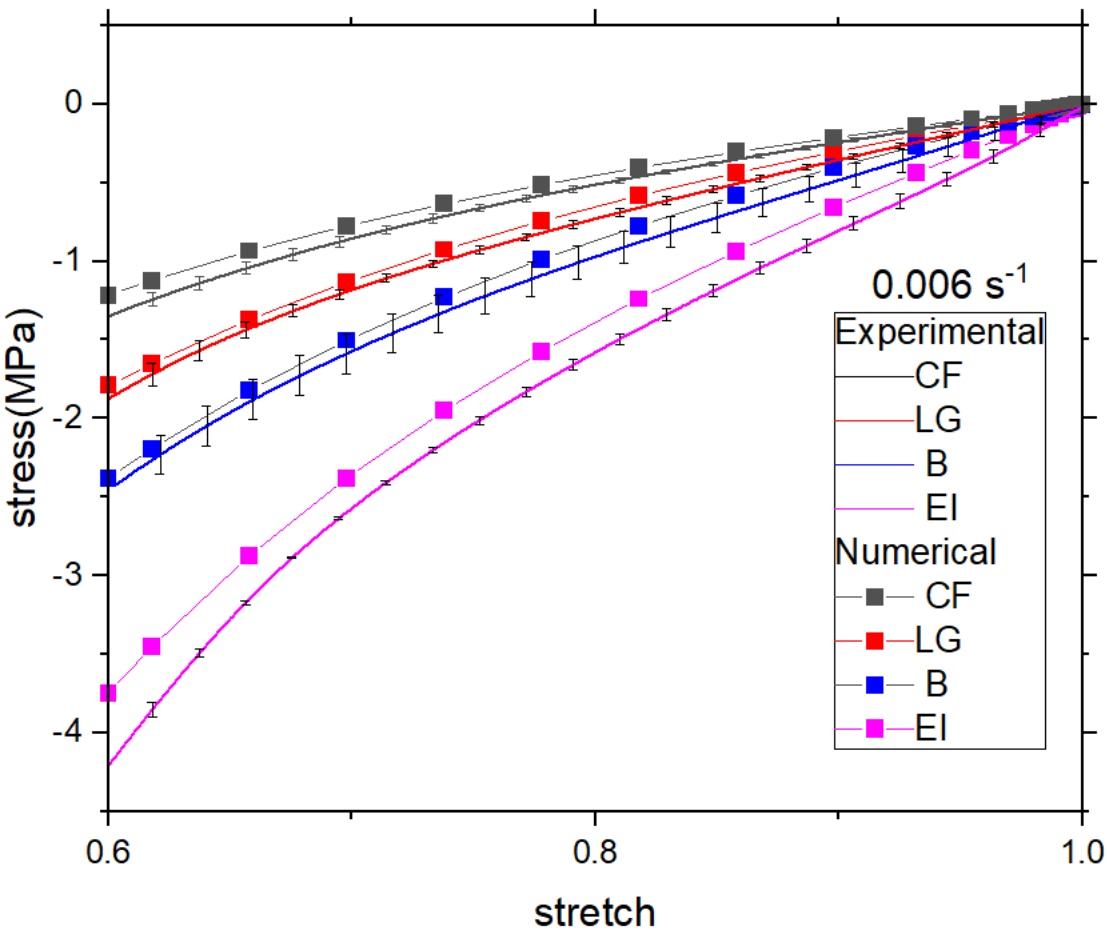

Fig. 6.6-3 Comparison between numerical and experimental compression curves for new fitting coefficients of table 6.1

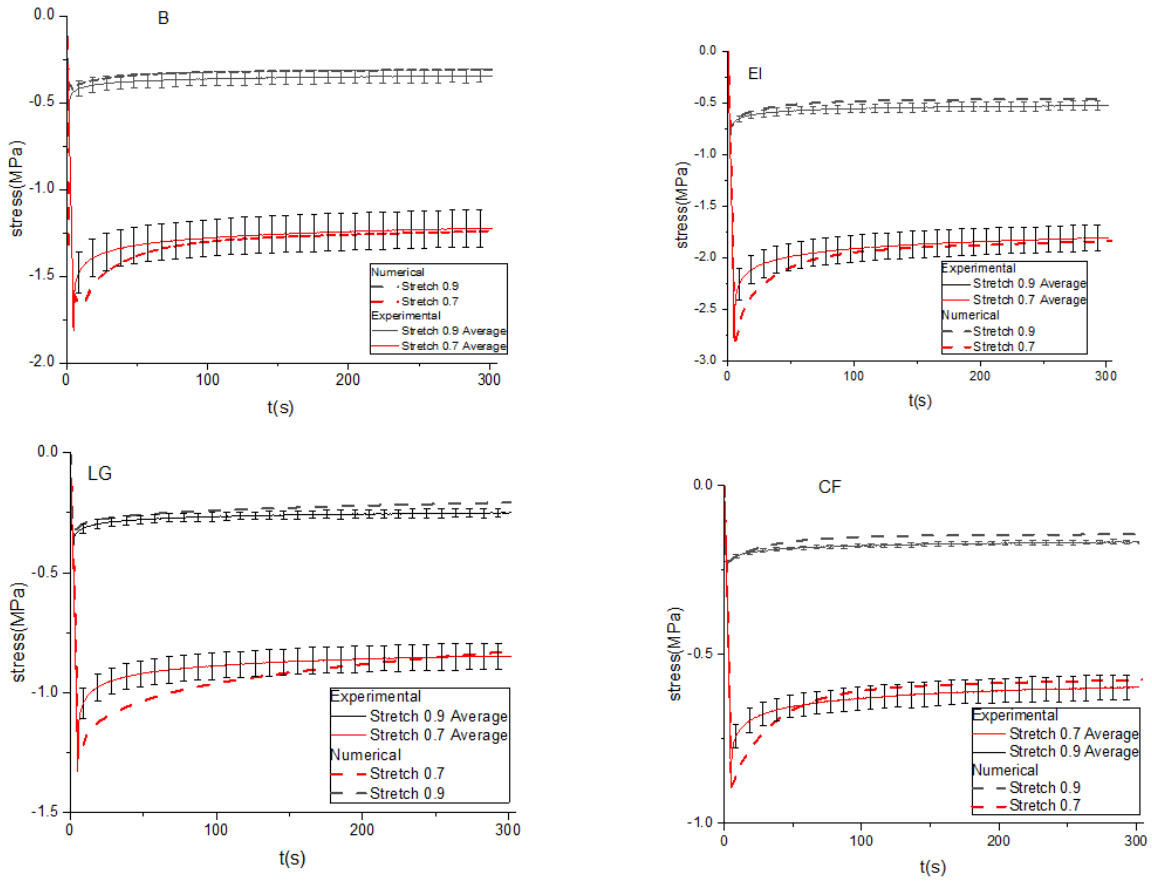

Fig. 6.6-4 Comparison between numerical and experimental stress-relaxation curves for new fitting coefficients of table 6.1

To extrapolate the frictionless behavior of the materials it was assumed that the mean ratio between the frictionless virtual curve and the experimental curve acting is the one found with the numerical model, considering as value of friction for the experimental curve the one measured with the sled for the corresponding PTFE-soap-PTFE configuration (about 0.1 for all velocities). From this value of friction, we extrapolated the mean ratio between the frictionless curve and the friction curve (0.1), as described in 6.3.6. This value is equal to 0.82 and it was then multiplied by the stress values of the soap experimental curves, obtaining in this way curves which should describe the frictionless behavior of the material. These curves were finally used for a new fitting. The final results are shown in table 6.2.

As expected the identified value of the hyperelastic coefficient C_{10} further decreases and, in all cases, is equal to about the 82% of the one obtained with the soap curves

fitting (in accordance with the proposed, "frictionless" rescaling factor). C_{01} is always equal to zero.

This time the viscoelastic function resulted the same obtained with the fitting of the soap curves. Only LG and CF showed a slight variation (figure 6.6.5).

To validate the results obtained, we run simulations of the experimental tests setting the friction at 0.1, value assigned to the experimental curves. The results were then compared with the experimental soap curves. The agreement is good as shown in figure 6.6.6 for the case of material B.

Similarly we tried to run simulations at the friction level measured for PTFE and steel interfaces and then compare them with the corresponding experimental curves. In addition we plotted the same simulations results found with the previous coefficients obtained in [19]. Of course the latter better describe the PTFE curve since it represents the data on which coefficients were fitted. However if we consider the steel curve, we see that having taken into account the effect of friction in the extrapolation of the material coefficients have improved the model accuracy, thanks to the improved description of friction within the model (figure 6.6.7).

Yet, even with this improvement the numerical model still predicts stress levels significantly higher than the experimental values (figure 6.6.7). The cause is probably related to the issues of the model that have been already discussed in 6.3.6 in particular: the edge effects in the sample and the excessive distortion in the elements. These aspects surely needs further investigation to understand why this discordance is recorded. Another aspect that should be taken into account is the dependence of friction on the contact pressure. The experimental values of COF in fact were measured in conditions of contact pressure much lower than the ones acting during the compression tests. The friction coefficients values measured on the sled therefore could be not representative of the actual contact. Due to these reasons the obtained results not completely reliable and surely need further study.

Material	C_{10} (MPa)	C_{01}(MPa)	g_1	g_2	g_3	g_4
B	0.66	0	0.19	0.059	0.14	0.060
EI	1.1	0	0.13	0.084	0.21	0.073
CF	0.36	0	0.24	0	0.22	0.050
LG	0.48	0	0.14	0.082	0.10	0.23

Table 6.2 Fitting of parameters on experimental curves obtained with soap lubricated PTFE interfaces rescaled by a factor of 0.82 computed from FEA simulations for COF 0.1.

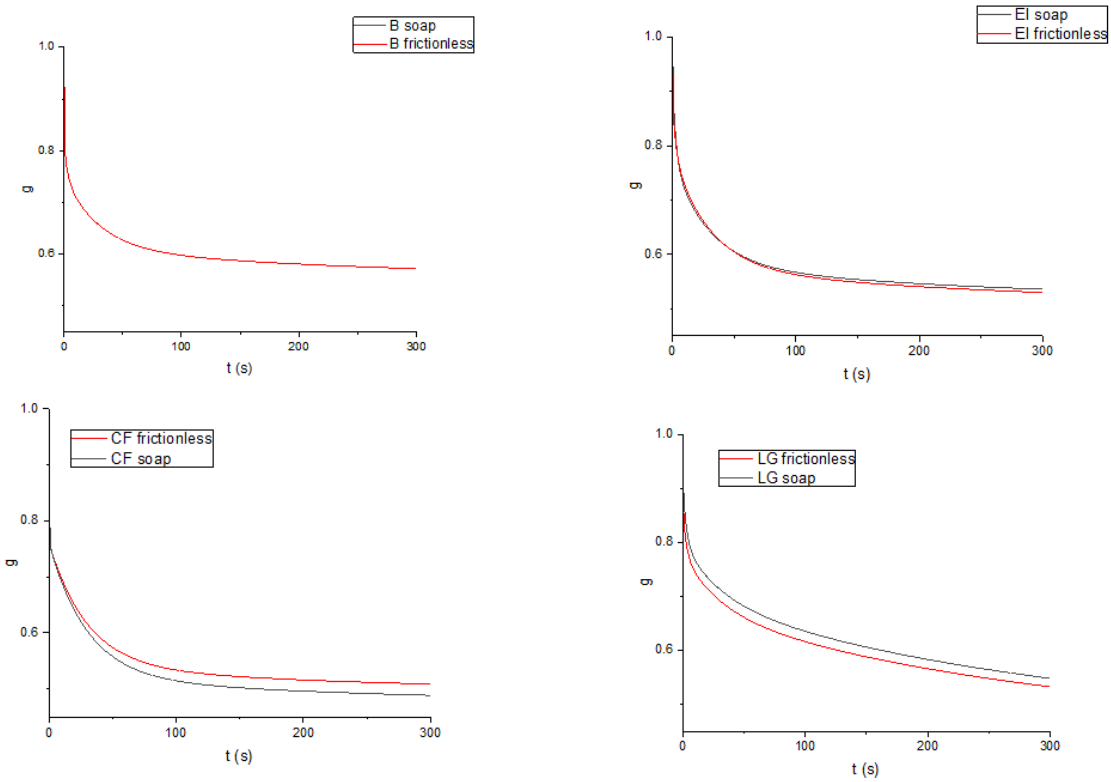

Fig. 6.6-5 Comparison between viscoelastic functions obtained with soap and the one obtained with curves rescaled by 0.82

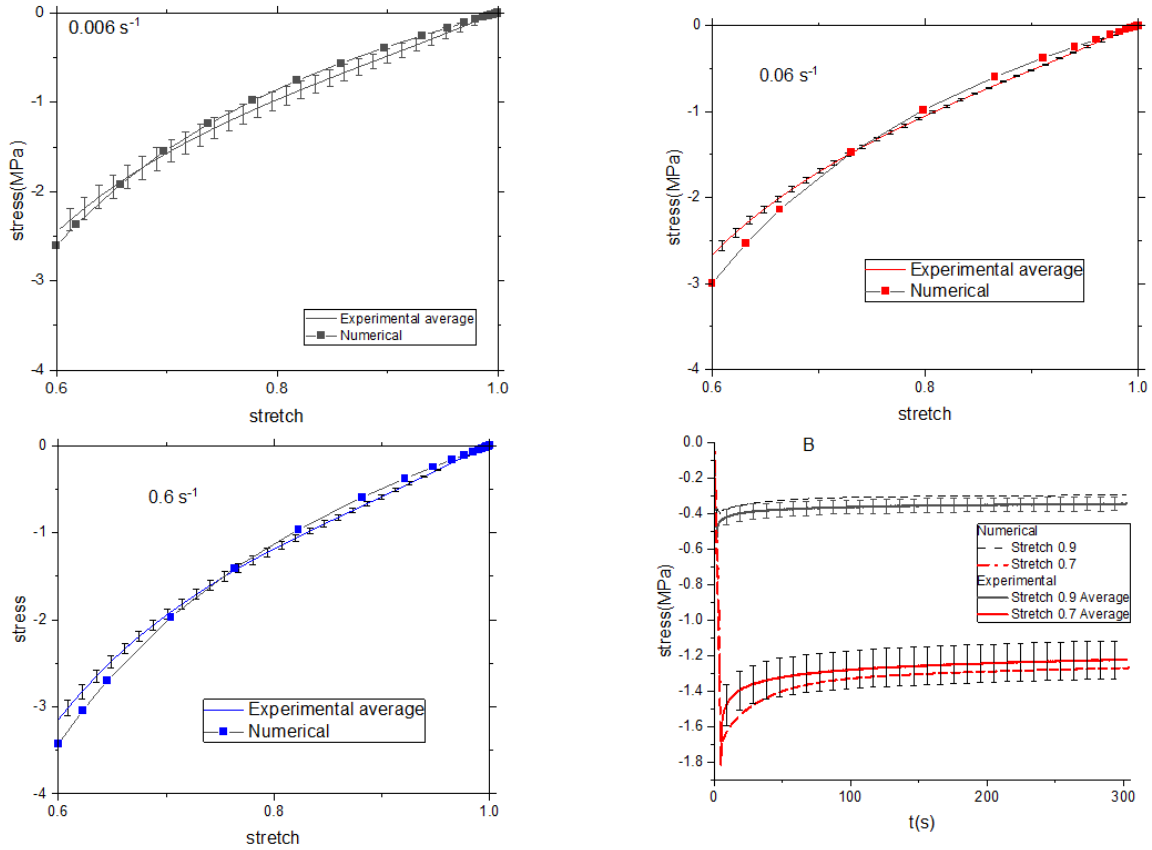

Fig. 6.6-6 Numerical simulations of compression and stress relaxation obtained with coefficients of table 6.2 for COF=0.1 and compared with experimental average soap curves (B)

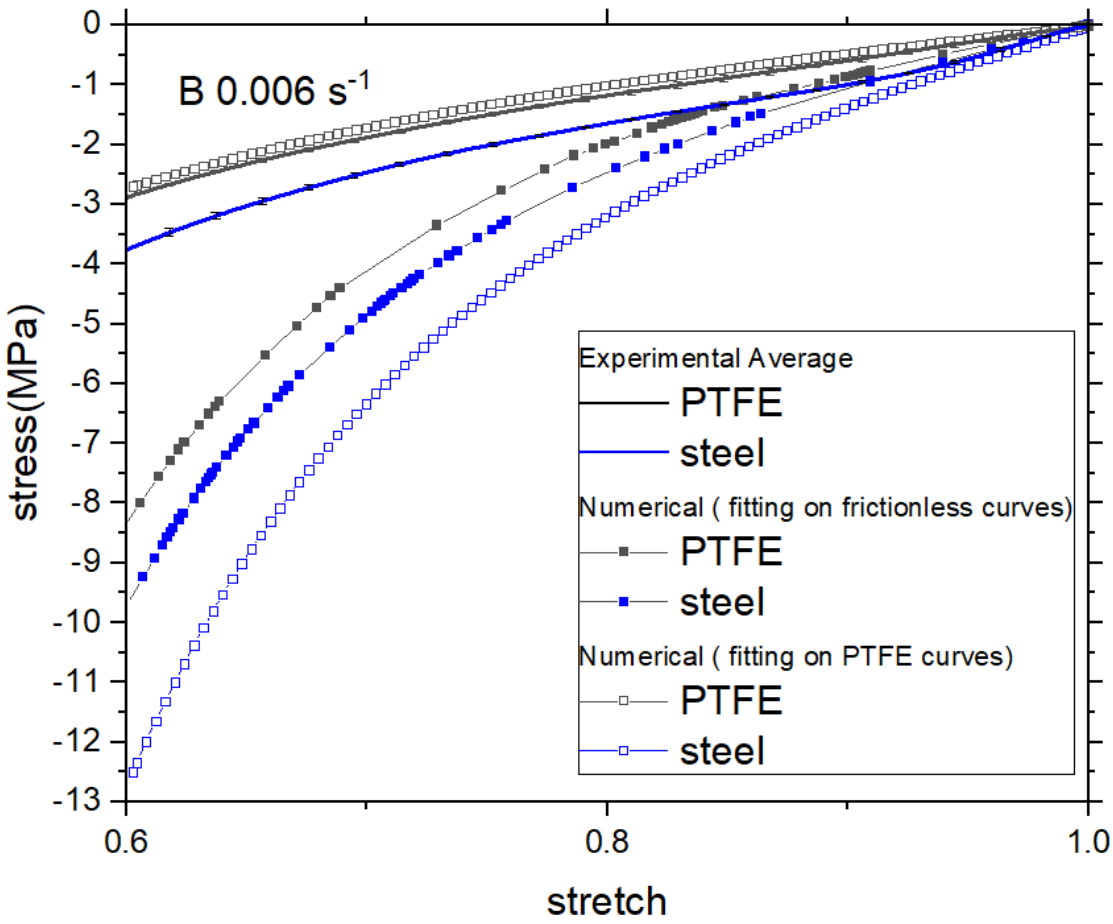

Fig. 6.6-7 Numerical simulations of compression obtained with coefficients of table 6.2 for COF assigned to PTFE and steel according to sled results and compared with experimental curves

7. CONCLUSIONS AND FUTURE DEVELOPMENT

In the present work we tried to account for the friction influence in the determination of the constitutive properties of four rubbery materials used for athletics tracks. Experimental friction coefficients were measured with a sled adopting different lubrication systems which used both solid (PTFE) and liquid (soap) lubricants. The same lubrication techniques have been used for the experimental compression and stress relaxation tests used to identify constitutive parameters. The latter have been input in a numerical model exploited to investigate the influence of friction on the tests results. Another numerical model representing the friction sled test was used to support study of the contact condition applied to the first model. Finally experimental results were fitted to find new coefficients for the materials in two ways: firstly the fitting has been done directly on the experimental curves (with an implicit assumption of negligible friction); in the second case virtual, frictionless curves were generated by rescaling the experimental ones, taking advantage of the numerical model.

For what concerns the first option we can say that the use of new lubrication techniques have for sure decreased the influence of friction and has allowed us to find more reliable materials coefficients that can be used for the characterization of the athletic tracks. Therefore the tested lubrication system with soap and PTFE proved to be a step in the right direction of minimizing the influence of friction during the compression tests. However these results are still influenced by friction as a negligible friction configuration is impossible to achieve from the experimental point of view.

For this reason the second approach described above was considered. These new results are still not fully satisfying; even if the new approach provides a marked improvement with respect to the previous one, some issues still need to be solved. In fact it was observed that the numerical model used to eliminate the friction influence was not able to completely predict experimental results previously obtained in [19]. In particular these results still showed a high dependence on friction at high level of COF where the numerical model showed the presence of a plateau. A possible cause is that the pressure under which friction coefficients were measured is much lower than the one acting during the real compression of the rubber samples, and this fact may affect the measured COF values. Due to the reasons listed above instead, the results obtained with the second fitting are not completely reliable and require

further investigation. However the realization of a model able to extrapolate the frictionless behavior of the materials seems feasible but, it still needs a considerable amount of future work.
For example, a way to improve the model could also be the collection of experimental compression curves for specimens of different aspect ratio and the comparison with corresponding numerical simulations [32]. In addition, further investigation on the dependence of friction on the applied contact pressure should be considered for the materials presented, in order to better understand which is the real value of friction acting during the compression test.
We can conclude saying that further studies about the realization of an accurate model able to extrapolate the frictionless behavior of the material could be really helpful to speed up the procedures for the characterization of rubbery materials at high level of compression strain, giving the possibility to obtain more reliable data to be used for the study about the optimization of the sports surfaces design.

BIBLIOGRAPHY

[1] World Athletics, Track and Field Facilities Manual. World Athletics, 2019.

[2] *"Tartan track"* accessed on 20/09/2021 https://en.wikipedia.org/wiki/Tartan_track

[3]J.Grandfield,*"First"*,15/09/2021,https://www.flickr.com/photos/32225523@N00/444310484/:

[4] *"Pavimentazioni, Sistemi erba sintetica,e attrezature sportive"* accessed on 15/09/2021, : https://www.mondoworldwide.com/emea/it/

[5]*"Athletics Track Tartan Flooring"*Accessed on 20/09/2021 http://www.innopurshield.com/athletics-track-tartan-flooring-applications/

[6]"*Paver tracks*" Accessed on 15/09/2021 https://www.continental-industry.com/en/solutions/undercarriage/rubber-tracks/products/product-range/paver-tracks

[7] M. Benanti, L. Andena, F. Briatico-Vangosa, and A. Pavan, *"Viscoelastic behavior of athletics track surfaces in relation to their force reduction,"* Polymer Testing, vol. 32, no. 1, pp. 52–59, 2013.

[8] UNI EN 14808 "*Superfici per aree sportive Determinazione dell'assorbimento degli urti"*

[9] D. J. Stefanyshyn and B. M. Nigg, *"Energy and Performance Aspects in Sport Surfaces,"* Sport Surfaces – Biomechanics, Injuries, Performance, Testing and Installation, vol. 1, pp. 31–46, 2003.

[10] Conica Sport floorings, *"Sport floors-Different Types of elasticity"*, accessed on 15/10/2021 https://conica.co.uk/wp-content/uploads/1_2b-Flooring-types-elasticity-en.pdf

[11] BS EN 14809:2005 "*Surfaces for sports areas — Determination of vertical deformation"*

[12]] L. Andena, S. Aleo, F. Caimmi, S. Mariani, F. Briatico-Vangosa, and A. Pavan,

"A 3D Numerical Model for the Optimization of Running Tracks Performance," Procedia Engineering, vol. 147, pp. 854–859, 2016.

[13] Adam I. Daoud, Gary J. Geissler, Frank Wang, Jason Saretsky, Yahya A. Daoud, and Daniel E. Lieberman; *"Foot Strike and Injury Rates in Endurance Runners: A Retrospective Study*", Official Journal of the American College of Sports Medicine, pp 1326

[14] A. A. Zadpoor and A. A. Nikooyan, "*The relationship between lower-extremity Stress fractures and the ground reaction force: A systematic review",* Clinical Biomechanics, vol. 26, no. 1, pp. 23–28, 2011.

[15] Luca Andena, Francesco Briatico-Vangosa, Antonio Ciancio, Stefano Mariani, Andrea Pavan, *"On the relationship between force reduction, loading rate and energy absorption in athletics tracks"*, J Sports Engineering and Technology 2018, Vol. 232(2) 71–78

[16] L. Andena, F. Briatico-Vangosa, E. Cazzoni, A. Ciancio, S. Mariani, and A. Pavan,*"Modeling of shock absorption in athletics track surfaces,"* Sports engineering, vol. 18, no. 1, pp. 1–10, 2015.

[17] L. Andena, F. Briatico-Vangosa, A. Ciancio, and A. Pavan, *"A finite element model for the prediction of Force Reduction of athletics tracks"*, Procedia Engineering, vol. 72, pp. 847–852, 2014.

[18] L. Andena, S. Aleo, F. Caimmi, F. Briatico-Vangosa, S. Mariani, S. Tagliabue, and A. Pavan, *"Modelling the cushioning properties of athletic tracks"*, Sports Engineering, vol. 21, no. 4, pp. 453–463, 2018.

[19] F. Cotta Ramusino *"A visco-hyperelastic model for elastomeric materials"*, Master Thesis in Materials engineering and nanotechnology at Politecnico di Milano, 2020

[20] S. M. Goh, M. N. Charalambides, and J. G. Williams, *"Large strain time dependentbehavior of cheese,"* Journal of Rheology, vol. 47, no. 3, pp. 701–716, 2003.

[21] I. M. Ward and J. Sweeney,*" Mechanical Properties of Solid Polymers"*, 3rd ed. Wiley, 2013.

[22] J. Bergstorm, *"Mechanics of solid polymers"*, Elsevier, 2015

[23] Husnu Dal, Kemal Acıkgoz, and Yashar Badienia:"*On the Performance of Isotropic Hyperelastic Constitutive Models for Rubber-Like Materials: A State of the Art Review*", Applied Mechanics Reviews, MARCH 2021, Vol. 73

[24]*" Abaqus user guide"* accessed on 20/09/2021
http://130.149.89.49:2080/v6.14/books/usb/default.htm

[25] R.W.Ogden*" Large deformation isotropic elasticity — on the correlation of theory and experiment for incompressible rubberlike solids"*, 1972

[26] A. Ciancio "*SIMULATION OF THE 'FORCE REDUCTION' TEST"* Master Thesis in Materials engineering and nanotechnology at Politecnico di Milano, 2013

[27] *"Introduction To The Finite Element Method (FEM)"*; P. Boeraeve; Institut Gramme, Liege;January 2010

[28] C. A. Felippa, *"Introduction to Finite Element Methods"*, 2004.

[29] A. N. Gent, F. M. Discenzo, J. B. Suh:" *Compression of Rubber Disks Between Frictional Surfaces"*

[30] H.T. Banks, G.A. Pinter, O.H. Yeoh: *"Analysis of bonded elastic blocks"*

[31] J.M. Horton, G.E. Tupholme, M.J.C. Gover: *"Axial loading of bonded rubber blocks"* Journal of Applied Mechanics NOVEMBER 2002 Vol. 69/ 843

[32]J.B. *Suh "STRESS ANALYSIS OF RUBBER BLOCKS UNDER VERTICAL LOADING AND SHEAR LOADING"* A Dissertation Presented to the Graduate Faculty of the University of Akron, 2007

[33]BS ISO 7743: 2017 *"Rubber, vulcanized or thermoplastic — Determination of compression stress-strain properties"* BS Standard Publication

[34] ASTM D1894 *"Standard test method for Static and Kinetic Coefficients of Friction of Plastic Film and Sheeting",* ASTM international

LIST OF FIGURES

LIST OF TABLES

Acknowledgements

I want to thank my supervisor Professor Luca Andena and my co-supervisor Dr. Stefano Tagliabue who helped me carrying out this project with their experience.

I would like to thank my family: my mother Donatella, my father Vincenzo, my sisters Maria Sole and Maristella and my nephew Riccardo and all my friends.

I would like to express my gratefulness to my university friends with which I've had a great time during my stay in the city of Milan.

Special thanks go to my girlfriend Lara who stood by me during my master degree.